Rockefeller University
Digital Commons @ RU

Student Theses and Dissertations

2021

Deciphering Cancer Metabolic Dependencies in the Tumor Microenvironment

Xiphias Ge Zhu

Follow this and additional works at: https://digitalcommons.rockefeller.edu/student_theses_and_dissertations

 Part of the Life Sciences Commons

DECIPHERING CANCER METABOLIC DEPENDENCIES IN THE TUMOR MICROENVIRONMENT

A Thesis Presented to the Faculty of
The Rockefeller University
in Partial Fulfillment of the Requirements for
the degree of Doctor of Philosophy

by
Xiphias Ge Zhu
June 2021

© Copyright by Xiphias Ge Zhu 2021

DECIPHERING CANCER METABOLIC DEPENDENCIES IN THE TUMOR MICROENVIRONMENT

Xiphias Ge Zhu, Ph.D.

The Rockefeller University 2021

Cancer cells face substantial pressure within the tumor microenvironment. Physical constraints and nutrient limitations in the tumor prevent excessive cell proliferation, while other cell types such as stromal and immune cells can compete with or kill cancer cells. To overcome these restrictions, cancer cells often possess oncogenic mutations or amplifications to divide rapidly but can also rewire their metabolism in adaptation to the environmental challenge. The metabolism of cancer cells exhibit high plasticity as many metabolic pathways and enzymes are redundant. This allows for cancer cells to adapt to the changing nutritional and intercellular context of the tumor. Though metabolic rewiring helps cancer cells survive and grow, the resultant reliance on specific metabolites or pathways present opportunities for therapeutic intervention. Recent advances in cancer metabolism have focused on characterizing these metabolic dependencies in different tumor contexts. This work employs unbiased CRISPR-guided genetic screens and large-scale metabolomics analyses to identify the metabolic dependencies of cancer cells under lipid saturation stress and characterize the *in vivo* specific metabolic liabilities of pancreatic tumors.

Cells require a constant supply of fatty acids to survive and proliferate but excess levels of fatty acids, specifically saturated lipids, are toxic to cells. However, the molecular mechanism of this toxicity is not well understood though this phenomenon is implicated in hypoxic tumors as cells require oxygen to desaturate fatty acids. Fatty acids incorporate into membrane and storage glycerolipids through a series of endoplasmic reticulum (ER) enzymes, but how these enzymes are regulated and how they contribute to lipid toxicity are also not well understood. With a combination of CRISPR-based genetic screens and unbiased lipidomics, we identified calcineurin B homologous protein 1 (CHP1) as a major regulator of ER glycerolipid synthesis and saturated lipid toxicity. Mechanistically, CHP1 binds and activates GPAT4, which catalyzes the initial rate-limiting step in glycerolipid synthesis. GPAT4 activity requires CHP1 to be N-myristoylated, forming a key molecular interface between the two proteins. Interestingly, upon CHP1 loss, the peroxisomal enzyme, GNPAT, partially compensates for the loss of ER lipid synthesis, enabling cell proliferation. Loss of CHP1 severely reduces fatty acid incorporation and storage in mammalian cells and invertebrates. Depletion of Chp1 and Gpat4 in the mouse liver reduces steatosis and inflammation during fatty liver disease. Our work identified a conserved regulator of glycerolipid metabolism and revealed metabolic regulators of cancer cells under saturated lipid toxicity.

To probe for similar lipid saturation stress and characterize the major metabolic dependencies of tumor growth in its endogenous microenvironment, we optimized our CRISPR screening approach on pancreatic ductal adenocarcinoma (PDAC). PDAC cells require substantial metabolic rewiring to overcome nutrient limitations and immune surveillance. However, the metabolic pathways necessary for pancreatic tumor growth *in vivo* are poorly understood. To address this, we performed metabolism-focused CRISPR screens in PDAC cells grown in culture or engrafted in immunocompetent mice. While most metabolic gene essentialities are unexpectedly similar under

these conditions, a small fraction of metabolic genes are differentially required for tumor progression. Among these, loss of heme synthesis reduces tumor growth due to a limiting role of heme *in vivo*, an effect independent of tissue origin or immune system. Our screens also identify autophagy as a metabolic requirement for pancreatic tumor immune evasion. Mechanistically, autophagy protects cancer cells from CD8+ T cell killing through TNFα-induced cell death *in vitro*. Altogether, the *in vivo* screens provide metabolic dependencies arising from microenvironmental limitations and the immune system, nominating potential anti-cancer targets.

Overall, this work provides a framework to identify the molecular mechanisms of specific metabolic liabilities and unbiasedly decipher the metabolic dependencies of cancer cells in the tumor microenvironment.

For science

ACKNOWLEDGMENTS

This work would not have been possible without the help and support from countless people. I would first like to thank Kivanç who has been a very supportive and engaging mentor. Kivanç took me on as his first student from the Rockefeller graduate program and was intricately involved in my training during the early days of the lab. I have been fortunate to be part of the pioneering batch of lab members who built this lab up from scratch and have learnt plenty along the way. Kivanç has been guiding us at every step: from experimenting techniques, presenting data, to writing and networking. He is always curious to make new discoveries and this enthusiasm has rubbed off on all of us. I am truly grateful for his mentorship and for providing us with a conducive environment to conduct insightful research. My experience in the lab has been extremely rewarding and this is what drives me to push forward every day.

I would next like to thank all members of the Birsoy Lab who have helped me one way or another. Lou Baudrier had been our essential lab manager who was foundational to the success of this lab and all my projects. Thank you for making my time in the lab so much easier and more enjoyable. Javi Garcia-Bermudez has been a wonderful buddy and someone I trust for questions scientific or non-scientific. Shirony Puthenveedu has been a tremendous help for my lipid project and I am really grateful to have worked with you. Ben Prizer has provided so much support with mouse injections, colony maintenance and all sorts of other experiments. Rebecca Timson and Yuyang Liu helped with many experiments in the mouse tumor project. It was also a great opportunity to work alongside Ying Wang and Fred Yen for the final months of my time in the lab to figure out SLC25A39. Konnor helped with many analyses of my screens and I am glad to have had all the interesting conversations with you. Erol has been my baymate for the longest time in the lab and it was great to work beside you. Eiko Nishiuchi has been amazing with administrative support and making sure all our scheduling is in order. Jak Fak was quick to jump into the role as our new lab manager and really helped us get through all the shortages during Covid times. Robbie Williams, Roy Guarecuco and Ross Weber have all helped in many ways and I will always remember our days as the first generation. Thank you to the newer members Mariluz Soula, Gokhan Unlu, Tim Kenny, Hsi-wen Yeh and Max Stahl for all your help and making the lab exciting and enjoyable. I am grateful to have worked with all of you in such a productive lab environment.

Beyond the Birsoy Lab, I must extend my thanks to all our collaborators and colleagues from other labs or institutions who have provided their assistance. The Wei Min Lab from Columbia University was of great importance in helping us visualize fatty acid uptake into cells. The Howard Hang Lab helped us by labeling the myristoyl tail of CHP1. Yetis Gultekin and Diana Klompstra, respectively, made our analyses in *C. elegans* and *D. melanogaster* possible. The Gabriel Victora Lab assisted greatly with our immune profiling of tumors. Ben Ostendorf, Bernardo Tavora and Nori Yamaguchi from the Tavazoie Lab all helped out with critical experiments. Hani Goodarzi from UCSF also helped us with a lot of big data analyses. I would also like to thank all the Resource Centers in Rockefeller for being very supportive and responsive. Henrik Molina, Justine Fidelin, Søren Heissel and Hanan Alwaseem from the Proteomics Resource Center have run too many mass spec samples for me to keep track. Thanks to Connie Zhao, Christine Lai and Bin Zhang from the Genomics Resource Center for running our sequencing experiments and accommodating our custom libraries. Alison North and Kaye Thomas from the Bio-imaging Resource Center provided support for our imaging. Svetlana Mazel and all members of the Flow Cytometry Resource Center have also been crucial help for our flow cytometry and sorting experiments. Special thanks also go out to everyone in the Dean's Office, namely Sid Strickland, Emily Harms,

Andrea Morris, Kristen Cullen, Marta Delgado, Cris Rosario and Stephanie Fernandez who have all personally been of help to me throughout my PhD training. We can have a world-class graduate program all thanks to them.

Next, I have to thank my committee members: Drs. Sandy Simon, Sohail Tavazoie and David Allis. Your support and suggestions have been extremely valuable over the years. I would also like to thank Dr. Celeste Simon for being my external examiner. I truly value your input and hope to get a chance to collaborate with you in the future. Special thanks also go to Dr. Paul Cohen whom I first rotated with upon joining the program. He has continued to provide good advice and support for me since then.

Finally, I thank all my family and friends who have been with me along this journey. My parents have always driven me to aim higher and I could not have arrived here without their love and support. My grandparents and extended family are always thinking of me and I wish I could have visited them more often. My friends in NUS have been supportive from the very beginning as I started research and I am glad to have found this passion with them. I am grateful to my undergraduate mentor Professor Ding Jeak Ling for guiding me on my first individual research project. Thank you to my scientific godfather, Marius Sudol. I will always remember your lecture at the Tumor Biology class where you introduced Rockefeller University and made me apply to the program in the first place. Last and definitely not least, to Jingyi, my partner in life and in science, I have been most fortunate to have met you just as I started in Rockefeller. I could not imagine how I would have made it here without your support in every single aspect of my life. In and out of the lab, you always light up my days, especially when the going gets tough. You make me a better scientist and a better person. I will always be grateful.

TABLE OF CONTENTS

LIST OF FIGURES

LIST OF TABLES

LIST OF ABBREVIATIONS

AcCa - acylcarnitine
ACSL - acyl-coenzyme A synthetase long-chain family member
ATP - adenosine triphosphate
BSA - bovine serum albumin
CD - cluster of differentiation
Cer - ceramides
CerG1 - neutral glycosphingolipid
CHP - calcineurin B homologous protein
CL - cardiolipin
CoA - coenzyme A
CRISPR - clustered regularly interspaced short palindromic repeats
DHAP - dihydroxyacetone phosphate
DG - diacylglycerol
ETC - electron transport chain
ER - endoplasmic reticulum
FA - fatty acid
$FADH_2$ - flavin adenine dinucleotide reduced
GFP - green fluorescent protein
GPAT - glycerol-3-phosphate acyltransferase
HA - hemagglutinin
HMBS - hydroxymethylbilane synthase
HIF - hypoxia-inducible factors
IFNγ - interferon gamma
IP - immunoprecipitation
KP - $Kras^{G12D}/Trp53^{R172H}$ mutant
LbNOX - NADH oxidase from Lactobacillus brevis
LC-MS - liquid chromatography–mass spectrometry
LPC - lysophosphatidylcholine
LPE - lysophosphatidylethanolamine
MG - monoacylglycerol
MHC - major histocompatibility complex
NADH - nicotinamide adenine dinucleotide reduced
NADPH - nicotinamide adenine dinucleotide phosphate reduced
NAFLD - non-alcoholic fatty liver disease
NASH - nonalcoholic steatohepatitis
NES - nuclear export signal
NK - natural killer
NSG - NOD scid gamma
OXPHOS - oxidative phosphorylation
OVA - ovalbumin
PA - phosphatidic acid
PC - phosphatidylcholine
PDAC - Pancreatic ductal adenocarcinoma
PDX - patient-derived xenografts

PE - phosphatidylethanolamine
PG - phosphatidylglycerol
phSM - sphingomyelin (phytosphingosine)
PI - phosphatidylinositol
PIP - phosphatidylinositol phosphate
PS - phosphatidylserine
PSM - peptide spectrum mass
ROS - reactive oxygen species
RNAi - RNA interference
SCD - stearoyl-CoA desaturase
sgRNA - single guide RNA
SM - sphingomyelin
SRS - stimulated Raman scattering
TCA - tricarboxylic acid
TG - triacylglycerol
TNFα - tumor necrosis factor alpha

CHAPTER 1. Introduction.

1.1 Metabolic reprogramming of cancer cells in the tumor microenvironment

The tumor microenvironment that cancer cells thrive in is unique for each cancer type and demonstrates high heterogeneity, with different stresses that either promote or inhibit tumor growth (Balkwill et al., 2012). As the tumor progresses, cancer cells usually undergo cell autonomous and non-autonomous alterations that help them proliferate. These alterations can result from oncogenic mutations or metabolic reprogramming that help cancer cells use nutrients more effectively. Metabolic reprogramming has thus been identified as a hallmark of cancer (Hanahan and Weinberg, 2011) and is a well-recognized phenomenon in most cancer types. Though these cancer cells can proliferate well in a harsh environment, their dependence on reprogrammed metabolism exposes them to targeted therapeutic interventions. Current trends in cancer metabolism studies focus on characterizing such metabolic dependencies and exploiting them for the development of novel targeted therapeutics. Though the field has greatly advanced in the past decade, we still lack a complete understanding of the metabolic dependencies of cancer cells in the context of each environmental stress in the tumor microenvironment. This work attempts to use recently developed techniques such as CRISPR-guided genetic screens and metabolomics analysis through LC-MS to systematically identify the metabolic dependencies of cancer cells in the tumor microenvironment as well as under specific metabolic challenges.

1.2 Metabolic dependencies of cancer cells in response to challenges in the tumor microenvironment

Unlike unicellular organisms whose metabolic regulation is relatively well understood, mammalian cells have complex metabolic networks that differ according to cell type and display high plasticity due to the interconnectivity of metabolic networks (Metallo and Vander Heiden, 2013). Redundant pathways can often be employed to synthesize limiting metabolites and certain metabolic reactions can also be co-opted for alternative functions to promote cell growth. Hence, the metabolic adaptation of cancer cells to each environmental challenge is specific and presents unique dependencies which can be targeted. Some of the most influential challenges which contribute to cancer metabolic reprogramming include nutrient limitations, oxygen deprivation and the interaction with other cell types in the tumor microenvironment. We present here some well characterized metabolic dependencies of cancer cells and provide our aims to present a complete unbiased understanding of cancer metabolic dependencies in the tumor microenvironment.

1.2.1 Nutrient limitations of cancer cells

As cancer cells are actively proliferating, they require a constant supply of nutrients for energy production and the synthesis of biomolecules. Two key nutrients that support most metabolic processes in the cell are glucose and glutamine. Both glucose and glutamine are essential nutrients that are required for the generation of adenosine triphosphate (ATP) either directly via glycolysis or indirectly through controlled oxidation of glucose carbons in the form of reduced nicotinamide adenine dinucleotide (NADH) or flavin adenine dinucleotide ($FADH_2$), which facilitate electron transfer to the electron transport chain (ETC). They also support the production of reduced

nicotinamide adenine dinucleotide phosphate (NADPH), a reducing cofactor that drives many biosynthetic reactions and maintains cellular redox capacity. Additionally, the downstream metabolites of both glucose and glutamine serve as anabolic precursors for the synthesis of a wide range of biomolecules such as nucleic acids, proteins, and lipids to drive cancer cell growth.

Given the necessity of these essential nutrients for cell growth and proliferation, cancer cell autonomous alterations in the form of oncogenic mutations often serve to increase their uptake and processing. The concept that cancer cells possess an altered metabolic state with increased nutrient uptake was first developed during the 1920s by German biochemist Otto Warburg, hence termed the Warburg effect (Liberti and Locasale, 2016). Warburg discovered that tumors, unlike normal cells that depend on oxidative phosphorylation (OXPHOS) for energy in aerobic conditions, exhibit a significant increase in glucose consumption and glycolysis. Positron emission tomography (PET)-based imaging technology has since leveraged the Warburg effect principles by locating regions with enhanced ^{18}F-flurodeoxyglucose uptake in order to diagnose tumors, stage, and determine treatment responsiveness (Kelloff et al., 2005). Increased glucose uptake through the glucose transporter (GLUT) family is found to be a common phenomenon in cancer cells, leading to a high rate of glycolysis and cell proliferation (Barron et al., 2016). Kirsten rat sarcoma viral oncogene homolog (KRAS) mutations in many cancer types can lead to increased glucose uptake, whereby cancer cells exhibit increased glycolysis and channeling of glucose-derived metabolites into various anabolic pathways (Kerr et al., 2016; Ying et al., 2012).

Despite the propensity of cancer cells to increase nutrient uptake, the effectiveness of solely relying on this strategy in the tumor microenvironment is limited. An ever-increasing number of proliferating cells results in a corresponding decrease in nutrient availability. Such nutrient deprivation promotes cancer cells to develop metabolic rewiring to survive and proliferate. Under glucose depletion, many cancer cells switch to glutamine as the main carbon source. The TCA cycle can be rewired to be solely fueled by glutamine, generating citrate comprised of only glutamine-derived carbons (Dang, 2012). Activation of cAMP-dependent protein kinase A (PKA) enhances the survival of cancer cells in low glucose environments by enhancing glutamine metabolism and increasing autophagy (Palorini et al., 2016). Myc expression in cancer cells can also drive glutamine uptake and its subsequent metabolism, promoting cell proliferation (Hensley et al., 2013).

In extreme nutrient depleted conditions, cancer cells can recycle key metabolites from within the cells or in the microenvironment. Many cancer cells can undergo autophagy to replenish amino acids and metabolic intermediates (Galluzzi et al., 2014). Macropinocytosis, on the other hand, allows cells to take up extracellular proteins to be degraded via the endocytic pathway. Degradation of extracellular proteins contributes to an in increased carbon and nitrogen supply, and subsequently enhancing cell survival (Commisso et al., 2013). Processes like autophagy and macropinocytosis can thereby serve as a stopgap for cancer cells until they become replenished with nutrients or rewire their metabolism to circumvent nutrient limitations.

1.2.2 Oxygen deprivation in the tumor microenvironment

Apart from the limitation of nutrients in the environment, physical challenges such as the lack of oxygen also play a key role in regulating cancer cell survival. Oxygen is critical for energy production in cells by being the final electron acceptor in the ETC. When oxygen is limited in hypoxic environments, mitochondrial ATP production is impaired and cellular processes will be

negatively affected (Wheaton and Chandel, 2011). Despite its putatively crucial role in producing ATP, the mitochondria have been shown to be essential under ETC inhibition for cell proliferation by enabling the synthesis of aspartate, which is necessary for nucleotide and protein synthesis (Birsoy et al., 2015). Hence, ETC impairment during hypoxia can inhibit cell proliferation by limiting anabolic substrates. Hypoxia is a common phenomenon challenging many cancer cells. As tumor size increases without an accompanied increase in vascularization, the tumor microenvironment becomes hypoxic. Given the essential role of oxygen in survival, cells have maintained a robust oxygen sensing and response mechanism in the form of hypoxia-inducible factor 1 (HIF-1). HIF-1 is a transcription factor that induces a large variety of genes to increase glycolysis, angiogenesis and improve cell survival upon reduction of oxygen levels (Harris, 2002). HIF-1 has also been shown to upregulate miR-210 which represses the assembly of iron-sulfur clusters which are critical components of the ETC (Chan et al., 2009). Hence, HIF-1 shifts cellular energy expenditure from oxidative phosphorylation to glycolysis to enhance survival in a hypoxic environment. In the presence of oxygen, HIF-1 is hydroxylated and degraded by the proteasome but becomes stabilized during hypoxia. Many cancer cells in hypoxic tumors are heavily dependent on HIF-1 and its function has been well characterized in cancer. Targeting HIF-1 for cancer therapy has been an ongoing process but it has seen limited success over the years due to difficulties in developing specific and efficient therapeutics (Semenza, 2003). New approaches are necessary to exploit cancer cells' dependency on oxygen in the tumor microenvironment.

Besides the ETC, many other metabolic reactions also require oxygen (**Figure 1.1**) and may be limiting to cancer cells in hypoxic conditions. Incidentally, recent advances have uncovered the oxygen-requiring lipid desaturation process as another metabolic liability of cancer cells under hypoxic stress (Ackerman et al., 2018; Ackerman and Simon, 2014). Lipids are an important component of the cell membrane and their availability is crucial for cancer cell proliferation. Due to the limited supply of lipids in the tumor microenvironment, cancer cells often exhibit increased *de novo* lipogenesis to meet their lipid needs (Peck and Schulze, 2016). While the synthesis of fatty acids (FAs) is crucial, newly synthesized FAs are saturated and have to be desaturated for several downstream processes. A balance of saturated and unsaturated FAs within the cell is crucial for membrane dynamics, signaling and prevention of lipotoxicity. The rate-limiting desaturation reaction involving the enzyme stearoyl-CoA desaturase 1 (SCD1) requires molecular oxygen and its function is inhibited during hypoxic stress, leading to an accumulation of saturated FAs (Ackerman et al., 2018). In order to overcome the accumulation of saturated lipids during hypoxia, certain cancer cells can scavenge lysophospholipids which contain unsaturated FA tails from the cell exterior. This process is shown to involve macropinocytosis driven by Ras activation (Kamphorst et al., 2013).

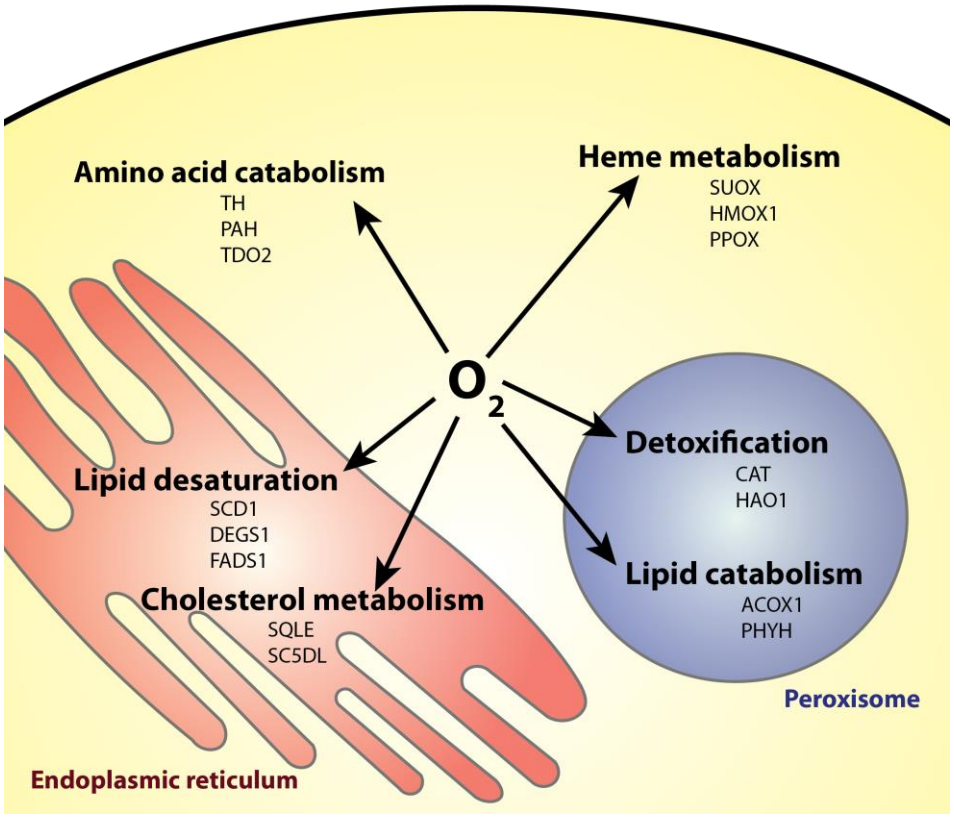

Figure 1.1. Metabolic processes and enzymes which require oxygen.
Examples of enzymes that require oxygen within different metabolic processes are provided. Apart from being the final electron acceptor in the ETC, oxygen is also required for a variety of other metabolic reactions. Hypoxia in the tumor microenvironment may inhibit these processes and lead to their specific metabolic liabilities in cancer cells.

1.2.3 Coordination and competition with other cell types in the tumor microenvironment

While much of the studies on cancer metabolism have focused on changes within cancer cells, the complex tumor microenvironment which consists of other cell types is relatively less appreciated when accounting for changes in cancer metabolism. The presence of other cell types within the tumor allows for metabolic crosstalk and competition that further influences cancer cell growth.

Stromal and fibroblast cells within the tumor are sometimes in symbiosis with cancer cells by supporting their growth with nutrient exchanges. Certain types of cancer cells have been shown to exploit metabolites secreted from surrounding stromal cell types for their own proliferation. Cancer-associated fibroblasts transfer nutrients to cancer cells through the secretion of lactate which can be used as a fuel (Becker et al., 2020; Hui et al., 2017). Pancreatic cancer cells have been shown to obtain alanine secreted by stromal-associated stellate cells to fuel their TCA cycle and lipid synthesis (Sousa et al., 2016). Melanoma cells in zebrafish can directly obtain fatty acids from nearby adipocytes (Zhang et al., 2018) while breast cancer cells can also depend on creatine derived from adipocytes for tumor progression (Maguire et al., 2021). Furthermore, breast

carcinomas maintain high iron concentration by using stromal inflammatory cells as a tissue iron reservoir and receive "iron-donations" from surrounding lymphocytes and macrophages (Marques et al., 2016).

On the other hand, immune cells within the tumor microenvironment are often suppressive of cancer cell growth. Even after discounting their immune surveillance and cytotoxic properties on cancer cells, immune cells are often competing for nutrients and growth signals. Lymphocytes compete with cancer cells for glucose in the tumor microenvironment, and a decrease in glucose availability in T cells can suppress their effector functions (Chang et al., 2015). Increase in lactate secreted by cancer cells also drive macrophages towards an M2 phenotype that is more immune suppressive and cancer promoting (Colegio et al., 2014). Breast cancer cells in obese individuals have also been reported to increase their lipid uptake to outcompete T cells for fatty acids which are necessary for T cell activity (Ringel et al., 2020).

1.3 Identifying metabolic dependencies of cancer cells in the tumor microenvironment with unbiased screens

Although individual metabolic dependencies, as we highlighted, have been well studied for many cancer types, we do not yet understand the molecular mechanisms of most metabolic dependencies and still lack a complete unbiased characterization of the relative dependencies on each metabolic pathway within most tumor types. We aim to approach this goal with two separate strategies: (1) elucidate the genetic regulators and the mechanism of a specific metabolic dependency and (2) provide an overview of the most crucial metabolic liabilities of a specific tumor type.

We were first interested in understanding how cancer cells respond to lipid saturation stress which may be a result of hypoxia. Primarily, the mechanism of lipotoxicity within the cell is not fully understood and the metabolic regulators of this process have not been completely identified. We thus designed a series of unbiased CRISPR-based genetic screens to characterize the metabolic liabilities of cancer cells under lipotoxicity and identify its genetic regulators. From these screens, we identified a poorly characterized protein, CHP1, and showed that it is essential for glycerolipid synthesis and is necessary for saturated lipid toxicity. We subsequently probed CHP1's physiological function and showed its role in regulating lipid accumulation in a fatty liver disease model.

Despite our success in elucidating the molecular regulators of lipid saturation stress in cancer cells, the actual tumor microenvironment is complex and cannot be easily replicated by *in vitro* culture conditions. Many metabolic adaptations and crosstalk of cancer cells with other cell types are also relatively uncharacterized and have to be studied in their endogenous environment. Hence, we modified our *in vitro* screening strategies to develop an *in vivo* screening protocol to unbiasedly identify the metabolic dependencies of pancreatic cancer cells in the harsh tumor microenvironment. Our series of *in vivo* screens revealed the major environment and immune-dependent metabolic liabilities of pancreatic tumor growth. Overall, our screening approaches provide a compendium of metabolic dependencies of cancer cells under various environmental challenges and present a path forward to fully characterize the metabolic liabilities of each cancer cell type in its specific microenvironment.

CHAPTER 2. CHP1 determines the response of cancer cells to lipotoxicity through glycerolipid synthesis.

2.1 Toxicity of saturated lipids

Lipids are essential building blocks of cellular structures and serve as the largest store of energy in most cell types. Most lipids consist of one or more fatty acids that may be conjugated to one or more chemical groups (**Figure 2.1**). Three main types of lipids are present in most cell types: structural phospholipids, storage triacylglycerols and sterols. The main bulk of the cell plasma membrane and organellar membranes is made up of phospholipids which consist of two hydrophobic fatty acids attached to a hydrophilic phosphoglycerol group. The amphiphilic nature of phospholipids allows them to serve as a barrier between aqueous environments. Phospholipids are further divided into subclasses such as phosphatidylcholine, phosphatidylethanolamine and other minor species which serve specific roles in different organelles. On the other hand, storage lipids reside in lipid droplets within cells and mainly consist of triacylglycerols which comprise of three fatty acid tails attached to a glycerol group. Both phospholipids and triacylglycerols are glycerolipids which make up the majority of the lipidome inside the cell. Sterols are complex ring-structured lipids that are metabolic precursors and can also be found in some cellular membranes. Besides the major glycerolipids and sterols, other classes of lipids such as cardiolipins, sphingolipids and free fatty acids serve other functions such as metabolic and signaling intermediates.

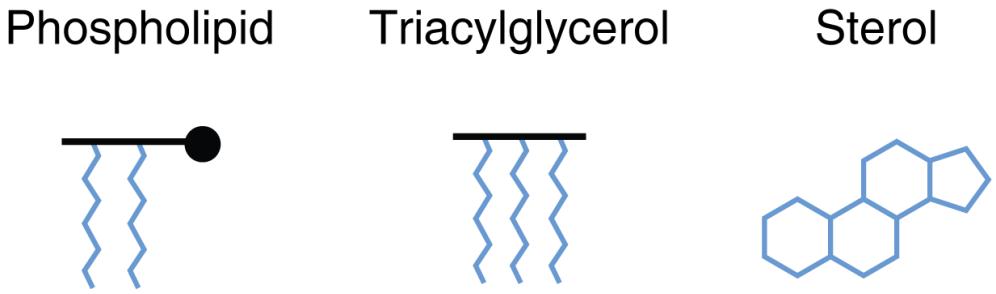

Figure 2.1. Major types of lipids.
Phospholipids consist of one or two fatty acid tails attached to a phosphoglycerol group. Triacylglycerols are made up of three fatty acid tails attached to a glycerol group. Phospholipids and triacylglycerols are both glycerolipids. Sterols are lipids with ring structures.

Though lipids are necessary for cell survival and proliferation, excess lipids are toxic to cells, especially in cell types that are not adapted to deal with lipid storage. This phenomenon is known as lipotoxicity and its effects have been well characterized in tissues such as the liver, muscles and heart. In mammals, the adipose tissue is highly specialized in storing energy as lipids in times when energy intake exceeds energy demand. White adipocytes in the adipose tissue have enlarged lipid droplets to store excess lipids. Cells in other tissues cannot adequately deal with excess lipids and show varying degrees of toxicity. The exact mechanism of cellular lipotoxicity has evaded scientists for decades but recent studies have allowed us to specifically identify the type of lipid involved and its mechanism of action.

Apart from the previously mentioned lipid classes, lipids can also be characterized by the saturation of their fatty acid tails. The degree of saturation in lipids is determined by the presence of C=C double bonds in their fatty acid tails. Saturated lipids have straight fatty acid tails with

fully saturated C-C bonds while unsaturated lipids have angled fatty acid tails due to the presence of C=C double bonds (**Figure 2.2**). It has been appreciated since the 1960s that saturated lipids are toxic to animals. Young mice weanlings that were fed a diet with high levels of saturated fatty acids such as palmitate and stearate exhibited poor health and higher mortality rates (Tove, 1964). This toxicity was reversed when unsaturated fatty acids such as oleate and linoleate were added to the diet. Fat content of the adipose tissue of the mice was minimally affected by changes in diet fatty acid content. These results suggest that toxicity of saturated fatty acids probably arise before they are assimilated as complex storage lipids in the adipose tissue and this effect is dependent on the relative abundance of saturated and unsaturated fatty acids.

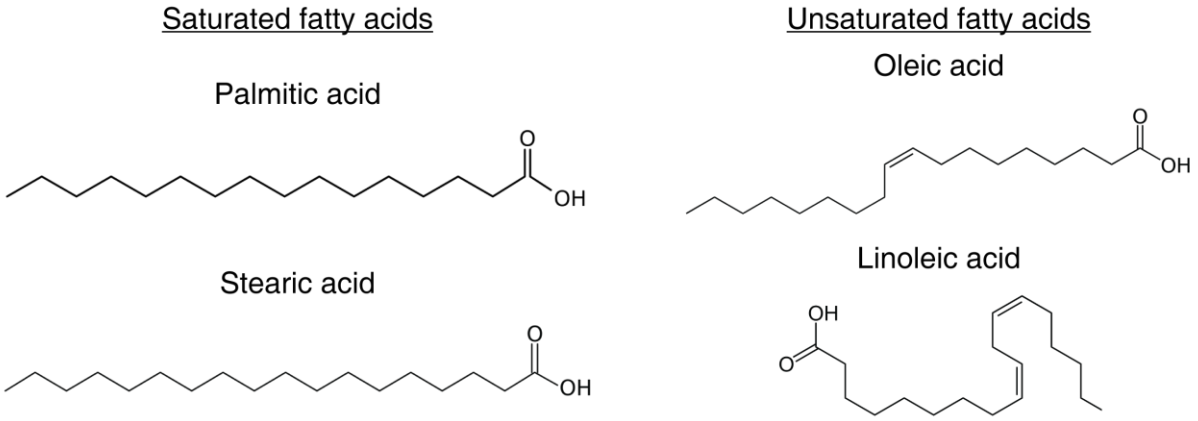

Figure 2.2. Saturation of fatty acids.
Saturation of fatty acids are determined by the presence of C=C double bonds in the fatty acyl chains. Saturated fatty acids such as palmitic acid and stearic acid do not have double bonds. Unsaturated fatty acids such as oleic acid and linoleic acid have one or more C=C double bonds which add kinks to the fatty acyl chain.

2.2 Excess saturated fatty acids lead to apoptosis in cancer cells

We were previously unclear of how exactly saturated fatty acids may cause toxicity. Human cells in culture arrest and die when treated with high levels of palmitate, the most abundant fatty acid in our body, but can be rescued with the addition of unsaturated fatty acids (Listenberger et al., 2003). The cause of this toxicity has been attributed to ROS stress, ER stress and ceramide toxicity but a conclusive finding was only made very recently. Using simulated Raman spectroscopy (SRS) microscopy, labeled palmitate molecules were found to accumulate in the ER membrane as they were synthesized into complex lipids. This results in an impairment of ER membrane fluidity as palmitate incorporates into ER glycerolipids and disrupts the membrane saturation balance to form a solid membrane sheet (Shen et al., 2017), ultimately leading to apoptosis (**Figure 2.3A**). Indeed, excess palmitate accumulates within sheet-like structures, representing solid phase membranes of the ER (**Figure 2.3B**). The toxicity due to saturated fatty acids is specific to the ER membrane as triacylglycerol synthesis, which diverts fatty acids away from phospholipids, is protective (Chitraju et al., 2017; Listenberger et al., 2003).

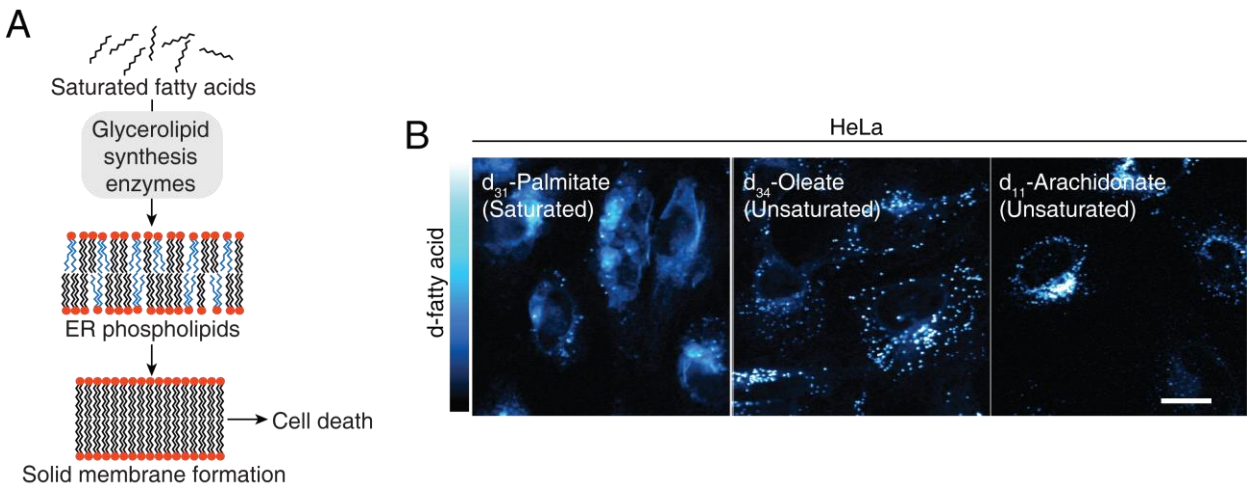

Figure 2.3. Saturated fatty acids cause cell death through solid membrane formation. (**A**) Saturated fatty acids incorporate into ER phospholipids through the glycerolipid synthesis pathway and ultimately result in cell death due to ER membrane solidification. (**B**) Stimulated Raman scattering imaging of the indicated deuterium-labeled fatty acid treated HeLa cells. Intensity indicates the relative concentrations of labeled fatty acid metabolites. Scale bar, 20 μm.

Lipotoxicity due to accumulation of saturated fatty acids is highly relevant in the tumor microenvironment. Since the balance of lipid saturation is critical for cell survival, cells can convert newly synthesized or exogenous saturated fatty acids into unsaturated fatty acids through a group of lipid desaturase enzymes. The principal desaturase enzyme, steroyl-coenzyme A desaturase (SCD), requires oxygen for its reaction. Most cancers reside in a hypoxic environment with limited oxygen supply which can inhibit the desaturation reactions catalyzed by SCD. Such a phenomenon has been shown in clear cell renal cell carcinoma where SCD inhibition due to hypoxia leads to the accumulation of saturated fatty acids and subsequently lipotoxicity (Ackerman et al., 2018).

For cancer cells to prevent lipotoxicity during hypoxia, cells need to regulate the level of fatty acid synthesis and uptake, as well as its incorporation into phospholipids and other glycerolipids. A better understanding of the regulators of glycerolipid synthesis will help us identify potential means to target cancer cells in a hypoxic tumor. However, apart from a few transcriptional and posttranscriptional mechanisms (Ericsson et al., 1997; Haas et al., 2012; Peterson et al., 2011; Shan et al., 2010), regulators of glycerolipid synthesis from fatty acids have not been thoroughly defined. To fully characterize the genetic regulators of glycerolipid synthesis, we reasoned that perturbing genes involved in the synthesis of ER glycerolipids should alter the cellular sensitivity to palmitate toxicity and that a genetic screening strategy may identify potential regulators of this pathway.

2.3 CRISPR-based genetic screen identifies metabolic regulators of lipotoxicity

To first understand how cellular metabolism responds to different levels of saturated fatty acids, we first examined the effects of palmitate on the metabolism of the human Jurkat leukemia cell line. Culturing these cells in the presence of high concentrations of palmitate caused cell death (**Figures 2.4A & 2.4B**) and profound metabolic changes: acylcarnitines, which are intermediates

of beta oxidation, and triacylgycerols increased, as did levels of intermediates of lipid synthesis pathway such as ceramides, suggesting the utilization of exogenous fatty acids for beta oxidation and glycerolipid synthesis, respectively (**Figure 2.4C**). We next performed a set of CRISPR-based negative and positive selection screens for genes whose loss potentiates or protects against the toxicity of palmitate. These genes would be expected to be involved in processes that regulate the utilization of fatty acids and thus their identification will pinpoint key metabolic regulators of glycerolipid metabolism in proliferating cells. For negative and positive selection screens, we used a metabolism focused (Birsoy et al., 2015) and genome-wide CRISPR library (Wang et al., 2017), respectively (**Figure 2.4D**). We transduced Jurkat cells with these sgRNA libraries and passaged the pool of knockout cells for 14 population doublings in the presence or absence of 50-200 μM palmitate (**Figure 2.4D**). At the end of the screens, for each gene, we calculated its score as the median $\log_2$ fold change in the abundance of all sgRNAs targeting the gene. Validating the robustness of the screens, most genes, as well as the control sgRNAs, scored similarly in the presence or absence of palmitate (**Figures 2.4E**).

Among the genes selectively essential in the presence of palmitate (**Figure 2.4E**), many encode lipid metabolism enzymes involved in the incorporation of unsaturated lipids which maintain the balance of cellular lipid saturation. These genes include the major acyl-CoA synthetase for polyunsaturated fatty acids, ACSL4 (Klett et al., 2017) (**Figure S2.5A**), as well as SCAP, HSD17B12, AGPAT1 and CEPT1, genes known to contribute to unsaturated lipid synthesis (Agarwal et al., 2011; Henneberry and McMaster, 1999; Kemiläinen et al., 2016; Williams et al., 2013). Additionally, mammalian cells use fatty acid desaturases, which require the transfer of electrons via the heme-containing cytochrome b5 to introduce double bonds into acyl chains (Mitchell and Martin, 1995). Interestingly, both cytochrome b5 (CYB5B) and members of the heme synthesis pathway such as HMBS, UROD and ALAS1, scored as essential under palmitate treatment. These results are consistent with previous findings that a balance between saturated and unsaturated membrane lipids are essential for cell viability (Listenberger et al., 2003). Similarly, the top scoring gene in the positive selection screen was ACSL3 (**Figures 2.5B & 2.5C**), a member of the acyl-CoA synthetase family that preferentially uses saturated fatty acids as major substrates (Van Horn et al., 2005). Other scoring genes include CHP1 (**Figure 2.5C**), a poorly characterized gene with no known metabolic function, as well as GPAT4 and ACACA, enzymes of the glycerolipid synthesis pathway (Wendel et al., 2009).

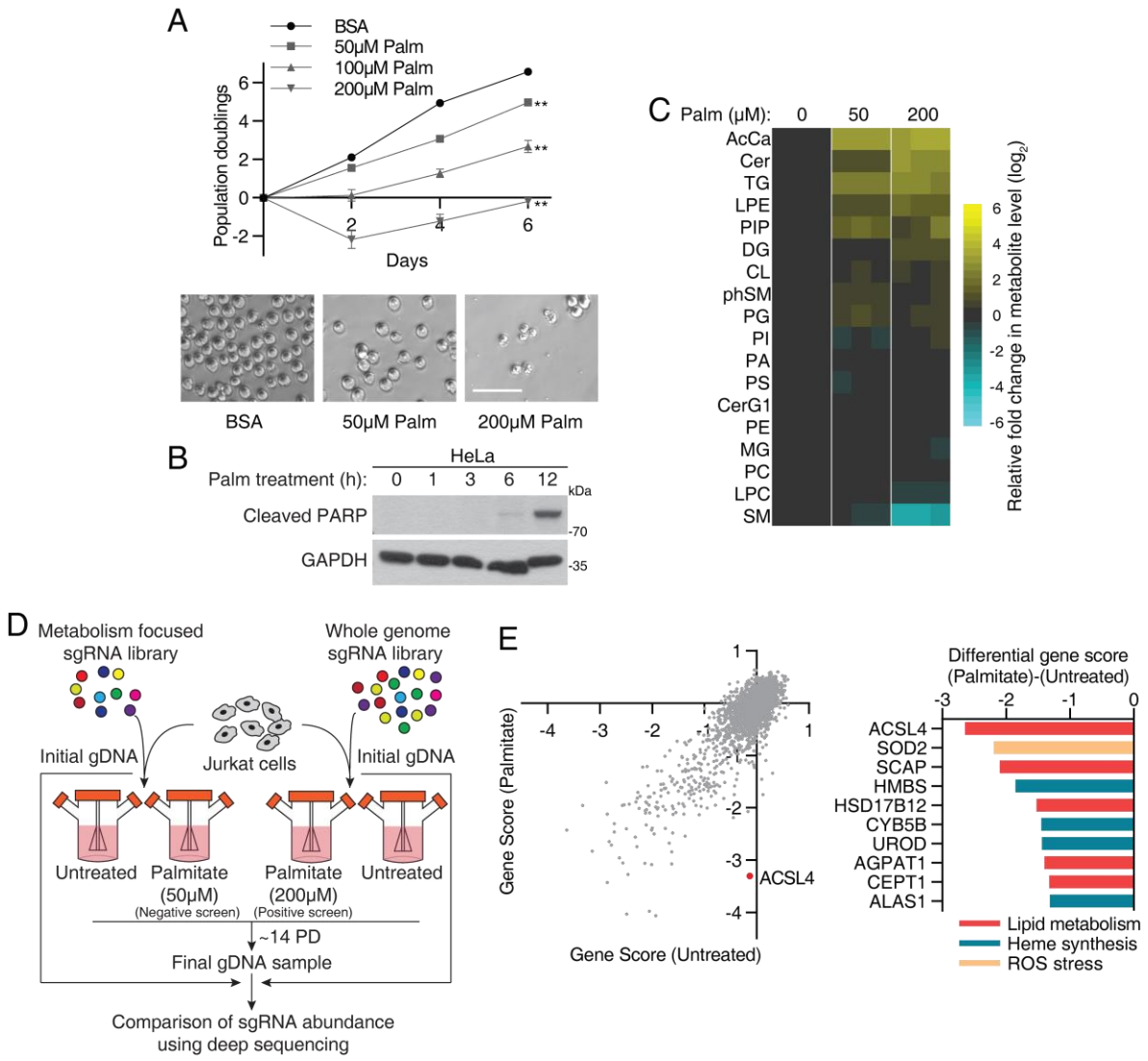

Figure 2.4. CRISPR screen to identify genetic regulators of glycerolipid synthesis and saturated fatty acid toxicity.

(**A**) Dose-dependent effects of palmitate on Jurkat cell proliferation (mean ± SD, n=3). ***p < 0.001 versus BSA control (top). Representative bright-field micrographs of Jurkat cells after a 6-day treatment with the indicated palmitate concentrations. Scale bar, 100 μm (bottom). (**B**) Immunoblot analysis of HeLa cells treated with 500 μM palmitate for the indicated durations. Cleaved PARP was used to show the extent of cell death. GAPDH was used as a loading control. (**C**) Relative abundance of indicated lipid groups in Jurkat cells treated with 50 uM or 200 uM palmitate after a 24-hour treatment. Lipid species of the same group were summed. Values were normalized to the average of the untreated controls (n=3). (**D**) Schematic depicting the negative and positive CRISPR based screens with palmitate. (**E**) Gene scores in untreated versus palmitate-treated (50 uM) Jurkat cells (left). Top 10 genes scoring as differentially required upon palmitate treatment. Genes linked to lipid metabolism are indicated in red, heme synthesis and desaturation in green, and ROS stress in yellow (right).

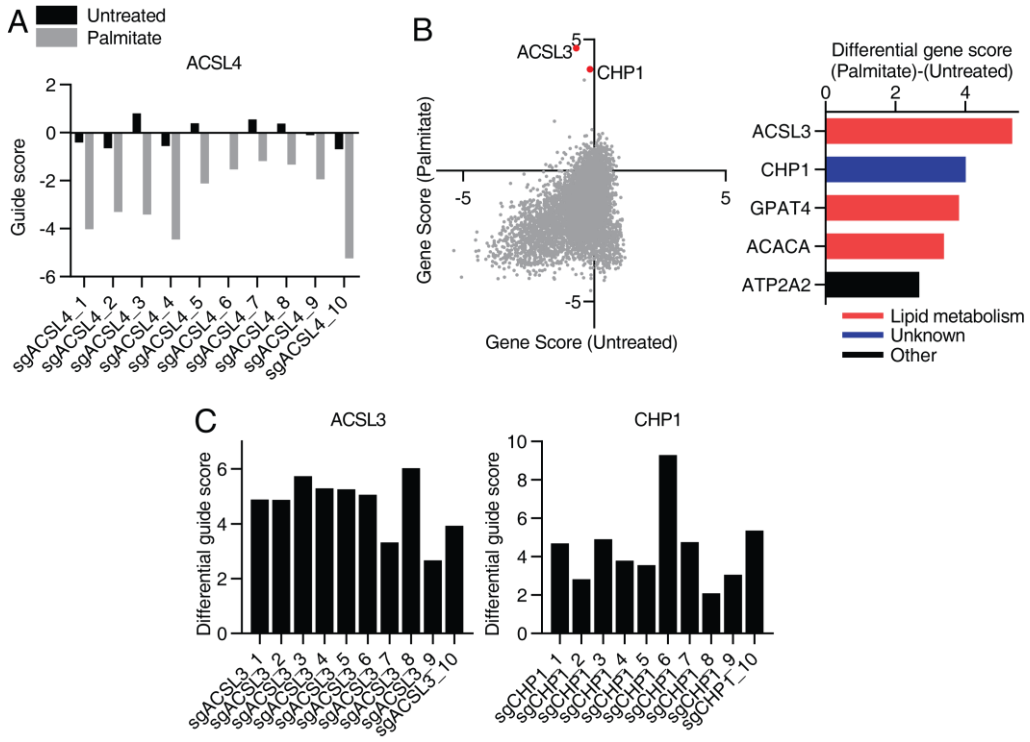

Figure 2.5. CRISPR screens identify ACSLs and CHP1 as main regulators of saturated fatty acid toxicity.
(**A**) Guide scores (log_2 fold change) of individual sgRNAs targeting ACSL4 used in the negative screen in the presence (gray) or absence (black) of palmitate. (**B**) Gene scores in untreated versus palmitate-treated (200 uM) Jurkat cells. Top 5 genes scoring as differentially required upon palmitate treatment. Genes linked to lipid metabolism are indicated in red. The second gene in the list, CHP1 (blue), does not have metabolism related annotations (right). (**C**) Differential guide scores ((palmitate)-(untreated)) of individual sgRNAs targeting ACSL3 and CHP1 used in the positive screen.

To confirm our screening results, we used the CRISPR-Cas9 system and, for each top scoring gene, generated two clonal Jurkat cell lines, in which ACSL4 (**Figure S2.6A**), ACSL3 (**Figure 2.6B**) and CHP1 (**Figure 2.6C**) proteins were undetectable. All knockout cell lines were viable and proliferated at similar rates to wild type cells. Consistent with the screening results, ACSL4 knockout cells arrested and died at low doses of palmitate, while the wild type counterparts did not (**Figure 2.6D**). In contrast, ACSL3 (**Figure 2.6E**) and CHP1 (**Figure 2.6F**) knockout cells were almost completely resistant to doses of palmitate that induced cell death in wild type cells. Notably, re-expression of sgRNA resistant cDNAs in the corresponding cell lines largely restored the wild type response to palmitate toxicity (**Figures 2.6D-F**). To address whether loss of these genes confers a similar response to palmitate in other cell types, we knocked out ACSL4, ACSL3 and CHP1 in human HeLa (**Figure 2.6G**) and HepG2 cells (**Figure 2.6H**) and observed similar responses to palmitate treatment, indicating a generalizable role for these genes in cellular fatty acid utilization. Overall, our findings suggest that ACSL3, ACSL4 and CHP1 are major regulators of glycerolipid metabolism. Given its uncharacterized role in lipid metabolism, we next focused our attention on CHP1.

Figure 2.6. Loss of ACSL4 sensitizes while loss of ACSL3 or CHP1 protects against saturated fatty acid toxicity.

(**A**) Relative cell numbers of Jurkat wild type (black) and two clones of ACLS4_KO cells (blue) after a 4-day treatment with the indicated palmitate concentrations. Cell numbers were normalized to the untreated control (mean ± SD, n=3). *p < 0.05 versus wild type. (**B**) Relative cell numbers of Jurkat wild type (black) and two clones of ACLS3_KO cells (blue) after a 4-day treatment with the indicated palmitate concentrations. Cell numbers were normalized to the untreated control (mean ± SD, n=3). **p < 0.01, ***p < 0.001 versus wild type. (**C**) Relative cell numbers of Jurkat wild type (black) and two clones of CHP1_KO cells (blue) after a 4-day treatment with the indicated palmitate concentrations. Cell numbers were normalized to the untreated control (mean ± SD, n=3). **p < 0.01, ***p < 0.001 versus wild type. (**D**) Immunoblot analysis of wild type, ACSL4_KO, and rescued KO cells. β-actin was used as a loading control (left). Fold change in cell number (log_2) of wild type (black), ACSL4_KO (blue), and rescued ACSL4_KO (gray) cells after a 4-day treatment with the indicated palmitate concentrations (mean ± SD, n=3). ***p < 0.001 versus wild type (right). (**E**) Immunoblot analysis of wild type, ACSL3_KO, and rescued KO cells. β-actin was used as a loading control (left). Fold change in cell number (log_2) of wild type (black), ACSL3_KO (blue), and rescued ACSL3_KO (gray) cells after a 4-day treatment with the indicated palmitate concentrations (mean ± SD, n=3). ***p < 0.001 versus wild type (right). (**F**) Immunoblot analysis of wild type, CHP1_KO, and rescued KO cells. β-actin was used as a loading control (left). Fold change in cell number (log_2) of wild type (black), CHP1_KO (blue), and rescued CHP1_KO (gray) cells after a 4-day treatment with the indicated palmitate concentrations (mean ± SD, n=3). ***p < 0.001 versus wild type (right). (**G**) Palmitate sensitivity of HeLa cells upon loss of indicated genes. Immunoblot analysis of wild type, ACSL4_KO, ACSL3_KO and CHP1_KO HeLa cells. β-actin was used as a loading control (left). Fold change in cell number (log_2) of wild type (black), ACSL4_KO (blue), ACSL3_KO and CHP1_KO (gray) cells after a 4-day treatment with the indicated palmitate concentrations (mean ± SD, n=3). ***p < 0.001 versus wild type (right). (**H**) Fold change in cell number (log_2) of HepG2 wild type (black), ACSL4_KO (blue), ACSL3_KO and CHP1_KO (gray) cells after a 4-day treatment with the indicated palmitate concentrations (mean ± SD, n=3). *p < 0.05, **p < 0.01, ***p < 0.001 versus wild type.

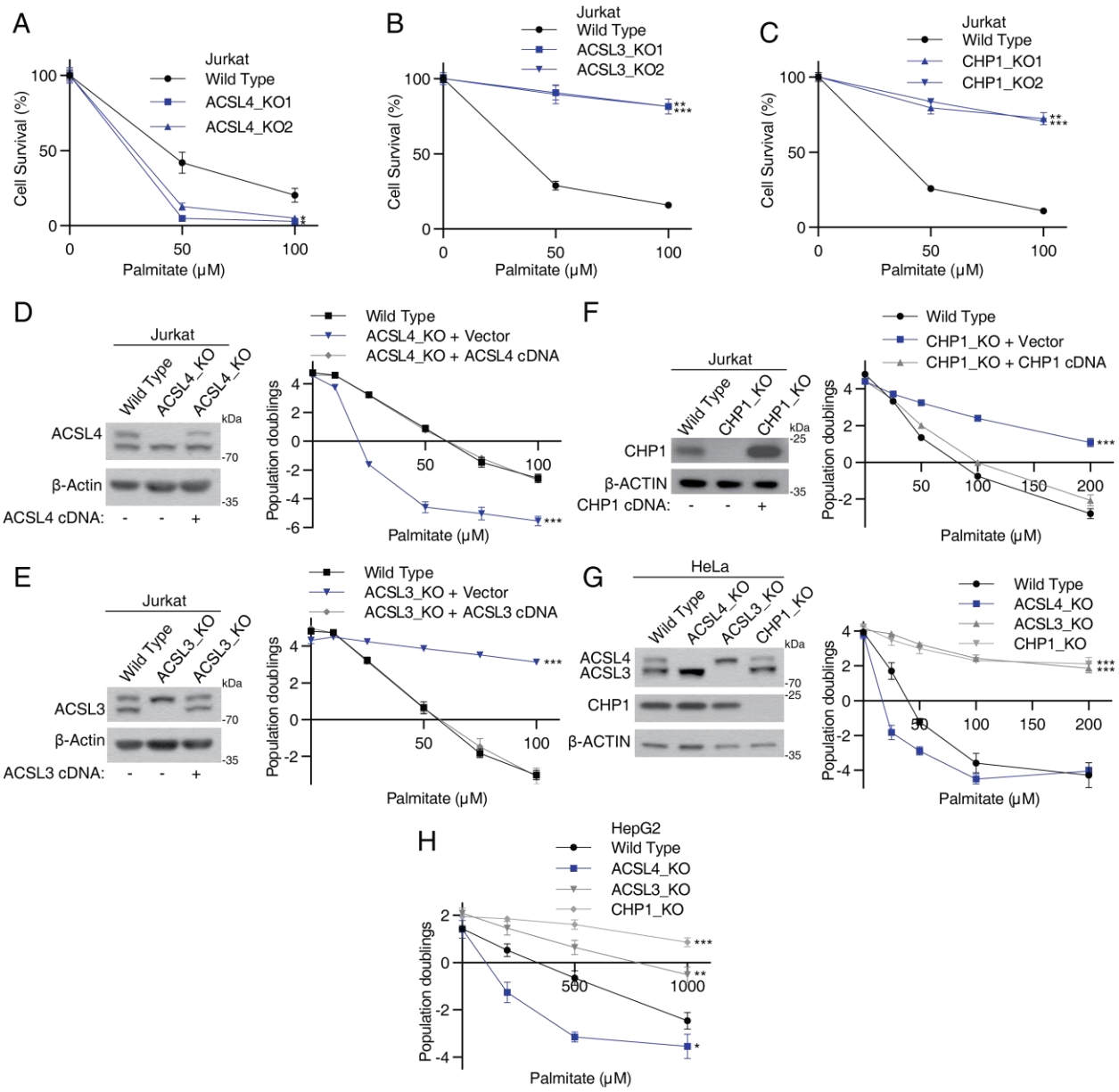
A
Jurkat
Wild Type
ACSL4_KO1
ACSL4_KO2
Cell Survival (%)
Palmitate (μM)
B
Jurkat
Wild Type
ACSL3_KO1
ACSL3_KO2
C
Jurkat
Wild Type
CHP1_KO1
CHP1_KO2
D
Jurkat
Wild Type
ACSL4_KO
ACSL4_KO
ACSL4
β-Actin
kDa
ACSL4 cDNA:
Wild Type
ACSL4_KO + Vector
ACSL4_KO + ACSL4 cDNA
Population doublings
Palmitate (μM)
E
Jurkat
Wild Type
ACSL3_KO
ACSL3_KO
ACSL3
β-Actin
ACSL3 cDNA:
Wild Type
ACSL3_KO + Vector
ACSL3_KO + ACSL3 cDNA
F
Jurkat
Wild Type
CHP1_KO
CHP1_KO
CHP1
β-ACTIN
CHP1 cDNA:
Wild Type
CHP1_KO + Vector
CHP1_KO + CHP1 cDNA
G
HeLa
Wild Type
ACSL4_KO
ACSL3_KO
CHP1_KO
ACSL4
ACSL3
CHP1
β-ACTIN
Wild Type
ACSL4_KO
ACSL3_KO
CHP1_KO
H
HepG2
Wild Type
ACSL4_KO
ACSL3_KO
CHP1_KO
Population doublings
Palmitate (μM)

2.4 CHP1 is necessary for glycerolipid synthesis from free fatty acids regardless of saturation

CHP1 belongs to the Ca^{+2}-binding protein subfamily and has previously been implicated in the regulation of the plasma membrane Na^{+}/H^{+} exchanger protein SLC9A1 function (Lin and Barber, 1996), but neither SLC9A1 nor other CHP family members scored in our genetic screens. We therefore sought to determine a direct role for CHP1 in lipid metabolism by performing lipidomic analysis. As the cellular imbalance of lipid saturation may impair cell proliferation, we first reasoned that CHP1 might influence cellular lipid saturation. Indeed, the two top scoring genes in our screens, ACSL3 and ACSL4, are members of the acyl-CoA synthetase family with preferences for saturated (e.g. palmitate) and polyunsaturated (e.g. arachidonate) fatty acids respectively (Klett et al., 2017; Van Horn et al., 2005). Consistent with their substrate choice, loss of ACSL3 or ACSL4 had opposing effects on cellular lipid saturation of triacylglycerols, the major storage glycerolipid species in mammalian cells. While ACSL3 loss decreased incorporation of saturated fatty acids into triacylglycerols, ACSL4 loss reduced mostly polyunsaturated fatty acids. However, loss of CHP1 decreased incorporation of both saturated and unsaturated fatty acids into triacylglycerols (**Figure 2.7A**).

Similar to palmitate, excess polyunsaturated fatty acids, such as arachidonate, are also toxic to mammalian cells (Pompeia et al., 2002), a phenotype rescued by supplementation of palmitate (**Figure 2.7B**). To test whether CHP1 is also involved in protecting against the toxicity of unsaturated fatty acid species in an unbiased way, we repeated our genetic screen with arachidonate (**Figure 2.7C**). ACSL3 and ACSL4 scored in an opposite fashion to their scores in the genetic screens using palmitate (**Figures 2.7D-E**). While loss of ACSL3 sensitized cells to arachidonate, ACSL4 and CHP1 loss protected them against its toxicity (**Figures 2.7E-F**). This raises the possibility that, unlike ACSL3 and ACSL4, CHP1 may be involved in the utilization of both saturated and unsaturated fatty acids. To further test this possibility, we visualized the incorporation of palmitate and arachidonate in wild type and CHP1 knockout cells using stimulated Raman scattering microscopy (Shen et al., 2014) with deuterium labeled palmitate (d_{31}-palmitate) and arachidonate (d_{11}-arachidonate). Upon treatment of deuterium labeled fatty acids, wild type cells displayed lamellar and punctate structures, which represent incorporated fatty acid metabolites in ER membranes and lipid droplets, respectively (Shen et al., 2017). However, unlike wild type cells, CHP1 knockouts failed to incorporate both fatty acids into membranes or lipid droplets (**Figures 2.8A-B**). Similarly, loss of CHP1 prevented lipid droplet formation in HeLa cells (**Figure 2.8C**) and differentiated mouse 3T3-F442A adipocytes (**Figures 2.8D-G**). These results suggest that CHP1 is essential for incorporating fatty acids to triacylglycerols and membrane lipids of mammalian cells.

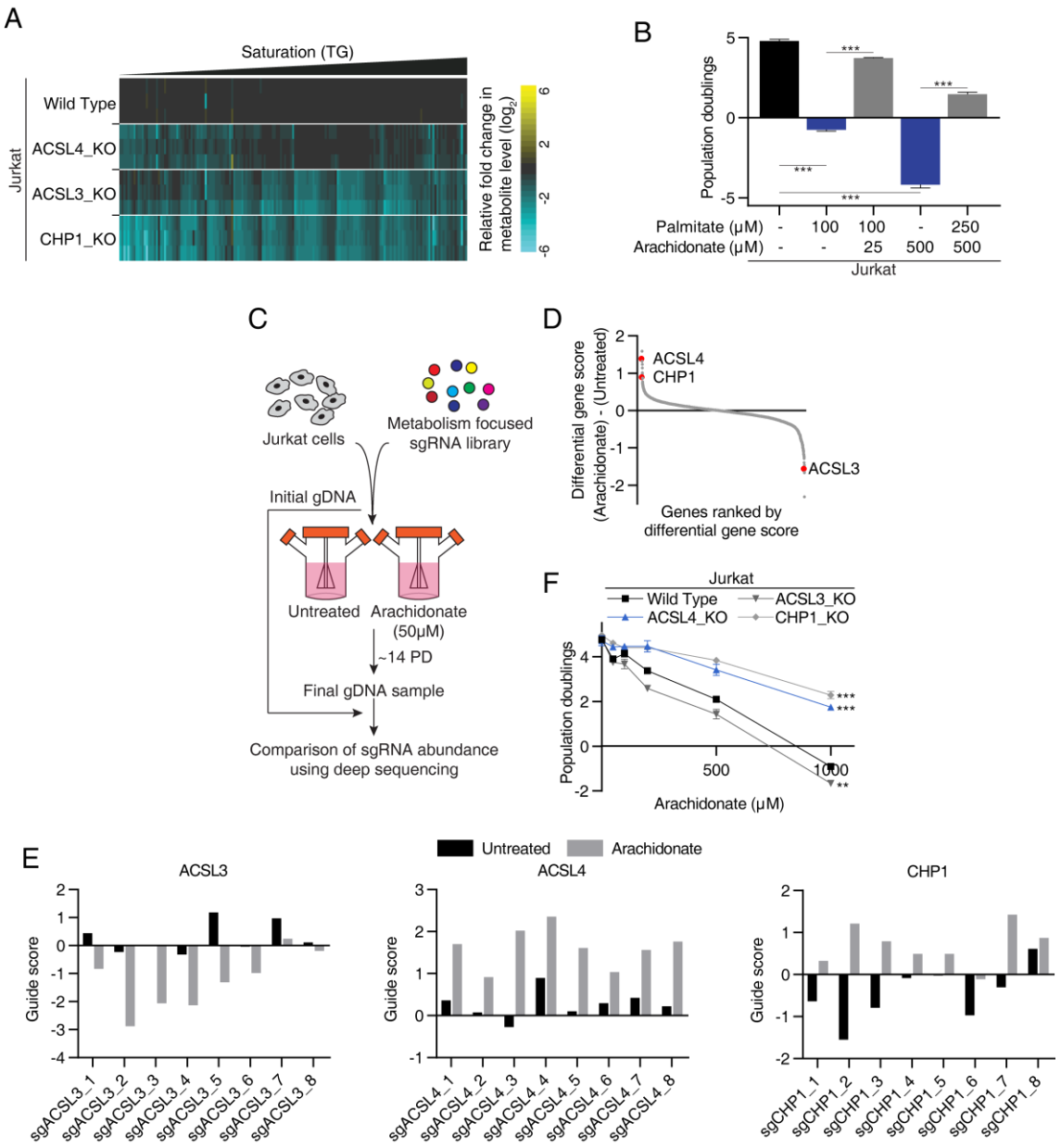

Figure 2.7. Unlike ACSLs, loss of CHP1 does not affect lipid saturation.
(**A**) Relative difference in abundance of triacylglycerol (TG) species ranked by saturation (number of double bonds) of the indicated cell lines. Values were normalized to the average of the wild type Jurkat cells (n=3). (**B**) Fold change in cell number (log_2) of Jurkat cells after a 4-day treatment with the indicated fatty acid concentrations (mean ± SD, n=3). ***p < 0.001. (**C**) Schematic depicting the negative CRISPR based screen with arachidonate. (**D**) Ranked differential gene scores of arachidonate-treated (50 uM) Jurkat cells relative to untreated controls. Gene scores for ACSL4, CHP1 and ACSL3 are indicated in red. (**E**) Guide scores (log_2 fold change) of individual sgRNAs targeting ACSL3, ACSL4 and CHP1 used in the arachidonate screen in the presence (gray) or absence (black) of arachidonate. (**F**) Fold change in cell number (log_2) of Jurkat wild type (black), ACSL4_KO (blue), ACSL3_KO and CHP1_KO (gray) cells after a 4-day treatment under the indicated arachidonate concentrations (mean ± SD, n=3). **p < 0.01, ***p < 0.001 versus wild type.

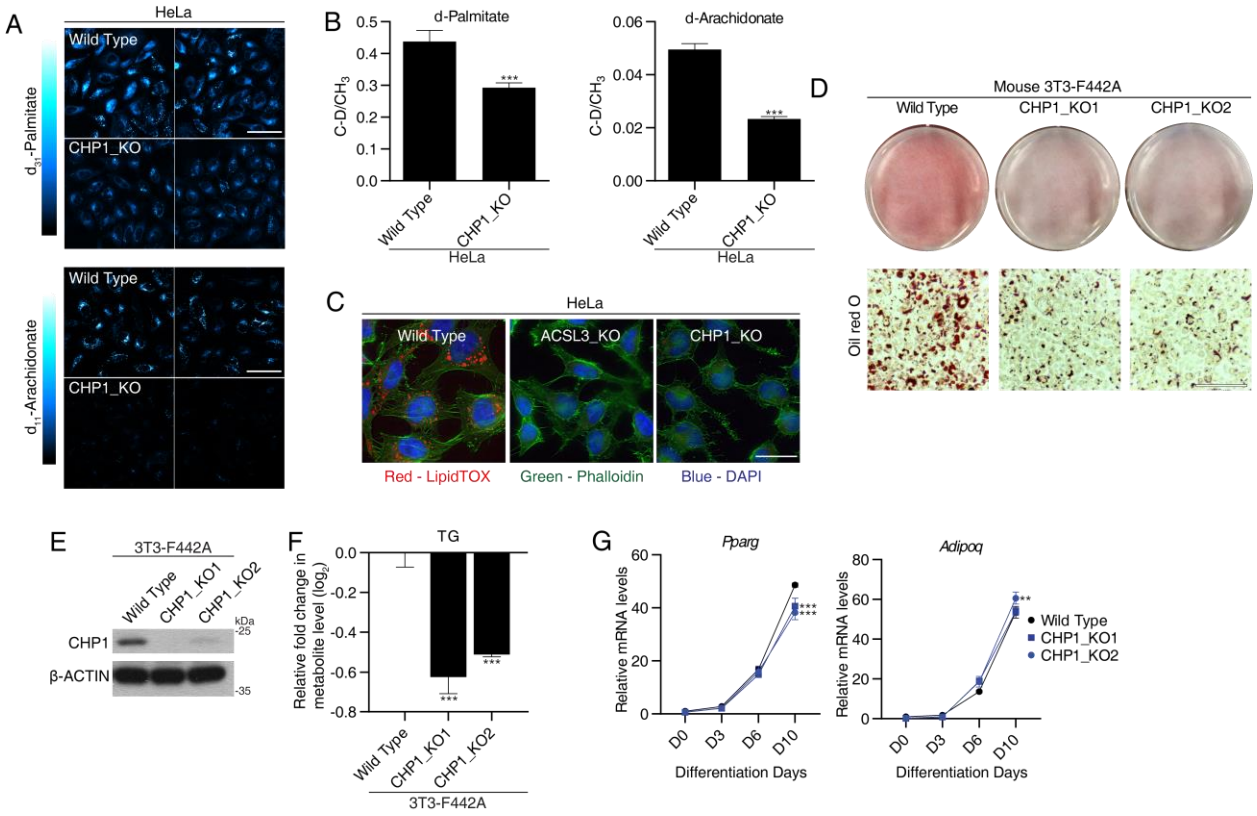

Figure 2.8. CHP1 enables fatty acid incorporation and lipid synthesis in human and mouse cells.

(**A**) Representative Stimulated Raman scattering imaging of deuterium-labeled palmitate (top) and arachidonate (bottom) treated HeLa wild type and CHP1_KO cells. Intensity indicates the relative concentrations of labeled fatty acid metabolites. Scale bar, 80 μm. (**B**) Normalized d-fatty acid abundance within wild type and CHP1_KO HeLa cells used in **Figure 2.8A** as indicated by C-D/CH_3 ratio. d-fatty acid intensity (C-D signal) was normalized to total protein intensity (CH_3 signal) to obtain normalized d-fatty acid level (mean ± SD, n=3). ***$p < 0.001$ versus wild type. (**C**) Representative fluorescence images of lipid droplet content in HeLa wild type, ACSL3_KO and CHP1_KO cells treated with 1mM oleate. Stains for neutral lipid (red), nucleus (blue) and cytoskeleton (green) were used. Scale bar, 30 μm. (**D**) Oil red O staining of mouse 3T3-F442A adipocytes. Pre-adipocytes were infected with a control or CHP1 sgRNA plasmids. Cells were then differentiated with a standard hormone cocktail and stained with oil red O. Images of wells (top) and representative micrographs (bottom) were shown. Scale bar, 150 μm. (**E**) Immunoblot analysis of wild type and CHP1_KO 3T3-F442A cells used in **Figure 2.8D**. β-actin was used as a loading control. (**F**) Fold change (log_2) in the abundance of triacylglycerols of wild type and CHP1_KO 3T3-F442A preadipocytes. Values were normalized to the average of the wild type cells (mean ± SD, n=3). ***$p < 0.001$ versus wild type. (**G**) Relative mRNA expression levels of indicated adipocyte differentiation markers in wild type and CHP1_KO 3T3-F442A cells collected on the indicated days upon start of differentiation. Minimal differences in differentiation were seen in the CHP1_KO cells. Expression levels were normalized to *Rpl32* (mean ± SD, n=3). **$p < 0.01$, ***$p < 0.001$ versus wild type.

2.5 CHP1 is essential for glycerolipid synthesis and accumulation in cancer cells

ACSLs catalyze the formation of fatty acyl-CoA esters, which in turn act as substrates for the synthesis of glycerolipids, cholesteryl esters and acyl-carnitines for β-oxidation. Given that ACSLs were the top-scoring genes in our screens, we reasoned that CHP1 loss may influence the function of ACSLs or other downstream enzymes. To address this, we measured steady state levels of different lipid species in CHP1 and ACSL3 knockout cells as well as wild type counterparts upon palmitate treatment using unbiased lipid profiling. Consistent with an upstream role in lipid metabolism, loss of ACSL3 resulted in a decrease in triacylglycerols, cholesteryl esters and acylcarnitines, all of which are derived from palmitoyl-CoA. CHP1 loss led to a similar decrease in triacylglycerols but, unlike ACSL3 loss, resulted in accumulation of cholesteryl esters and acylcarnitines, particularly in response to palmitate supplementation (**Figure 2.9A**). This phenotype was rescued by reintroduction of sgRNA resistant CHP1 cDNA (**Figure 2.9B**) but did not affect the cellular rate of fatty acid oxidation (**Figure 2.9C**). Additionally, CHP1 loss resulted in an increase in cellular palmitoyl-CoA levels (**Figure 2.9D**). This observation indicates a role for CHP1 downstream of ACSLs. To test this further, we performed a metabolite tracing experiment and measured the metabolic fate of uniformly ^{13}C labeled palmitate. Compared to wild type cells, CHP1 knockout cells displayed significantly reduced incorporation of single (M+16) and double (M+32) palmitoyl labeled triacylglycerols and phosphatidylcholines, but increased incorporation of M+16 labeled acylcarnitines (**Figure 2.9E**). These experiments suggest that CHP1 acts downstream of ACSLs to regulate glycerolipid synthesis (**Figure 2.9F**).

Figure 2.9. CHP1 regulates glycerolipid synthesis downstream of ACSLs.
(**A**) Heatmap (left) and bar graphs (right) indicating the relative change in abundance (log_2) of individual lipid species of Jurkat wild type, ACSL3_KO and CHP1_KO cells to untreated wild type controls. Cells were treated with control BSA or 50μM palmitate for 24 hrs prior to lipid extraction. (mean ± SD, n=3). **p < 0.01, ***p < 0.001. (**B**) Fold change (log_2) in indicated lipid groups of Jurkat wild type, CHP1_KO and rescued CHP1_KO cells treated with 50μM palmitate for 24 hrs prior to lipid extraction. Lipid species of the same group were summed. Values were normalized to the average of the wild type untreated cells (mean ± SD, n=3). ***p < 0.001. (**C**) Maximal exogenous fatty acid oxidation of wild type and CHP1_KO HeLa cells measured by Seahorse Fatty Acid Oxidation Assay (mean ± SD, n=3). (**D**) Fold change (log_2) in the abundance of palmitoyl-CoA of wild type, ACSL3_KO and CHP1_KO Jurkat cells treated with 50μM palmitate for 24 hrs prior to metabolite extraction. Values were normalized to the average of the untreated wild type cells (mean ± SD, n=3). **p < 0.01, ***p < 0.001. (**E**) Schematic depicting metabolic tracing of [U-^{13}C]-palmitate incorporation (left). Relative abundance of the labeled lipid species of the indicated Jurkat cell lines. Values were normalized to the average of the untreated controls (mean ± SD, n=3) (right). (**F**) CHP1 functions downstream of ACSLs, as its loss causes an increase in cholesteryl esters and acylcarnitines, but a decrease in glycerolipids.

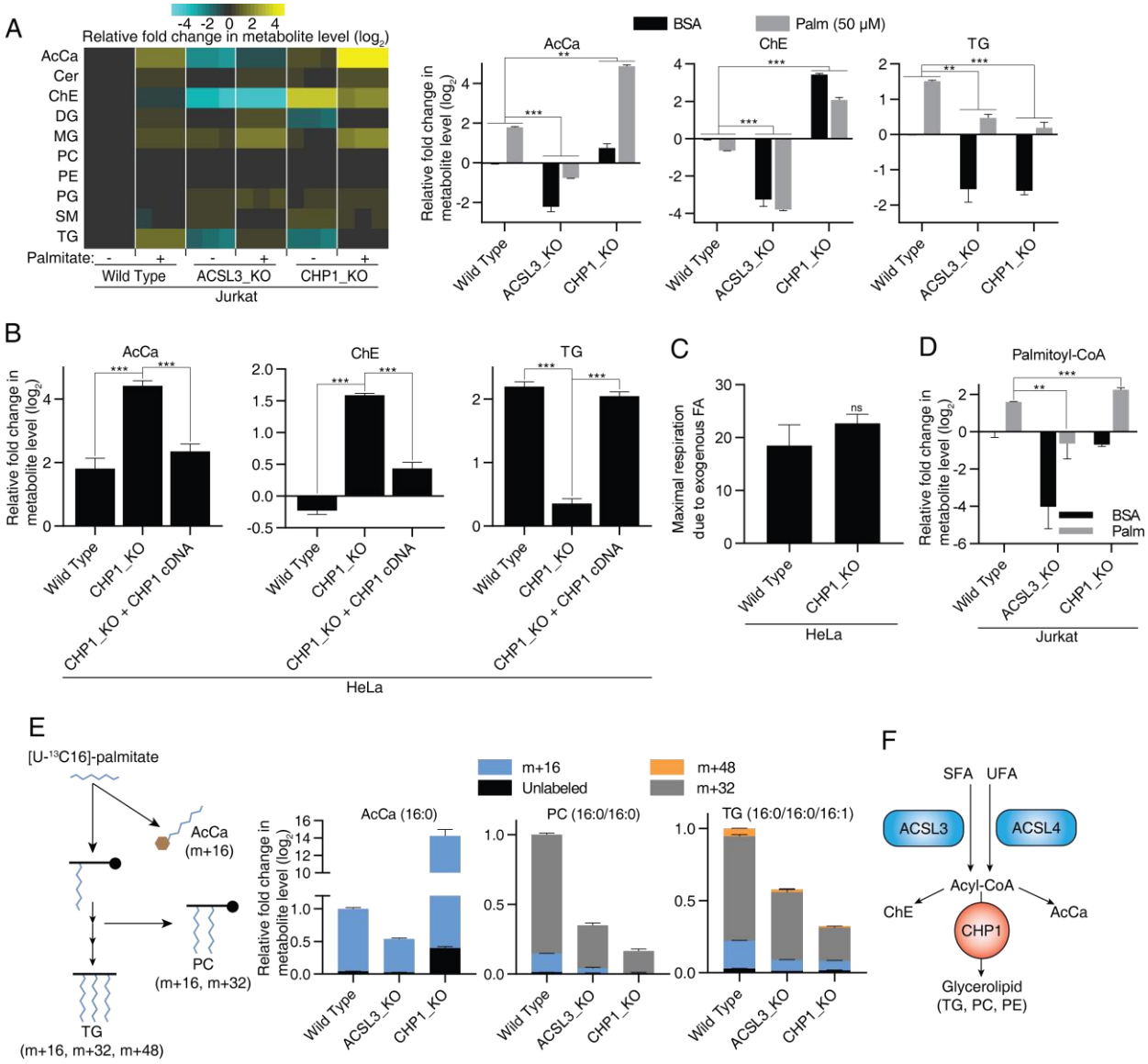
A
Relative fold change in metabolite level (log2)
AcCa
Cer
ChE
DG
MG
PC
PE
PG
SM
TG
Palmitate:
Wild Type
ACSL3_KO
CHP1_KO
Jurkat
BSA
Palm (50 μM)
Relative fold change in metabolite level (log2)
B
HeLa
C
Maximal respiration due to exogenous FA
ns
D
Palmitoyl-CoA
E
[U-13C16]-palmitate
AcCa (m+16)
PC (m+16, m+32)
TG (m+16, m+32, m+48)
m+16
Unlabeled
m+48
m+32
AcCa (16:0)
PC (16:0/16:0)
TG (16:0/16:0/16:1)
F
SFA
UFA
ACSL3
ACSL4
Acyl-CoA
ChE
AcCa
CHP1
Glycerolipid
(TG, PC, PE)

2.6 CHP1 interacts with GPAT4 to enable glycerolipid synthesis

We next sought to understand the precise mechanism by which CHP1 regulates glycerolipid synthesis. Amino acid sequence analysis of CHP1 protein did not reveal any obvious catalytic domain (**Figure 2.10A**). We therefore hypothesized that CHP1 might interact with other glycerolipid metabolism enzymes and regulate them. To identify such enzymes, we performed a mass spectrometric analysis of anti-FLAG immunoprecipitates from human Hela cells stably expressing FLAG-CHP1. This analysis consistently revealed the presence of proteins encoded by the two ER GPATs, GPAT3 and GPAT4, a top scoring gene in our genetic screen (**Figures 2.10B & 2.5B**). Further supporting this interaction, we detected CHP1 proteins in immunoprecipitates of HA-GPAT4 in a reciprocal mass spectrometric analysis (**Figure 2.10B**). To confirm the identification of CHP1 as a GPAT interacting protein, we overexpressed FLAG-CHP1 and found that CHP1, but not control GFP protein, co-immunoprecipitated ER GPATs (**Figure 2.10C**). This interaction is specific to ER GPATs as we did not observe any interaction between CHP1 and mitochondrial GPATs (GPAT1) in our mass spectrometry analysis and co-immunoprecipitation experiments. Interaction with CHP1 was also confirmed by co-immunoprecipitation using an antibody against endogenous GPAT4 (**Figure 2.10D**).

To study this relationship further, we determined biologically relevant gene associations with CHP1 using a publicly available CRISPR-Cas9 genetic screening data of 347 human cancer cell lines (Meyers et al., 2017). It has previously been shown that covariability in gene essentiality provides an efficient means of defining genes with similar biological functions (Wang et al., 2017). Analysis of coessential gene scores revealed that the essentiality of CHP1 correlated highly significantly with that of GPAT4 but not other GPAT family members (**Figure 2.11A**). These results were further confirmed with an independent CRISPR screen dataset (Wang et al., 2017) (**Figure 2.11B**). Consistent with a functional relationship between CHP1 and GPAT4, lipid profiles of CHP1 knockout cells correlate more significantly with those of GPAT4 knockout cells than GPAT3 knockout or wild type counterparts (**Figures 2.11C-D**). Additionally, GPAT4, but not GPAT3 knockout cells were resistant to palmitate toxicity in our genetic screens and cell viability experiments (**Figures 2.11E-F & 2.5B**), suggesting that GPAT4 is the major ER GPAT for glycerolipid synthesis.

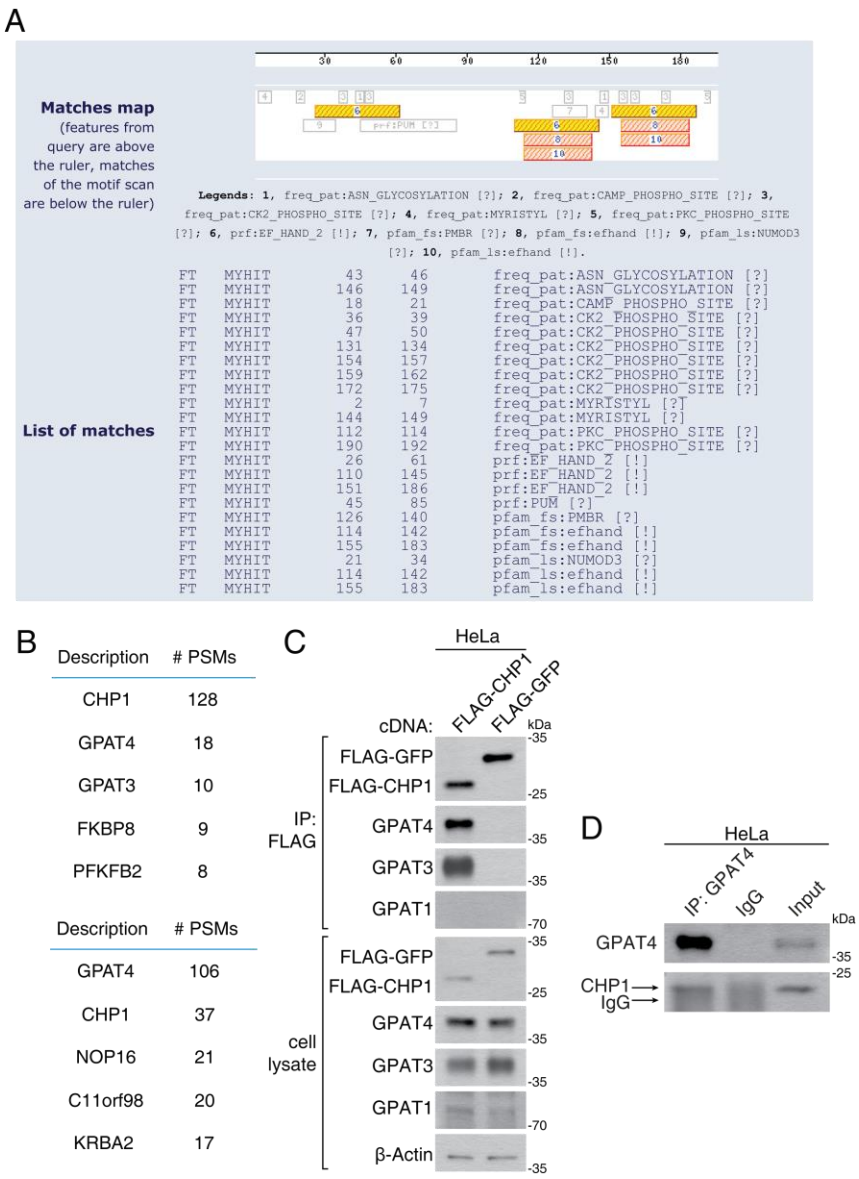

Figure 2.10. CHP1 interacts with ER enzymes GPAT4 and GPAT3.
(**A**) Motif analysis of CHP1 amino acid sequence. Analysis was carried out using MyHits (SIB). (**B**) Mass spectrometric analyses identified GPAT4 and GPAT3-derived peptides in immunoprecipitates prepared from HeLa cells expressing FLAG-tagged CHP1 (top). A reciprocal co-immunoprecipitation with HA-GPAT4 identified CHP1-derived peptides (bottom). Top 5 proteins in each experiment were shown. Peptide spectrum mass (PSM) indicates the total number of identified peptide spectra matched for the protein. (**C**) Recombinant FLAG-tagged CHP1 immunoprecipitates endogenous ER GPATs, GPAT4 and GPAT3. Anti-FLAG immunoprecipitates were prepared from HeLa cells expressing FLAG-CHP1 or FLAG-GFP. Cell lysates and immunoprecipiates were analyzed by immunoblotting for the indicated proteins. β-actin was used as a loading control. (**D**) Immunoprecipitation of endogenous GPAT4 protein in HeLa cells. Anti-GPAT4 immunoprecipitates were prepared from cell lysates and analyzed by immunoblotting for levels of indicated proteins.

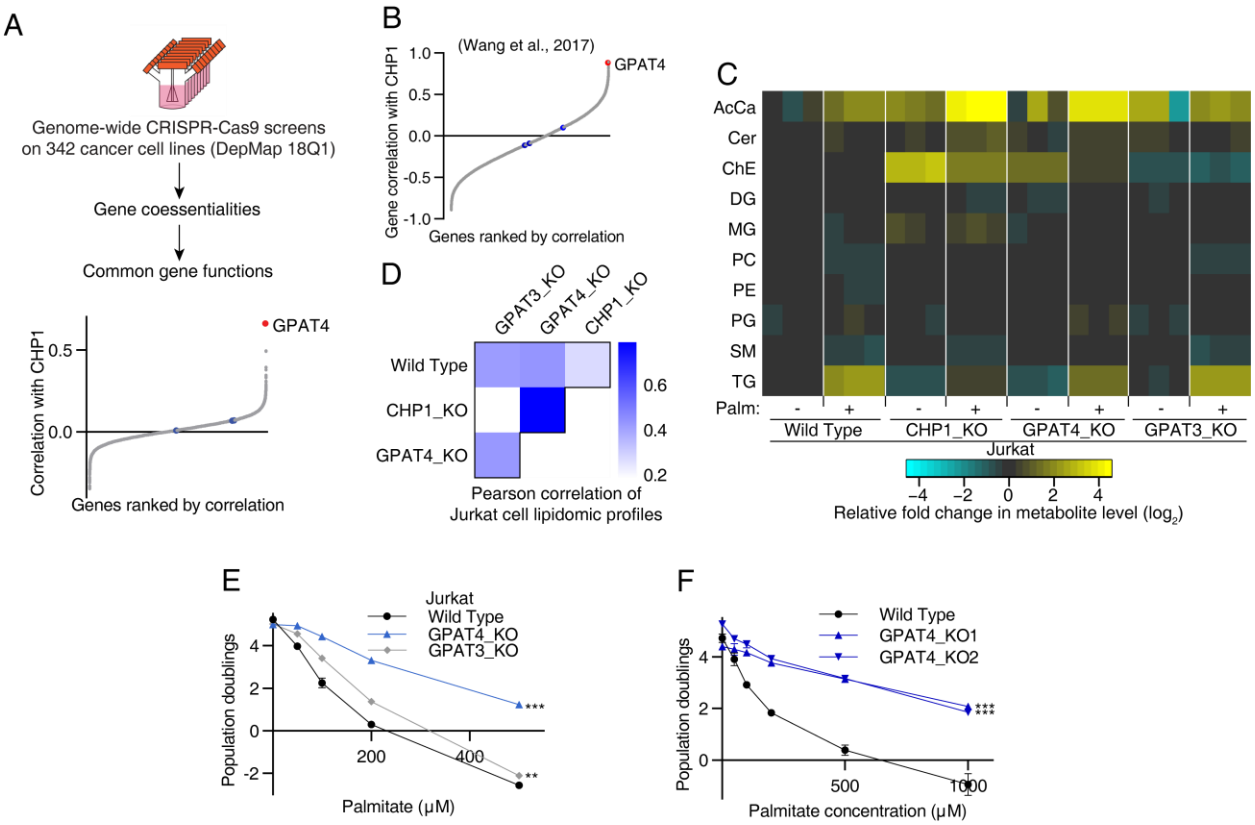

Figure 2.11. CHP1 and GPAT4 correlate genetically and phenotypically.
(**A**) Schematic depicting co-essentiality analysis using CRISPR screens in Meyers et al. (2017) (top). Correlations of gene essentialities of CHP1 with other genes were calculated and ranked. GPAT4 is indicated in red and other GPATs (GPAT1, GPAT2 and GPAT3) in blue (bottom). (**B**) CHP1 co-essentiality analysis using data from Wang et al. (2017). Gene correlation scores with CHP1 were calculated for all genes and ranked. The top co-essential gene is GPAT4 (red). Other GPATs (blue) do not correlate well with CHP1. (**C**) Changes in lipid profiles of Jurkat wild type, CHP1_KO, GPAT4_KO and GPAT3_KO cells treated with control BSA or 50μM palmitate for 24 hrs prior to lipid extraction. Lipid species of the same group were summed. Values were normalized to the average of the untreated wild type controls (n=3). (**D**) Correlation of total lipid profiles of Jurkat wild type, CHP1_KO, GPAT4_KO and GPAT3_KO cells treated with control BSA or 50μM palmitate for 24 hrs prior to lipid extraction. Pearson correlation coefficients of the relative abundance of all lipid species among each cell line were compared. (**E**) Fold change in cell number (log_2) of Jurkat wild type (black), GPAT4_KO (blue) and GPAT3_KO (gray) cells after a 4-day treatment with the indicated palmitate concentrations (mean ± SD, n=3). **p < 0.01, ***p < 0.001 versus wild type. (**F**) Fold change in cell number (log_2) of Jurkat wild type (black) and two clones of GPAT4_KO (blue) cells after a 4-day treatment with the indicated palmitate concentrations (mean ± SD, n=3). ***p < 0.001 versus wild type.

2.7 CHP1 enhances stability of GPAT4 and enables its enzymatic function

We next asked whether CHP1-GPAT4 interaction itself is required for glycerolipid synthesis. CHP1 and GPAT4 are more stable when they interact with each other, as loss of either protein reduces the levels of the interacting partner even though mRNA levels remain relatively unchanged (**Figures 2.12A-C**). To address this further, we performed a deletion analysis of GPAT4 protein and looked for GPAT4 mutants that no longer bind CHP1. Large terminal deletions of GPAT4 revealed that the N-terminus of the protein is responsible for its interaction with CHP1 (**Figures 2.13A-C**). Smaller deletions within the N-terminal region identified a conserved 113-126 amino acid region as necessary for this interaction (**Figure 2.13D**), regardless of the reduced CHP1 protein level due to GPAT4 loss (**Figure 2.13E**). GPAT4 is an ER membrane protein, but loss of CHP1 interaction did not alter its ER localization (**Figures 2.14A-B**). To test the necessity of the CHP1-GPAT4 interaction in glycerolipid synthesis, we expressed wild type and CHP1-interaction deficient (113-119del) GPAT4 cDNA in GPAT4 knockout cells. Unlike wild type GPAT4 cDNA, introduction of the CHP1-interaction deficient GPAT4 cDNA failed to restore the decrease in triacylglycerol levels (**Figure 2.14C**) or palmitate sensitivity (**Figure 2.14D**). These experiments demonstrate that CHP1-GPAT4 interaction is essential to enable glycerolipid synthesis in mammalian cells.

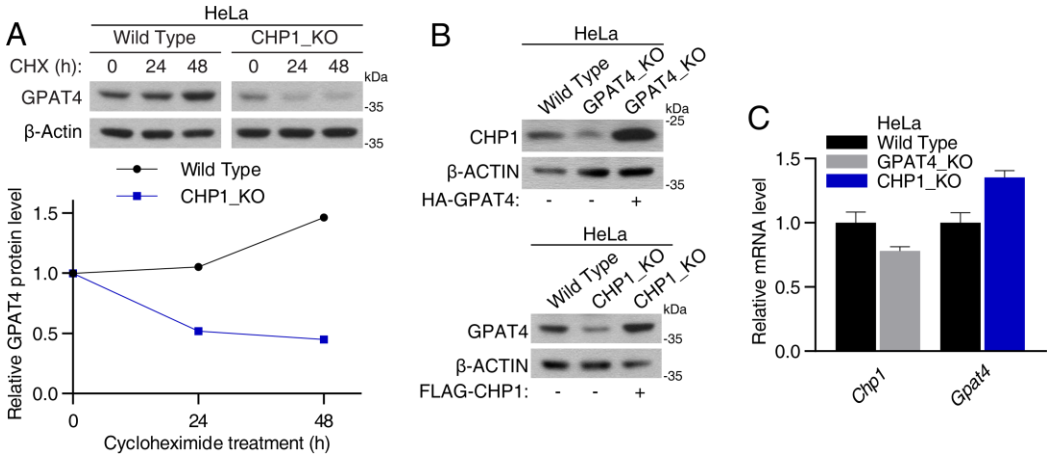

Figure 2.12. Loss of CHP1 of GPAT4 destabilizes the interaction partner.
(**A**) Immunoblot analysis of HeLa wild type and CHP1_KO cells treated with 100μg/mL cycloheximide for the indicated durations. β-actin was used as a loading control (top). Densitometry analysis of GPAT4 protein levels from the above immunoblot. GPAT4 level was normalized to the initial (t=0) (bottom). (**B**) Immunoblot analysis of HeLa wild type, GPAT4_KO, rescued GPAT4_KO, CHP1_KO and rescued CHP1_KO cells. β-actin was used as a loading control. (**C**) Relative mRNA expression levels of *Chp1* and *Gpat4* in the indicated HeLa cell lines. Expression levels were normalized to *Rpl32* (mean ± SD, n=3).

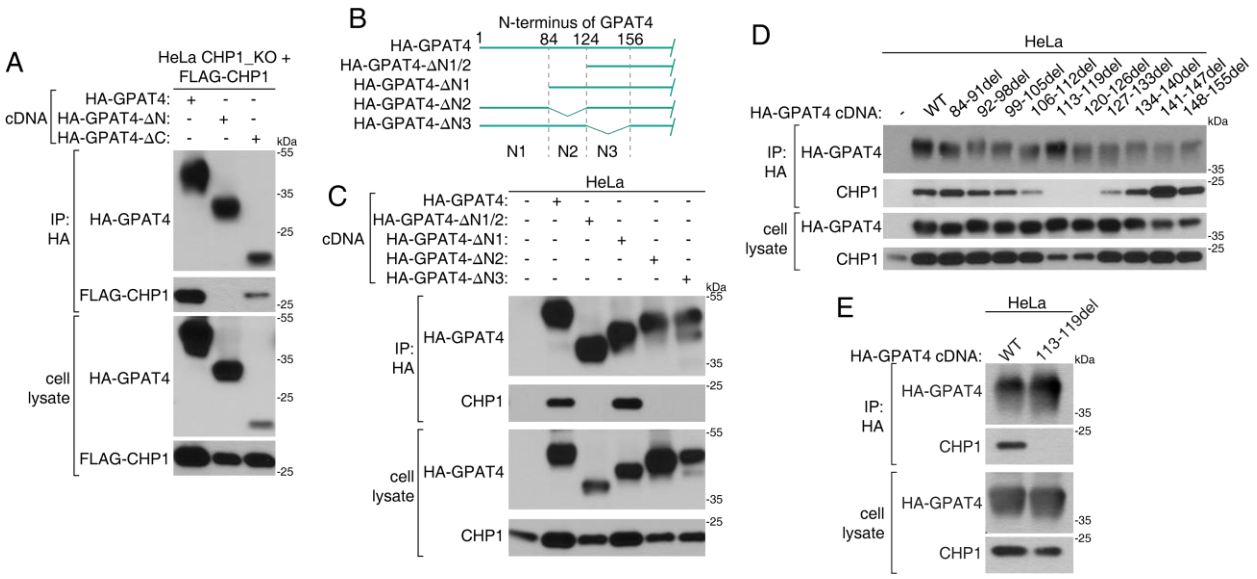

Figure 2.13. Deletion of a GPAT4 N-terminal domain prevents binding to CHP1.
(**A**) Identification of terminal regions of GPAT4 responsible for CHP1 interaction. Plasmids containing cDNA for HA-GPAT4 mutants with N- or C-terminal deletions, as well as full length HA-GPAT4, were expressed in HeLa rescued CHP1_KO cells. Immunoblot of co-immunoprecipitates with the indicated HA-GPAT4 constructs. (**B**) Indicated deletions and full length HA-tagged GPAT4 cDNAs were expressed in HeLa cells. (**C**) Interaction of CHP1 with large N-terminal deletions of HA-tagged GPAT4. Indicated deletions and full-length HA-tagged GPAT4 cDNA were expressed in HeLa cells. Anti-HA immunoprecipitates were prepared from cell lysates and analyzed by immunoblotting for levels of indicated proteins. (**D**) Interaction of CHP1 with HA-tagged GPAT4 lacking regions between amino acids 84-156. Indicated deletions and full-length HA-tagged GPAT4 cDNA were expressed in HeLa cells. Anti-HA immunoprecipitates were prepared from cell lysates and analyzed by immunoblotting for levels of indicated proteins. (**E**) Interaction of CHP1 with full length and small 113-119del HA-tagged GPAT4 accounting for the reduction of CHP1 levels in GPAT4_KO cells. Indicated deletion and full-length HA-tagged GPAT4 cDNA were expressed in HeLa cells. Anti-HA immunoprecipitates were prepared from cell lysates of cells expressing full length and 3X the amount of cells expressing 113-119del HA-GPAT4 and analyzed by immunoblotting for levels of indicated proteins.

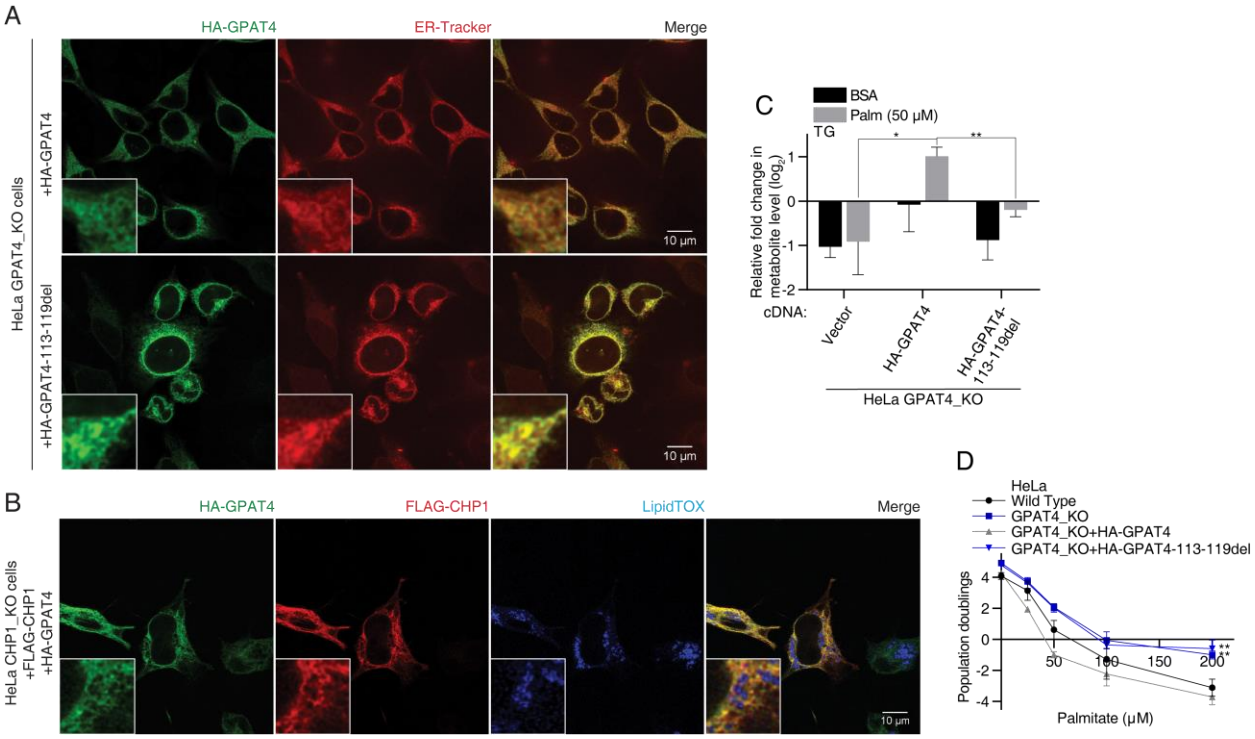

Figure 2.14. Loss of binding domain to CHP1 abrogates GPAT4 function without affecting its localization.

(**A**) Representative confocal immunofluorescence images of HeLa GPAT4_KO cells expressing wild type or interaction deficient (113-119del) HA-GPAT4. Stains for HA (green) and ER (red) were used. Insets show 5X magnified images. Scale bar, 10 µm. (**B**) Representative confocal immunofluorescence images of HeLa CHP1_KO cells expressing FLAG-CHP1 and HA-GPAT4, treated with 1mM oleate. Stains for HA (green), FLAG (red) and neutral lipids (blue) were used. Insets show 5X magnified images. Scale bar, 10 µm. (**C**) Fold change (log_2) in the abundance of triacylglycerols of HeLa GPAT4_KO cells expressing vector, HA-GPAT4 and HA-GPAT4-113-119del cDNA treated with 50µM palmitate for 24 hrs prior to lipid extraction. Values were normalized to the average of the untreated GPAT4_KO cells expressing HA-GPAT4 (mean ± SD, n=3). *$p < 0.05$, **$p < 0.01$. (**D**) Fold change in cell number (log_2) of HeLa wild type (black), GPAT4_KO (blue), GPAT4_KO expressing HA-GPAT4 (gray) and HA-GPAT4-113-119del (blue) cells after a 4-day treatment with the indicated palmitate concentrations (mean ± SD, n=3). **$p < 0.01$ versus wild type.

2.8 CHP1 activates GPAT4 through its myristoyl moiety

Given the requirement of the CHP1-GPAT4 interaction for glycerolipid synthesis, we reasoned that CHP1 may modulate GPAT4 catalytic activity. To test this, we performed a GPAT activity assay using ^{14}C labeled glycerol-3-phosphate as substrate in wild type and CHP1 knockout HeLa cells. Indeed, loss of CHP1 reduced cellular GPAT enzyme activity to the levels seen in GPAT4/GPAT3 double knockout cells, indicating a requirement for CHP1 in ER GPAT activity (**Figure 2.15A**).

We next sought to determine how CHP1 may activate GPAT4. CHP1 protein contains *1*) a myristoylation signal (MGSRAS); *2*) two functional EF-hand Ca^{2+}-binding domains (EF3-EF4); and *3*) two nuclear export signals (NES) (**Figure 2.15B**). We mutated key CHP1 protein residues to disrupt myristoylation (G2A/S6A), calcium binding (D123A/D125A/D127A/D164A/D166A/D168A) and the nuclear export signal (V138A/L139A/V179A/L180A) and stably expressed them in a CHP1 knockout HeLa cell line. Expression of the wild type or calcium binding deficient CHP1 restored sensitivity to palmitate toxicity, but mutants of the myristoylation site or the nuclear export signal failed to do so (**Figure 2.15C**). This suggests that cytoplasmic localization and myristoylation of CHP1 are essential for its metabolic function, while calcium binding is not.

Myristoylation, the addition of a 12-carbon fatty acyl chain, plays important roles in protein-protein interaction and targeting proteins to cellular membranes, regulating diverse cellular functions (Farazi et al., 2001). Interestingly, blocking myristoylation of CHP1 did not change the localization of CHP1 (**Figure 2.16A**) or its interaction with GPAT4 in co-immunoprecipitation experiments (**Figure 2.16B**). As myristoylation can also modulate protein structure and activity (Hantschel et al., 2003), we asked whether CHP1 myristoylation is required for GPAT4 to be active. We therefore performed GPAT activity assays in CHP1 knockout cells and isogenic counterparts complemented with wild type and myristoylation mutant CHP1 cDNA. While expression of wild type CHP1 cDNA induced GPAT activity ~20 fold, myristoylation mutant CHP1 cDNA failed to activate GPATs in CHP1 knockout cells (**Figure 2.16C**). Consistent with this, reintroduction of wild type but not myristoylation mutant CHP1 cDNA restored triacylglycerol, cholesteryl ester and acylcarnitine levels of CHP1 knockout cells (**Figure 2.16D**). To test whether the myristoyl group on CHP1 also makes direct intermolecular contacts with GPAT4, we used x-alk-16, a bi-functional fatty acid reporter that contains a clickable alkyne and a photo-activatable diazirine which can crosslink proteins in its close vicinity (Peng and Hang, 2015) (**Figure 2.17A**). Similar to myristate, x-alk-16 can incorporate into wild type CHP1 and not the myristoylation mutant counterpart (**Figure 2.17B**). In these experiments, only wild type, but not myristoylation deficient CHP1, effectively co-immunoprecipitated GPAT4 upon photocrosslinking, confirming a contact between the CHP1 myristoyl moiety and GPAT4 (**Figures 2.17C-D**). Altogether, our results show that CHP1 must interact with GPAT4 but also be myristoylated to fully activate GPAT4 for enabling glycerolipid synthesis at the endoplasmic reticulum (**Figure 2.17E**).

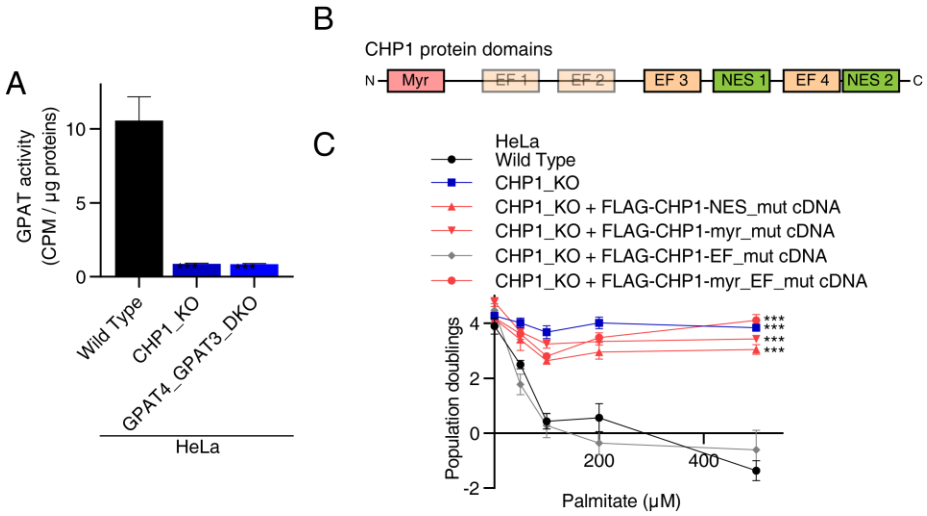

Figure 2.15. Loss of CHP1's myristoylation domain abrogates its function in glycerolipid metabolism.

(**A**) Radiolabeled GPAT activity assay of the indicated HeLa cell lines. Cell lysates were incubated with [^{14}C]-glycerol-3-phosphate. GPAT activity was quantified as the CPM in the non-polar fraction (mean ± SD, n=3). ***p < 0.001 versus wild type. (**B**) Schematic of functional protein domains of CHP1. (**C**) Identification of functionally relevant residues of CHP1 in glycerolipid metabolism. Fold change in cell number (log_2) of HeLa wild type (black), CHP1_KO (blue), CHP1_KO expressing FLAG-CHP1-EF_mut (D123A/D125A/D127A/D164A/D166A/D168A) (gray), FLAG-CHP1-NES_mut (V138A/L139A/V179A/L180A), FLAG-CHP1-myr_mut (G2A/S6A) and FLAG-CHP1-myr_EF_mut (G2A/S6A/D123A/D125A/D127A/D164A/D166A/D168A) (red) cells after a 4-day treatment with the indicated palmitate concentrations (mean ± SD, n=3). ***p < 0.001 versus wild type.

Figure 2.16. Loss of CHP1 myristoylation domain abrogates GPAT4's enzymatic activity and glycerolipid synthesis.

(**A**) Representative confocal immunofluorescence images of HeLa CHP1_KO cells expressing wild type or myristoylation mutant FLAG-CHP1. Stains for FLAG (green) and ER (red) were used. Insets show 5X magnified images. Scale bar, 10 μm. (**B**) Immunoblot of co-immunoprecipitates with the indicated FLAG-CHP1 constructs. β-actin was used as a loading control. (**C**) GPAT activity assay of HeLa CHP1_KO cells expressing vector, FLAG-CHP1 and FLAG-CHP1-myr_mut cDNAs. All cell lines are additionally infected with an HA-GPAT4 virus. Immunoblotting analysis of the indicated proteins. β-actin was used as a loading control (top). Cell lysates were incubated with [^{14}C]-glycerol-3-phosphate and with or without palmitoyl-CoA. GPAT activity was quantified as the CPM in the non-polar fraction (mean ± SD, n=3). **p < 0.01, ***p < 0.001 versus CHP1_KO expressing FLAG-CHP1 (bottom). (**D**) Fold change (log_2) in indicated lipid groups of HeLa CHP1_KO cells expressing vector, FLAG-CHP1 and FLAG-CHP1-myr_mut cDNAs treated with 50μM palmitate for 24 hrs prior to lipid extraction. Lipid species of the same group were summed. Values were normalized to the average of the untreated CHP1_KO cells expressing FLAG-CHP1 cDNA (mean ± SD, n=3). **p < 0.01, ***p < 0.001 versus CHP1_KO expressing FLAG-CHP1 cDNA.

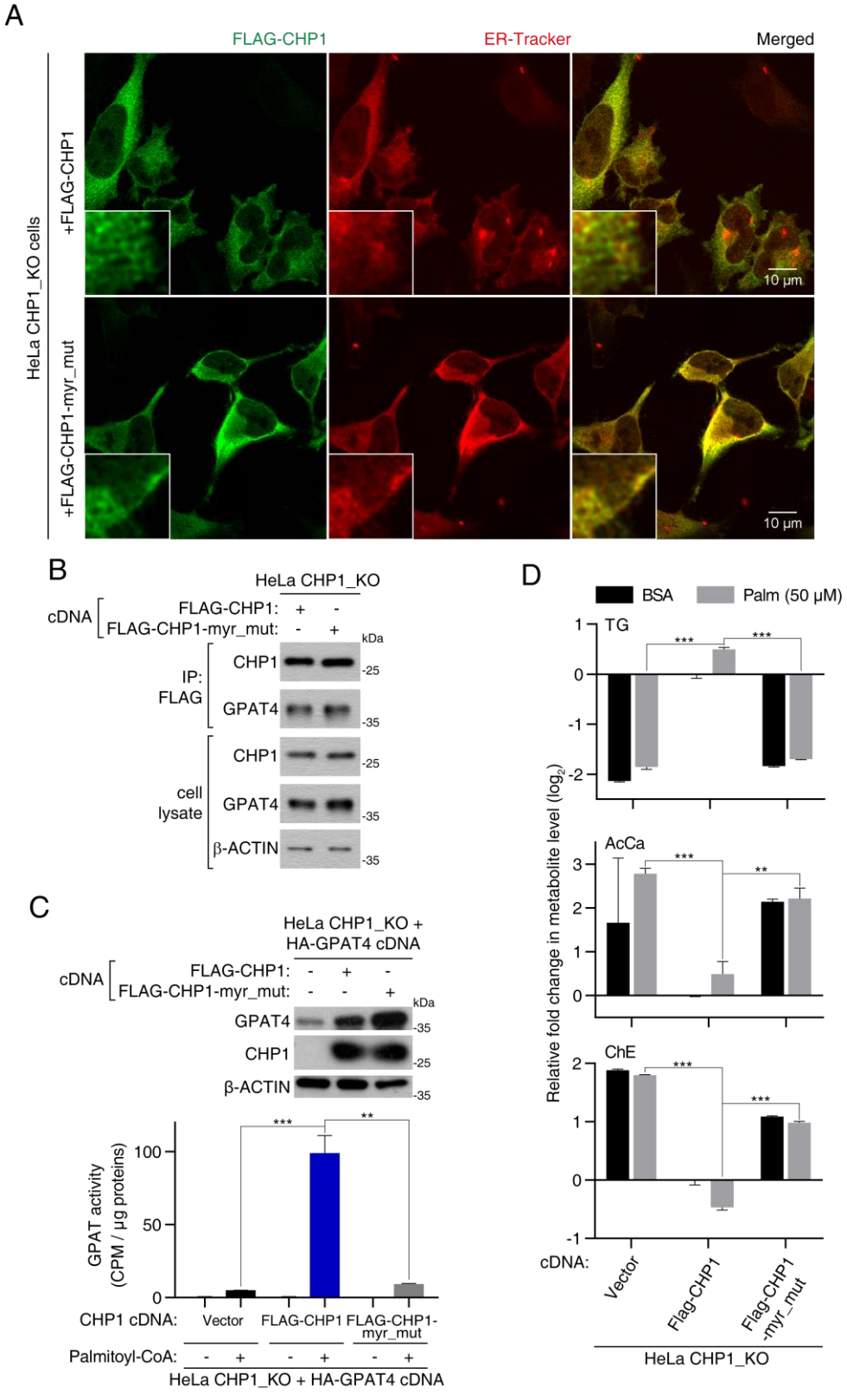
A
FLAG-CHP1
ER-Tracker
Merged
HeLa CHP1_KO cells
+FLAG-CHP1
+FLAG-CHP1-myr_mut
10 μm
10 μm
B
HeLa CHP1_KO
cDNA
FLAG-CHP1: + -
FLAG-CHP1-myr_mut: - +
kDa
IP: FLAG
CHP1
GPAT4
-25
-35
cell lysate
CHP1
GPAT4
β-ACTIN
C
HeLa CHP1_KO + HA-GPAT4 cDNA
FLAG-CHP1: - + -
FLAG-CHP1-myr_mut: - - +
GPAT4
CHP1
β-ACTIN
GPAT activity (CPM / μg proteins)
CHP1 cDNA: Vector FLAG-CHP1 FLAG-CHP1-myr_mut
Palmitoyl-CoA:
HeLa CHP1_KO + HA-GPAT4 cDNA
D
BSA
Palm (50 μM)
TG
AcCa
ChE
Relative fold change in metabolite level (log2)
cDNA: Vector Flag-CHP1 Flag-CHP1-myr_mut
HeLa CHP1_KO

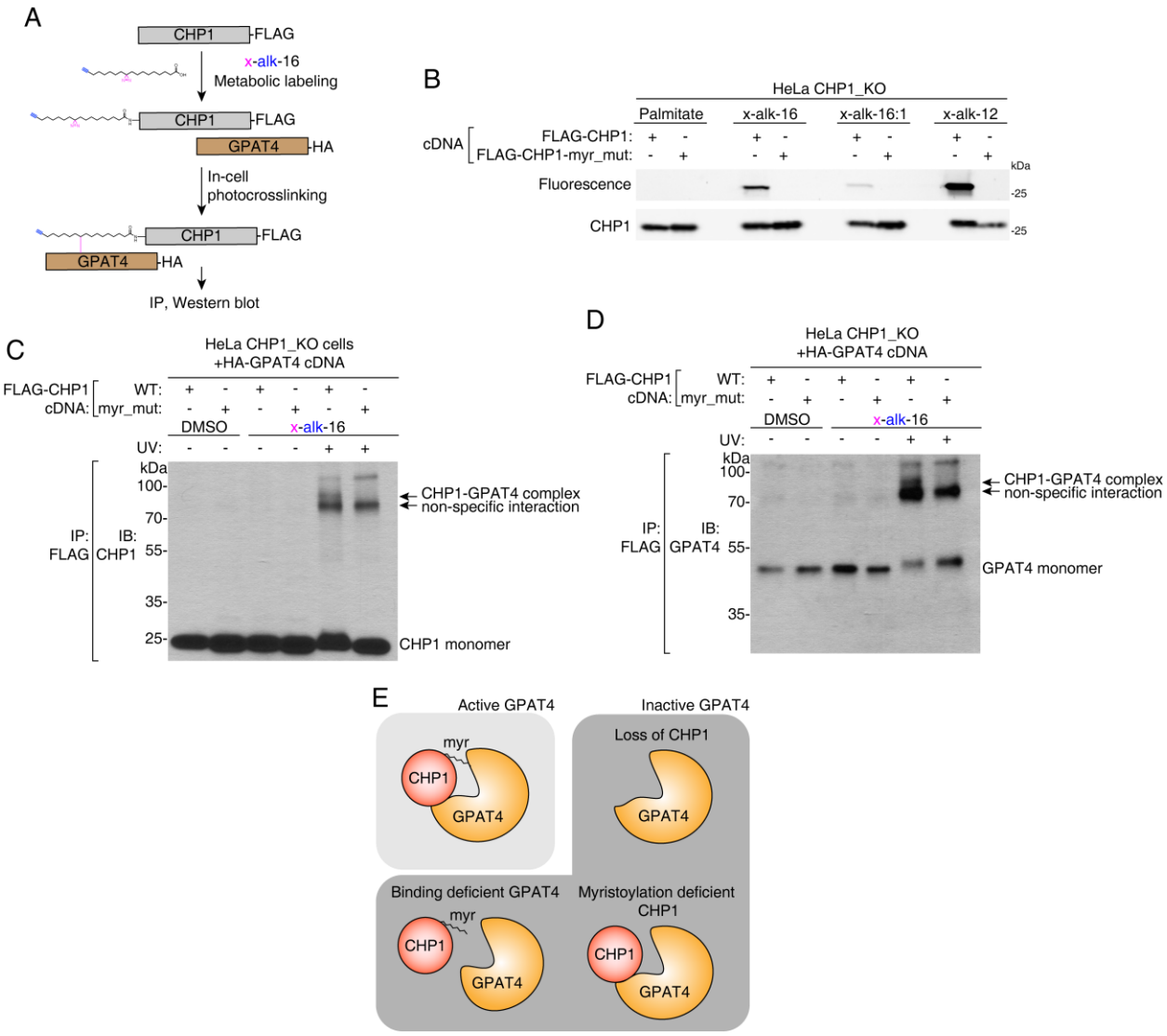

Figure 2.17. CHP1's myristoylation moiety directly interfaces with GPAT4.
(**A**) Schematic depicting steps to crosslink CHP1 and GPAT4 through a bifunctional fatty acyl group on the myristoylation site of CHP1. (**B**) Immunoblot and in-gel fluorescence analysis of bifunctional fatty acid incorporation. HeLa CHP1_KO cells expressing the indicated FLAG-CHP1 constructs were incubated with 500 μM of the indicated bifunctional fatty acids or control palmitate for 24 hrs prior to immunoprecipitation. Fluorescence indicates incorporation of fatty acids through click chemistry with azido-rhodamine. (**C**) Immunoblot using an antibody against CHP1 on immunoprecipitates with FLAG-CHP1 or FLAG-CHP1-myr_mut in the presence or absence of x-alk-16 photo-crosslinking. Crosslinked complex of CHP1-GPAT4 appeared as a higher band with a combined molecular weight of these two proteins (~80 kDa). (**D**) Immunoblot using antibody against GPAT4 on immunoprecipitates with FLAG-CHP1 or FLAG-CHP1-myr_mut in the presence or absence of x-alk-16 photo-crosslinking. Crosslinked complex of CHP1-GPAT4 appeared as a higher band with a combined molecular weight of these two proteins (~80 kDa). (**E**) Schematic depicting active and inactive forms of GPAT4. Interaction of CHP1 with GPAT4 alone is necessary but not sufficient for GPAT4 activity. Full GPAT4 activity requires CHP1 to be myristoylated.

2.9 Loss of CHP1/GPAT4 rewires cells to rely on peroxisomal glycerolipid synthesis

Our results with CHP1 knockout cells suggest that mammalian cells can survive and proliferate without ER GPAT activity. As these enzymes are required for the synthesis of essential membrane lipids, our findings indicate a degree of metabolic plasticity that allows sufficient phospholipid synthesis for cell survival and proliferation in the absence of CHP1. To identify these alternative metabolic routes that enable cell proliferation, we sought to define genes that are synthetically lethal with CHP1 loss. We therefore transduced wild type and CHP1 knockout Jurkat cells with the metabolism focused sgRNA library and identified genes whose loss reduced cellular proliferation and viability only in CHP1 knockout cells, but not in wild type counterparts (**Figure 2.18A**). Remarkably, the top two scoring genes essential in CHP1 knockout cells both encode peroxisomal proteins: ATP binding cassette subfamily D member 3 (ABCD3), which catalyzes the import of acyl-CoAs into peroxisomes and glyceronephosphate O-acyltransferase (GNPAT), which catalyzes the acylation of dihydroxyacetonephosphate (DHAP), a precursor for peroxisomal ether lipids (Datta and Hajra, 1984) (**Figures 2.18B-C**). Interestingly, none of the mitochondrial GPATs scored, suggesting that ER GPATs may use different fatty acid pools or their products may have different metabolic fates. To confirm these results, we transduced Jurkat wild type cells or CHP1 knockout cells with two sgRNAs targeting GNPAT. As predicted by the screen, GNPAT loss reduced proliferation of CHP1 knockout cells, but not that of wild type cells (**Figure 2.18D**). Interestingly, at the time of collection, we found that the remaining CHP1 knockout cells infected with virus expressing GNPAT sgRNA had higher amounts of GNPAT than the infected wild type cells, which is consistent with a selection against GNPAT loss in CHP1 knockout state (**Figure 2.18D**). Collectively, these data demonstrate that GNPAT is essential for the optimal proliferation of cells lacking ER GPAT activity.

We next asked how GNPAT alters cellular membrane lipid composition upon CHP1 loss. GNPAT catalyzes the first step of the synthesis of ether lipids, a unique class of glycerolipids that have an ether bond at the sn-1 position of the glycerol backbone rather than an ester bond like most other glycerolipids (Braverman and Moser, 2012). Under normal conditions, peroxisomes are the main site of ether lipid synthesis but contribute only to a minor portion of total glycerolipid content (Hajra et al., 2000; Liu et al., 2005). Consistent with these observations, ether lipid content of phosphatidylcholine and phosphatidylethanolamine, the two most abundant membrane lipids, decreased in GNPAT knockout cells (**Figure 2.18E**). In contrast, CHP1 knockout cells accumulated 2-fold more ether lipids in their membranes compared to wild type cells, suggesting that GNPAT mediated acylation of DHAP is the major route for glycerolipid synthesis when CHP1 or ER GPAT activity is lost (**Figure 2.18E**). This indicates that when ER glycerolipid pathway is inhibited, peroxisomal GNPAT compensates for the reduced glycerolipid synthesis and provides sufficient precursors for membrane lipid synthesis to enable cell survival and proliferation (**Figure 2.19**).

Here, using multiple genetic screens, we systematically defined metabolic regulators of saturated fatty acid toxicity and glycerolipid synthesis in mammalian cells. Our data suggests that fatty acid toxicity arises due to excess incorporation into cellular glycerolipids and that blocking the initial steps of the glycerolipid synthesis pathway, particularly GPAT4, is sufficient to prevent this toxicity. A major finding of our work is the identification of CHP1, a poorly characterized metabolic protein, as a key regulator of the first committed step of glycerolipid synthesis. Given its relatively uncharacterized role in metabolism, we next attempted to characterize its physiological function *in vivo*.

Figure 2.18. Upon CHP1 loss, cells depend on peroxisomal GNPAT to proliferate.
(**A**) Schematic depicting the CRISPR based screens of wild type and CHP1_KO Jurkat cells using a metabolism focused sgRNA library. (**B**) Gene scores in wild type versus CHP1_KO Jurkat cells (top). Top 5 genes scoring as differentially required in the CHP1_KO cells. Genes linked to peroxisomes are indicated in red (bottom). (**C**) Guide scores (log_2 fold change) of individual sgRNAs targeting ABCD3 and GNPAT used in the isogenic screen in wild type (black) or CHP1_KO (gray) cells. (**D**) Immunoblot analysis of Jurkat wild type and CHP1_KO cells infected with control and GNPAT targeting sgRNAs. Lysates from the first and ninth day of culture were compared. β-actin was used as a loading control (top). Relative cell numbers of the indicated cell lines to vector controls (mean ± SD, n=3). *$p < 0.05$, ***$p < 0.001$ versus vector control (bottom). (**E**) Fraction of ether phosphatidylcholine (PC) and phosphatidylethanolamine (PE) species of wild type, GNPAT_KO and CHP1_KO Jurkat cells. Lipid species of the same group were summed (mean ± SD, n=3).

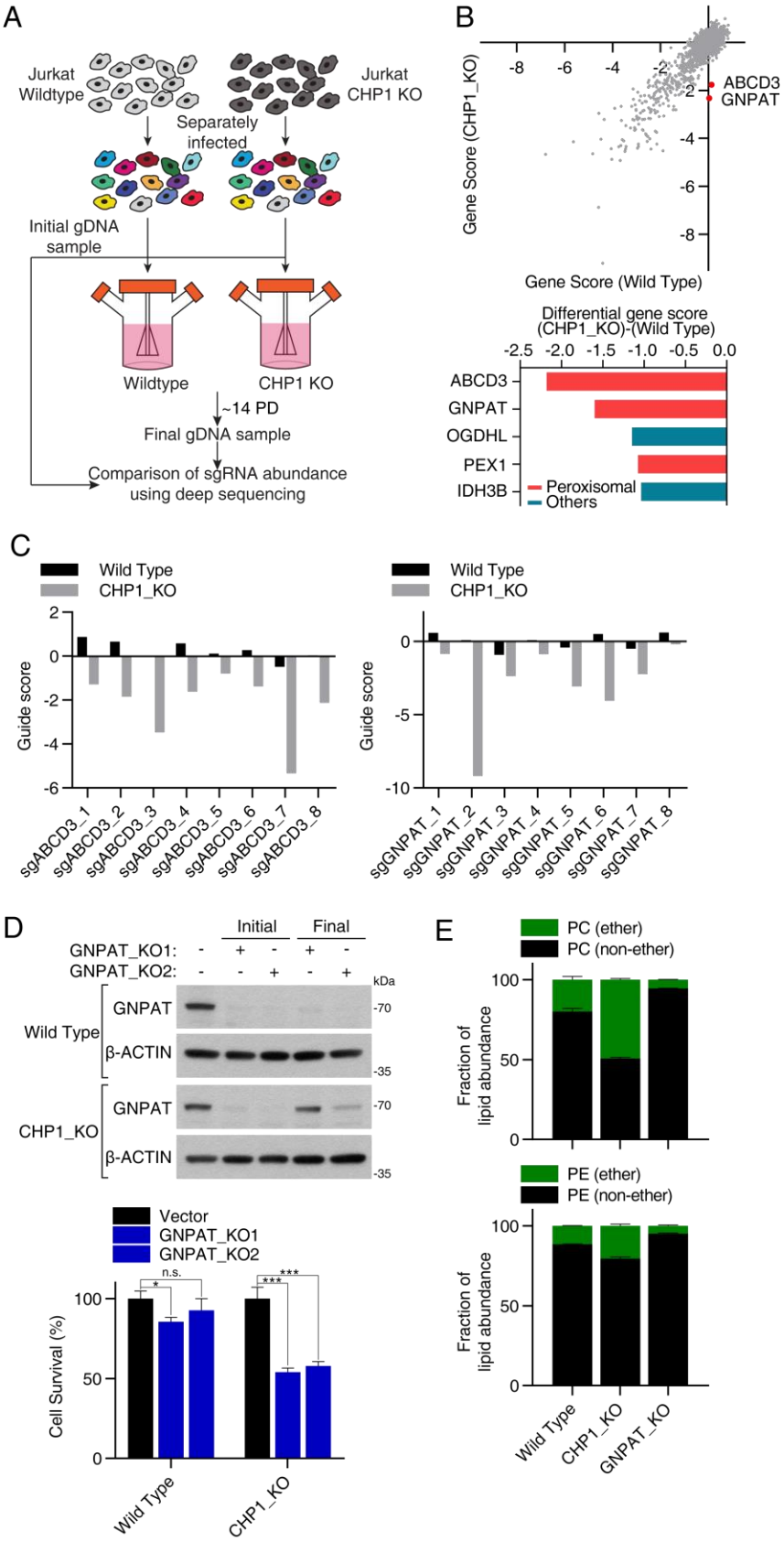
A
Jurkat Wildtype
Jurkat CHP1 KO
Separately infected
Initial gDNA sample
Wildtype
CHP1 KO
~14 PD
Final gDNA sample
Comparison of sgRNA abundance using deep sequencing
B
Gene Score (CHP1_KO)
Gene Score (Wild Type)
ABCD3
GNPAT
Differential gene score (CHP1_KO)-(Wild Type)
ABCD3
GNPAT
OGDHL
PEX1
IDH3B
Peroxisomal
Others
C
Wild Type
CHP1_KO
Guide score
sgABCD3_1
sgABCD3_2
sgABCD3_3
sgABCD3_4
sgABCD3_5
sgABCD3_6
sgABCD3_7
sgABCD3_8
sgGNPAT_1
sgGNPAT_2
sgGNPAT_3
sgGNPAT_4
sgGNPAT_5
sgGNPAT_6
sgGNPAT_7
sgGNPAT_8
D
Initial
Final
GNPAT_KO1:
GNPAT_KO2:
kDa
Wild Type
CHP1_KO
GNPAT
β-ACTIN
Vector
GNPAT_KO1
GNPAT_KO2
Cell Survival (%)
n.s.
E
PC (ether)
PC (non-ether)
PE (ether)
PE (non-ether)
Fraction of lipid abundance
Wild Type
CHP1_KO
GNPAT_KO

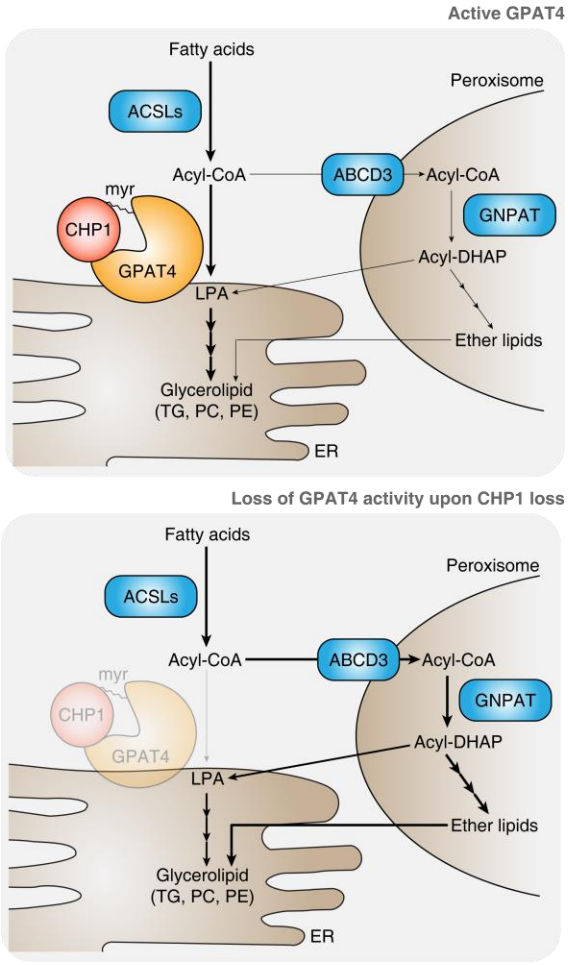

Figure 2.19. Loss of CHP1 rewires glycerolipid metabolism in proliferating cells.
Schematic depicting CHP1/GPAT4-catalyzed ER glycerolipid synthesis and the alternative peroxisomal pathway upon CHP1-GPAT4 loss. Under normal circumstances, CHP1 binds to and activates the major ER GPAT, (GPAT4), enabling the synthesis of membrane lipids and triacylglycerols at the endoplasmic reticulum. Upon CHP1 loss, peroxisomal GNPAT compensates for the loss of ER glycerolipid synthesis by generating acyl-DHAP, which in turn generates lysophosphatidic acid and glycerolipids.

CHAPTER 3. CHP1 enables glycerolipid synthesis and accumulation in tissues.

3.1 Lipid synthesis and storage in animal tissues

We have established through our series of genetic screens that CHP1 is essential for ER glycerolipid synthesis by activating GPAT4 in cells. Since the ER glycerolipid synthesis pathway is the major route of glycerolipid synthesis (Wendel et al., 2009), we wondered whether the loss of CHP1 will have a similar effect on animal tissues in the context of normal or diseased physiology. In mammals, the liver is the major site of glycerolipid synthesis while the adipose tissue is the major site of lipid storage (Nguyen et al., 2008). In lower animals without adipose tissue, lipids are stored in other tissues such as the intestine or specialized fat bodies. We first asked whether CHP1 is conserved in different animals and whether it has a similar role in glycerolipid synthesis in lower animals.

3.2 CHP1 is necessary for lipid synthesis invertebrate tissues

As orthologues of CHP1 proteins are conserved in vertebrates and invertebrates including *Drosophila melanogaster* and *Caenorhabditis elegans (***Figures 3.1A-B)**, we next asked whether CHP1 is also essential for lipid storage in lower metazoa. RNAi-mediated knockdown of CHP1 orthologue *pbo-1* suppressed lipid accumulation in the intestines of *C. elegans* as determined by Nile red staining (**Figures 3.1C-D**). To investigate the potential function of CHP1 in regulating *D. melanogaster* lipid storage, we ubiquitously knocked down CHP1 orthologue *elm* by using an *Actin5C Gal4* driver (**Figure 3.1E**). Reduction of *elm* expression also led to a decrease in lipid content of the two specialized fat storing organs: midgut (**Figure 3.1F-G**) and fat body (**Figure 3.1H**). Additionally, loss of CHP1 orthologues also led to accumulation of acylcarnitine in *C. elegans* and *D. melanogaster* (**Figures 3.1I-J**). Altogether, this indicates a conserved role for CHP1 in metazoan lipid storage.

3.3 Loss of CHP1 in mice is lethal

As CHP1 is intricately linked to the function of GPAT4 in mammalian cells, we wondered whether CHP1 will phenocopy GPAT4 in terms of genetics. Mice lacking *Gpat4* are viable and exhibit normal physiology. They show reduced body weight and are protected from diet and genetically induced obesity. Loss of *Gpat4* severely reduced triacylglycerol content in adipose tissue from various fat depots (Vergnes et al., 2006). We have already shown that loss of *Chp1* in mouse adipocytes led to a reduction of lipid droplets and triacylglycerol levels. Hence, we reasoned that mice with constitutive *Chp1* knockout will be similar to $Gpat4^{-/-}$ mice in terms of metabolic phenotypes. We thus decided to examine this possibility by creating a $Chp1^{-/-}$ mouse through CRISPR knockout. However, only heterozygous $Chp1^{+/-}$ mice were obtained and no homozygous $Chp1^{-/-}$ mice were born (**Figure 3.2**). As $Gpat4^{-/-}$ mice were viable, this suggests that loss of Chp1 may result in a loss of total ER GPAT activity that is critical in embryogenesis or Chp1 may be involved in additional processes unrelated to glycerolipid synthesis.

Figure 3.1. CHP1 is essential for glycerolipid synthesis and lipid storage in metazoa.
(**A**) Phylogenetic comparison of CHP1 orthologues and paralogues in metazoans. Protein sequences and comparisons were obtained from Ensembl (EMBL-EBI). CHP1 orthologues were highlighted in blue. Lowest peptide similarity in each group were shown. (**B**) Protein sequence comparison of human CHP1 to its closest orthologue or paralogue in mouse, fruit fly and nematode. (**C**) *C. elegans* were fed with bacteria containing a control or knockdown plasmid of the CHP1 paralogue *pbo-1*. Worms were fixed in isopropanol and stained with Nile red. Nile red fluorescence signals (red) were merged with brightfield micrographs (n=5). Scale bar, 200 µm. (**D**) Fold change (log_2) in the abundance of triacylglycerols of wild type and *pbo-1*_KD *C. elegans*. Values were normalized to the average of the wild type animals (mean ± SD, n=3). *$p < 0.05$ versus wild type. (**E**) Relative quantification of *elm* mRNA levels in the control and *elm*_KD flies. *Drosophila UAS-elm* RNAi or *UAS-White* RNAi transgenes were expressed under *Actin5C Gal4* driver. *White* RNAi served as control. Expression levels were normalized to *Rpl32* (mean ± SD, n=6). **$p < 0.01$ versus wild type. (**F**) Representative images of Nile red fluorescence (green) in the anterior midguts of indicated flies were shown (n=3). CHP1 orthologue *Drosophila elm* was knocked-down by *UAS-elm* RNAi under *Actin5C Gal4* driver. *White* RNAi served as control. Scale bar, 200 µm. (**G**) Fold change (log_2) in the abundance of triacylglycerols of control and *elm*_KD *D. melanogaster* midgut. Values were normalized to the average of the control animals (mean ± SD, n=3). ***$p < 0.001$ versus wild type. (**H**) Fat bodies from 5-days old adult flies were fixed and stained with Nile red. Representative images of Nile red fluorescence (green) in the indicated animals were shown. Scale bar, 50 µm. (**I**) Fold change (log_2) in the abundance of acylcarnitine of wild type and *pbo-1*_KD *C. elegans*. Values were normalized to the average of the wild type animals (mean ± SD, n=3). *$p < 0.05$ versus wild type. (**J**) Fold change (log_2) in the abundance of acylcarnitine of control and *elm*_KD *D. melanogaster* midgut. Values were normalized to the average of the control animals (mean ± SD, n=3). **$p < 0.01$ versus control.

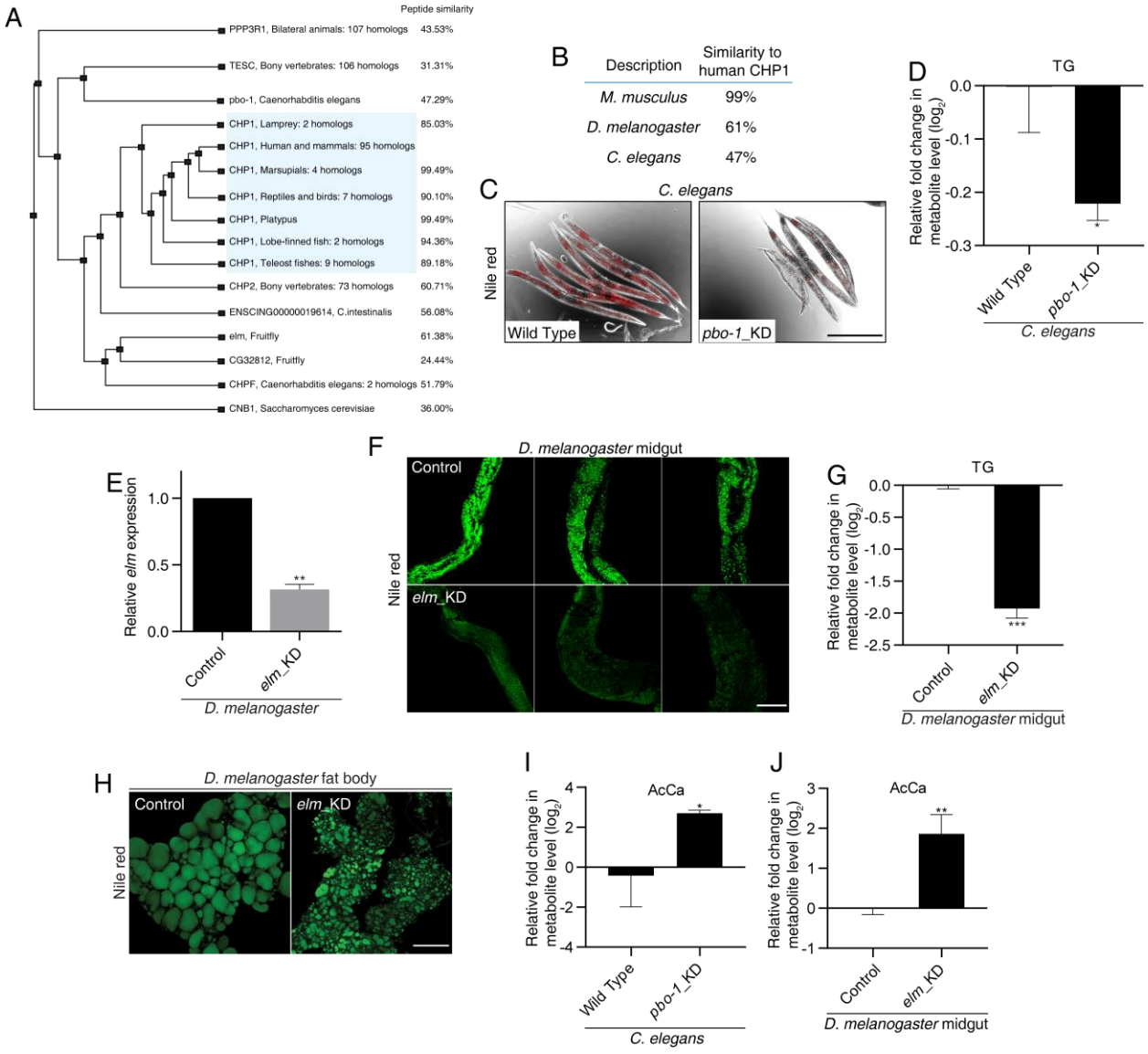
A
Peptide similarity
PPP3R1, Bilateral animals: 107 homologs 43.53%
TESC, Bony vertebrates: 106 homologs 31.31%
pbo-1, Caenorhabditis elegans 47.29%
CHP1, Lamprey: 2 homologs 85.03%
CHP1, Human and mammals: 95 homologs
CHP1, Marsupials: 4 homologs 99.49%
CHP1, Reptiles and birds: 7 homologs 90.10%
CHP1, Platypus 99.49%
CHP1, Lobe-finned fish: 2 homologs 94.36%
CHP1, Teleost fishes: 9 homologs 89.18%
CHP2, Bony vertebrates: 73 homologs 60.71%
ENSCING00000019614, C.intestinalis 56.08%
elm, Fruitfly 61.38%
CG32812, Fruitfly 24.44%
CHPF, Caenorhabditis elegans: 2 homologs 51.79%
CNB1, Saccharomyces cerevisiae 36.00%
B
Description
Similarity to human CHP1
M. musculus 99%
D. melanogaster 61%
C. elegans 47%
C
C. elegans
Nile red
Wild Type
pbo-1_KD
D
TG
Relative fold change in metabolite level (log2)
0.0
-0.1
-0.2
-0.3
*
Wild Type
pbo-1_KD
C. elegans
E
Relative elm expression
1.0
0.5
0.0
**
Control
elm_KD
D. melanogaster
F
D. melanogaster midgut
Control
elm_KD
Nile red
G
TG
Relative fold change in metabolite level (log2)
0.0
-0.5
-1.0
-1.5
-2.0
-2.5
***
Control
elm_KD
D. melanogaster midgut
H
D. melanogaster fat body
Control
elm_KD
Nile red
I
AcCa
Relative fold change in metabolite level (log2)
4
2
0
-2
-4
*
Wild Type
pbo-1_KD
C. elegans
J
AcCa
Relative fold change in metabolite level (log2)
3
2
1
0
-1
**
Control
elm_KD
D. melanogaster midgut

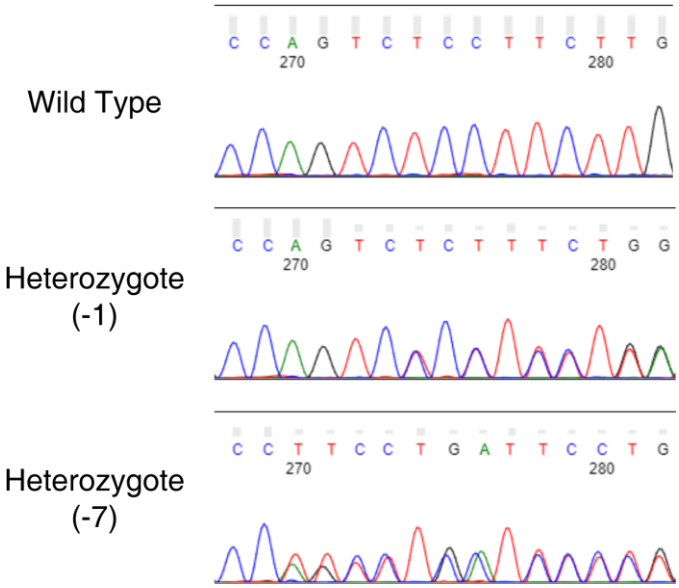

Figure 3.2. Genotypes of constitutive *Chp1* knockout mice.
Homozygous constitutive *Chp1*$^{-/-}$ mice were not viable and only heterozygotes were obtained. Sequencing traces of heterozygotes with -1 or -7 nucleotide deletions were shown compared to wild type animals at the site of sgRNA cleavage.

3.4 Liver-specific deletion of *Chp1* reduces liver steatosis and inflammation

We next decided to create an inducible *Chp1* knockout mouse model to specifically probe the physiological function of Chp1 in various mouse tissues. We added loxP sites to flank exon 2 of the *Chp1* gene to generate a *Chp1*$^{fl/fl}$ mouse model in which *Chp1* can be knocked out in specific tissues or at specific times by introducing Cre recombinase. As the genomic DNA region around *Chp1* exon 2 contained abundant repetitive elements, it was initially difficult to introduce the loxP sites and we could only obtain a single pup with a Chp1 T45I mutation. This substitution mutation lies in an EF hand domain that we have shown to be unnecessary for Chp1's function in lipid metabolism. As disruption to essential Chp1 function would likely result in embryonic lethality given our constitutive *Chp1* knockout mice phenotype, we continued to functionally characterize these inducible *Chp1* knockout animals.

Since the liver is the major site of triacylglycerol lipid synthesis (Nguyen et al., 2008) and *Gpat4*$^{-/-}$ mice display reduced triacylglycerol levels in the liver (Vergnes et al., 2006), we reasoned that knocking out *Chp1* in the liver will present a clear phenotype of reduced glycerolipid synthesis. We thus crossed *Chp1*$^{fl/fl}$ mice with Alb-Cre mice that specifically express Cre in the liver to obtain *Chp1*$^{fl/fl}$, Alb-Cre mice that have *Chp1* specifically deleted in liver tissue. These *Chp1* liver-KO mice did not show any differences in body weight or show any visible phenotypes when kept on standard chow diet (**Figure 3.3A**). When we compared Chp1 protein levels in liver and kidney tissues, we could see that Chp1 was depleted specifically in the liver tissue and not in the kidney. Chp1 levels in the *Chp1*$^{fl/fl}$ mice were also similar to wild type mice, suggesting that the mutation did not affect Chp1 protein expression. Interestingly, *Chp1* liver-KO mice also displayed lower levels of Gpat4 proteins in their livers (**Figure 3.3B**), corroborating our in vitro studies that loss of Chp1 leads to the decrease of Gpat4 protein levels (**Figure 2.12**). Given the efficient depletion of Chp1 in our *Chp1* liver-KO mice, we next asked whether their liver lipidomic profile will be

different from *Chp1*$^{fl/fl}$ or wild type mice. Surprisingly, *Chp1* liver-KO mouse livers do not show any apparent differences in the major lipid classes when compared to both *Chp1*$^{fl/fl}$ and wild type mice (**Figure 3.3C**). We also did not see any overt changes in the proteome of *Chp1* liver-KO mouse livers when compared to *Chp1*$^{fl/fl}$ mice (**Figure 3.3D**), arguing against the upregulation of compensatory lipid synthesis pathways. The lack of difference between *Chp1*$^{fl/fl}$ and wild type mice also suggests that the T45I mutation may not affect Chp1 function. Given these similarities, it is likely that the CHP1/GPAT4 axis contributes minimally to liver lipid content under normal physiology and we turned our attention to conditions where excess lipid is accumulated in the liver.

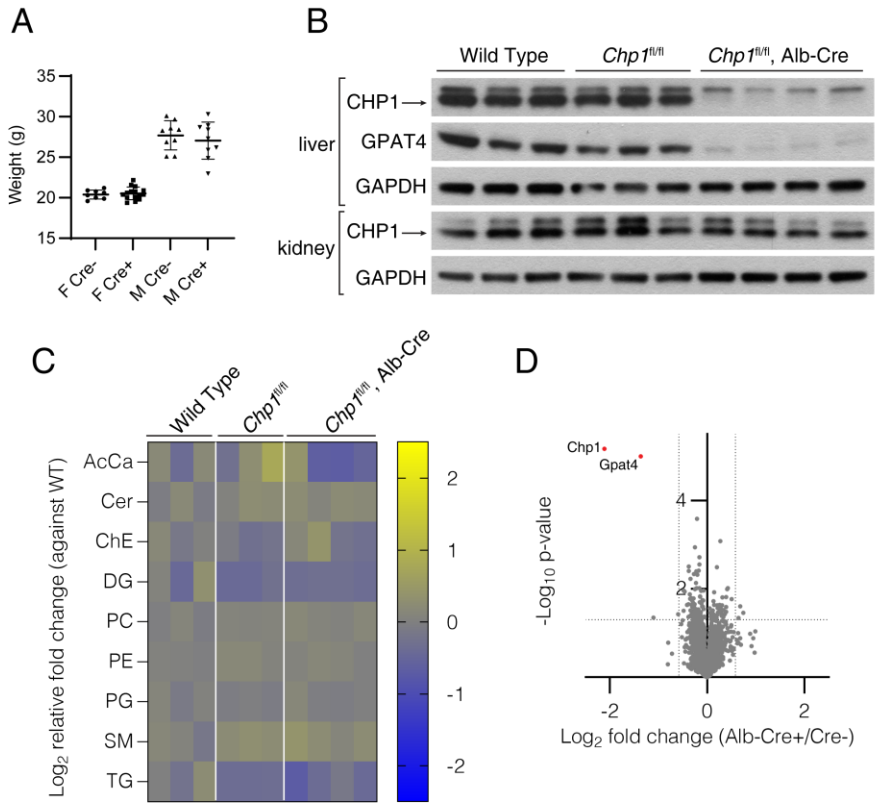

Figure 3.3. Chp1 deletion in mice liver does not cause overt metabolic or proteomic changes. **(A)** Body weights of *Chp1*$^{fl/fl}$ mice with or without Alb-Cre as indicated at 10 weeks of age (mean ± SD, n=8~15). F, female, M, male. (**B**) Immunoblot analysis of mouse livers from 8-week old animals of the indicated genotypes. GAPDH was used as a loading control. **(C)** Changes in lipid profiles of mouse livers from animals of the indicated genotypes. Lipid species of the same group were summed. Values were normalized to the average of the wild type controls (n=3~4). (**D**) Volcano plot of differential proteins comparing the mouse livers from animals of the indicated genotypes. Chp1 and Gpat4 are highlighted in red.

Nonalcoholic fatty liver disease (NAFLD) is a range of conditions where excess lipids are stored in the liver of the affected patients. The cause of NAFLD is unknown and some of the underlying conditions such as obesity and diabetes are difficult to manage. The excess lipid buildup may eventually lead to inflammation and fibrosis, a condition known as nonalcoholic steatohepatitis (NASH). As lipid buildup in the liver is the primary indication of NASH, we wondered if deleting Chp1 in the liver to modulate glycerolipid synthesis may alleviate the excess lipid deposition and

resulting inflammation. As a model for NASH, we kept female *Chp1* liver-KO mice and their *Chp1*$^{fl/fl}$ control animals on a high fat, high sugar NASH diet for 15 weeks. The mice showed similar weight gains overall without any difference between *Chp1* liver-KO and control animals (**Figure 3.4A**). At the end of the experiment, we sacrificed the animals and measured their liver and adipose tissue weights. Relative to whole body weight, the relative liver weights of *Chp1* liver-KO animals were significantly lower than control animals while their relative adipose tissue weights were similar (**Figure 3.4B**). This indicates that Chp1 deletion in the liver indeed prevented excess lipid deposition in the liver tissue. Lipidomic profiling of the livers revealed that there was a reduction in liver triacylglycerol content and increases in acylcarnitine and cholesteryl ester levels (**Figure 3.4C**), similar to what we observed *in vitro* (**Figure 2.9**). Comparison between the lipidomic changes in mouse livers under NASH diet and cultured cells treated with excess palmitate also revealed that most lipid classes were altered in a similar way (**Figure 3.4D**). Apart from lipid deposition, *Chp1* liver-KO also displayed reduced inflammation and fibrosis in the liver when compared to control animals (**Figure 3.4E**). These results indicate that under excess lipid availability, Chp1 enables glycerolipid synthesis in the liver and loss of which prevents steatosis and fibrosis during NASH.

Overall, we have established CHP1 as a key regulator of glycerolipid synthesis both *in vitro* and *in vivo*. Loss of CHP1 prevents excess lipid synthesis and accumulation through the downregulation and inactivation of GPAT4. Our results suggest that targeting CHP1 may be a viable option to prevent excess lipid deposition and inflammation in patients with NASH. We have also shown that saturated fatty acid toxicity can be a metabolic liability of cancer cells when saturated fatty acids are in excess. Leading from this, we wondered whether we can systematically characterize the metabolic liabilities of cancer cells in their natural microenvironment and whether genes related to lipid synthesis and saturation that we have characterized will be essential for tumor progression.

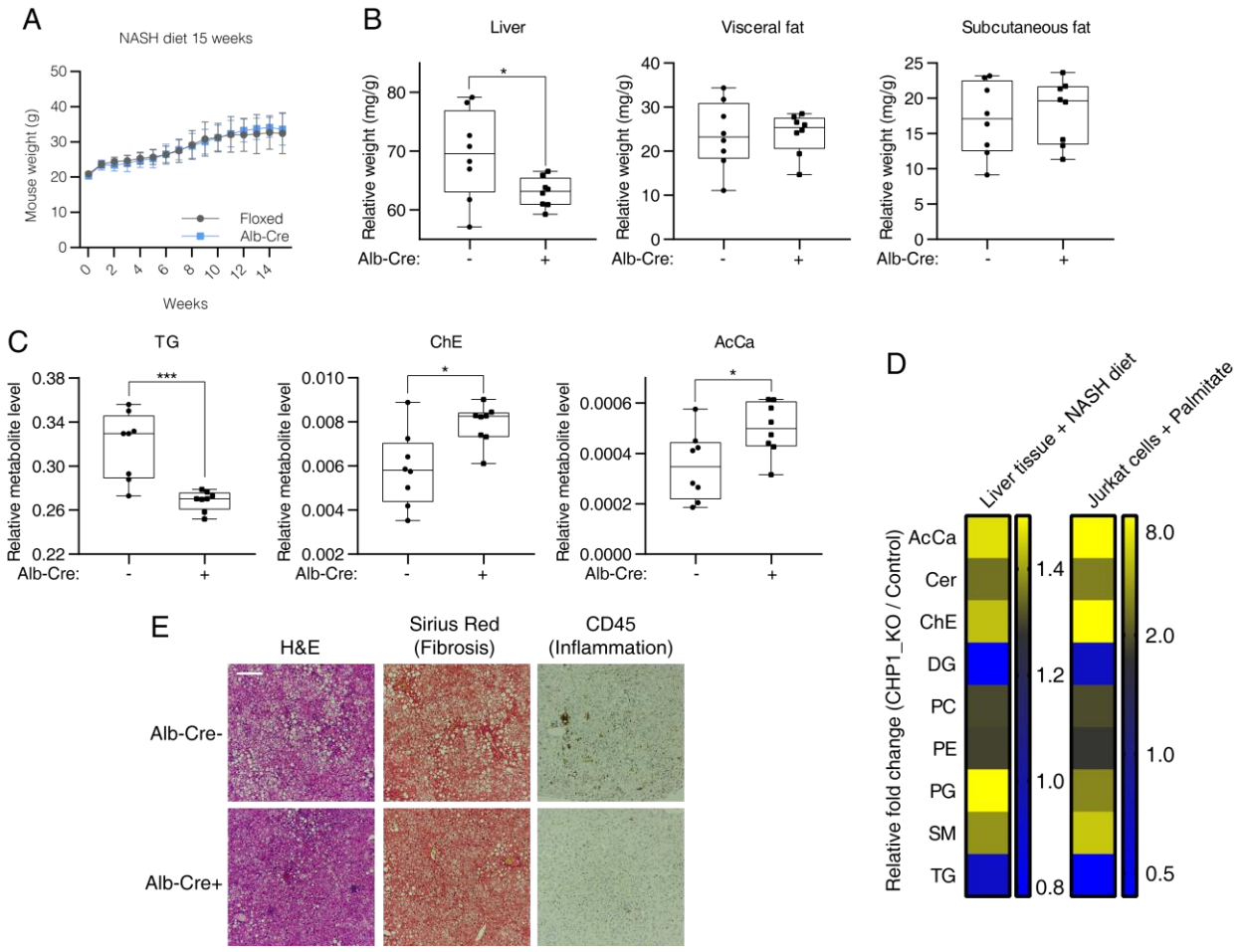

Figure 3.4. Deletion of Chp1 in the liver prevents excess lipid deposition and inflammation during NASH.

(**A**) Body weights of female *Chp1* liver-KO mice and *Chp1*$^{fl/fl}$ control mice kept on NASH diet for 15 weeks (mean ± SD, n=8). (**B**) Relative weights of the indicated tissues to body weights of *Chp1* liver-KO mice and *Chp1*$^{fl/fl}$ control mice. Mice were sacrificed after 15 weeks of NASH diet (mean ± SD, n=8). *p < 0.05 versus floxed control. (**C**) Relative abundance of individual lipid species of liver tissues from *Chp1* liver-KO mice and *Chp1*$^{fl/fl}$ control mice (mean ± SD, n=3). *p < 0.05, ***p < 0.001 versus floxed control. (**D**) Changes in lipid profiles of mouse livers from animals of the indicated genotypes and Jurkat cell data from **Figure 2.9**. Lipid species of the same group were summed. Values were normalized to the average of the controls (n=3~8). (**E**) H&E, Sirius Red and immunohistochemical staining of CD45 cells in paraffin embedded liver tissue slices from *Chp1* liver-KO mice and *Chp1*$^{fl/fl}$ control mice. Representative images are shown. Scale bar, 230 μm.

CHAPTER 4. Metabolic determinants of pancreatic tumor growth.

4.1 Challenges to identifying metabolic limitations of tumors *in vivo*

Recent isotope labeling studies argue that the metabolism of human tumors is different from that of cancer cells in culture (Faubert et al., 2017; Hui et al., 2017). The tumor microenvironment in part drives this difference as cancer cells frequently starve for nutrients and oxygen due to dysfunctional vasculature. Indeed, changes in environmental nutrients and oxygen in culture can cause widespread effects on cancer cell metabolism (Alvarez et al., 2017; Birsoy et al., 2014; Cantor et al., 2017; Vande Voorde et al., 2019). Additionally, solid tumors are extraordinarily complex, containing diverse cell types including vascular cells, fibroblasts and immune cells. Many non-cancerous cell types are in constant interaction with each other and provide metabolic support for growth and evasion of immune surveillance (Kishton et al., 2017). These observations raise the possibility that much of the work done in culture conditions may not reflect the cellular and nutrient complexities of human tumors. Despite recent attempts to recapitulate cancer metabolic states *in vivo* (Sullivan et al., 2019), nutrient composition of most human tumor types remains to be defined and the metabolic pathways that cancer cells require to proliferate in the context of the stromal and immune cells remain poorly understood. Though CRISPR and siRNA genetic screens have been widely used to identify metabolic dependencies of cancer cells, most of these screens were conducted *in vitro*. Technical limitations have also restricted the success of genetic screens *in vivo* as it has been difficult to conduct negative selection screens with good coverage and efficiency in animals. We have optimized our CRISPR screening protocol to obtain effectively complete coverage of our library within tumors and have thus attempted to unbiasedly delineate the differential metabolic limitations of cancer cells grown in culture and as tumors.

4.2 Pancreatic cancer cells rewire their metabolism

We have decided to apply our *in vivo* CRISPR screening strategy to pancreatic cancer given its propensity to rewire its metabolism in tumors. Pancreatic ductal adenocarcinoma (PDAC) is an aggressive disease characterized by a dense desmoplastic stroma, severe hypoxia and an immunosuppressive microenvironment (Ryan et al., 2014). Mutations in *KRAS* and *TP53* are frequent in PDACs and contribute to metabolic changes that support anabolic processes as well as nutrient scavenging (Perera and Bardeesy, 2015). Previous work have identified metabolic pathways involved in PDAC progression such as autophagy, cysteine uptake and alanine metabolism (Badgley et al., 2020; Sousa et al., 2016; Yang et al., 2018). However, we currently lack a complete understanding of essential metabolic pathways during pancreatic tumor progression or how environmental factors cause each of these dependencies. Such a study would identify potential therapeutic targets for these cancers with limited treatment options.

4.3 Metabolism-focused CRISPR screens *in vivo* reveal essential genes for pancreatic tumor growth

Pancreatic tumors rely on various cellular metabolic pathways to grow, but how nutrient environments modify these dependencies is not well understood. To begin to address potential differences in metabolic pathway dependencies of pancreatic cancer cells grown in tissue culture or as tumors, we constructed a metabolism focused mouse sgRNA library targeting a

comprehensive set of ~2900 metabolic genes and performed parallel loss-of-function screens in a murine pancreas cancer cell line derived from a *Kras*^{G12D}/*Trp53*^{R172H} mutant (KP) PDAC mouse model (**Figure 4.1A**). This library contains sgRNAs targeting enzymes and small molecule transporters as previously reported (Birsoy et al., 2015), but also transcription factors and other regulators relevant to cellular metabolism. After transduction with the sgRNA library, we passaged the pool of knockout cells for 14 population doublings in culture but also formed subcutaneous tumors in an immunocompetent C57BL/6J mouse model. At the end of the screens, for each gene, we calculated its score as the median $\log_2$ fold change in the abundance of all sgRNAs targeting the gene. Despite the challenge of maintaining sgRNA representation *in vivo*, we were able to detect an overwhelming majority (> 99%) of sgRNAs from tumors, owing to the efficient engraftment of this syngeneic model. Furthermore, indicating the robustness of the screening approach, cumulative sgRNA frequencies of cultured cancer cells showed only a slight enrichment in representation compared to those of tumors (**Figure 4.1B**). Gene sets related to metabolic processes such as glycolysis and glycosylation showed strong depletion (**Figure 4.1C**), consistent with the known essentiality of these pathways (Ohtsubo and Marth, 2006; Tsherniak et al., 2017; Xu et al., 2005). Notably, sgRNA abundances correlated remarkably well between tumors and cultured pancreatic cancer cells ($r=0.761$, $p<0.001$) (**Figure 4.1D**). These results suggest that, despite the nutritional and cellular differences between tumors and culture systems, a substantial fraction of metabolic essentialities of pancreatic cancer cells *in vivo* are similar and likely not determined by the tumor environment.

Our screens also identify a small fraction of metabolic genes that are differentially required during tumor formation (~200 genes, ~7% of all screened genes) (**Figure 4.1E**). iPAGE analysis (Goodarzi et al., 2009) to search for the pathways most informative about the observed gene essentiality differences reveals that *in vivo* metabolic dependencies were enriched with gene modules associated with heme metabolism, oxidative phosphorylation, nucleotide synthesis and antigen presentation (**Figures 4.1E-F**). Among these are several metabolic genes previously reported to be selectively essential in tumors. For example, glucose transporters (*Slc2a1*) and electron transport chain components are necessary to enable cancer cell proliferation only under low glucose conditions of the tumor environment (Birsoy et al., 2014). Notably, genes involved in purine and pyrimidine metabolism such as *Dhodh* and *Ppat* score as essential, in line with findings that oncogenic *Kras* supports pancreatic cancer through regulation of nucleotide synthesis and inhibition of nucleotide metabolism slows down tumor growth *in vivo* (Santana-Codina et al., 2018). Finally, PDACs display high basal autophagic flux (Yang et al., 2014, 2018, 2011), inhibition of which decreases tumorigenicity *in vivo*. Interestingly, consistent with the higher lipid content of the serum *in vivo* (Weiss et al., 1986), several lipid synthesis genes, such as ATP citrate lyase (*Acly*) and hydroxysteroid 17-beta dehydrogenase 12 (*Hsd17b12*), known to be essential for cancer cell growth in culture were dispensable for tumor growth (**Figures 4.1G-H)**. These results suggest that given the essentiality of lipid desaturation in certain hypoxic tumors (Ackerman et al., 2018), such a phenomenon is likely cell type and tissue specific as the availability of lipid species in the microenvironment can influence the extent of saturated lipid toxicity in tumors. Overall, while reflecting these recently reported vulnerabilities, our screens provide a robust compendium of metabolic dependencies of pancreatic cancer cells in culture and as tumors**.**

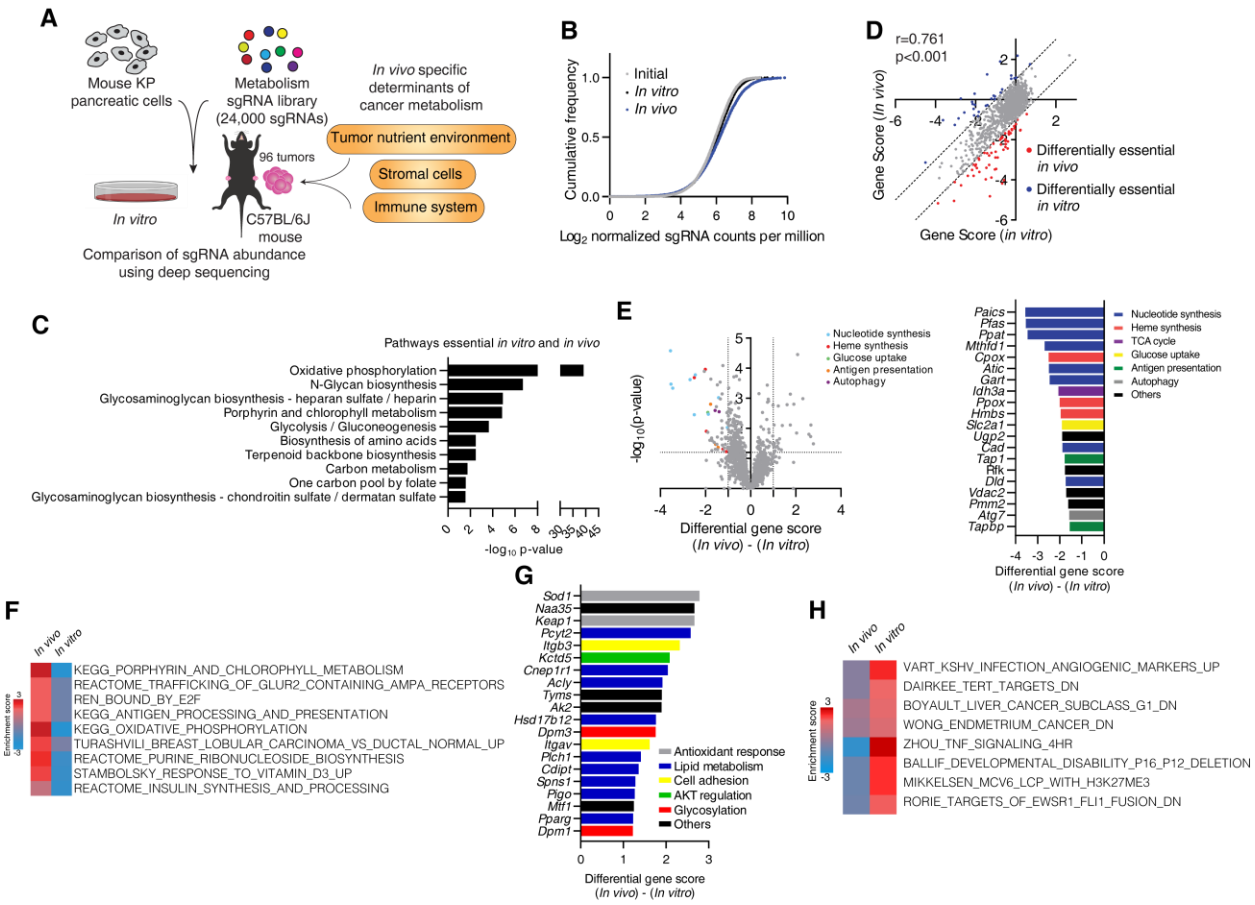

Figure 4.1. Metabolism-focused CRISPR screens *in vivo* reveal metabolic dependencies of pancreatic tumors.
(**A**) Schematic of genetics screens to identify metabolic dependencies of KP pancreatic cancer specifically *in vivo*. (**B**) Cumulative frequency curve of represented guides in genetic screens. (**C**) KEGG pathways essential for both *in vitro* and *in vivo* growth of KP pancreas cells. (**D**) Gene scores of *in vivo* versus *in vitro* genetic screens of KP pancreatic cancer growth. (**E**) Volcano plot of differential gene scores comparing in vivo against in vitro conditions (left). Top 20 genes scoring as differentially required *in vivo*. Gene involved in specific metabolic pathways are indicated (right). (**F**) Gene sets enriched in differentially required genes *in vivo* versus *in vitro* for pancreatic cancer growth. The heatmap generated by iPAGE represents the extent to which each gene set is enriched among the genes that are essential for tumor growth *in vivo*. (**G**) Top 20 genes scoring as differentially required *in vitro*. Gene involved in specific metabolic pathways are indicated. (**H**) Gene sets enriched in differentially required genes *in vitro* versus *in vivo* for pancreatic cancer growth.

4.4 Tissue of origin partly dictates metabolic determinants of *Kras*-driven tumors

While environment may impact metabolic phenotypes of tumors, metabolic differences may also result from cell-autonomous factors such as driver mutations or tissue of origin**.** To address this for tissue of origin, we asked what portion of the metabolic dependencies of *Kras*-driven pancreatic cancer cells are shared by murine lung cancer cell lines with similar mutational profile. We

therefore customized a highly focused sgRNA library encompassing only the top scoring guides in our initial screen (top 40 *in vivo* essential genes, top 10 *in vitro* essential genes with 10 sgRNAs per gene and 20 non-targeting control guides) (**Figure 4.2A**) and performed a similar screen in a *Kras*-driven lung cancer cell line. The use of a small, focused library enables the use of multiple tumor types and better representation of sgRNAs. Surprisingly, comparison of sgRNA abundance reveals that only few of the metabolic essentialities were similar between the *Kras*-driven pancreas and lung cancer cells, suggesting that tissue of origin is an important determinant for metabolic dependencies *in vivo* (**Figures 4.2B-C**). Specifically, most metabolic dependencies of *Kras*-driven pancreatic tumors such as purine synthesis and autophagy were not differentially essential in *Kras*-driven lung tumors (**Figure 4.2D**). These findings are also consistent with previous work where tissue context dictates the use of different metabolic routes in mutant *Kras*-driven cancers (Mayers et al., 2016). Interestingly, among these, sgRNAs for heme synthesis genes (*Uros, Cpox, Ppox and Hmbs*) were depleted in both lung and pancreas tumors, indicating a generalized environmental pressure imposing the heme dependency regardless of tissue of origin (**Figures 4.2B-D**). Given the uncharacterized role of heme metabolism in pancreas cancer and its high score, we next focused our attention on heme synthesis.

4.5 Heme synthesis is essential for Kras-driven cancer growth specifically *in vivo*

Our screens yielded heme synthesis as the only common metabolic essentiality *in vivo* for lung and pancreatic cancer growth, raising the possibility that a common environmental limitation may impose this dependency. Consistent with the screening results, while depletion of *Hmbs* showed only a modest effect on the proliferation of these cancer cell lines in culture (**Figures 4.3A-B**), *Hmbs* loss strongly reduced the sizes of the tumors *in vivo* (**Figure 4.3C**). As heme acts as a cofactor for several enzymes of the ETC (Fukuda et al., 2017; Lin et al., 2019), the slight defect in cell growth *in vitro* could be exacerbated when cells were seeded at a low confluency and could be rescued by the addition of hemin (oxidized heme), pyruvate or the expression of LbNOX, an NADH oxidase that increases NAD^+/NADH ratio (Titov et al., 2016) (**Figures 4.3D-G**).

We next asked why cancer cells require heme synthesis specifically in the tumor environment and which environmental factors *in vivo* may result in this dependency. Heme limitation in tumors may be a result of lower heme availability or an increase in heme degradation (Li and Stocker, 2009). In line with the latter possibility, we observed substantial upregulation of heme oxygenase-I (Hmox1), the rate-limiting enzyme in heme catabolism, in tumors and in hypoxia compared to cultured cancer cells in normoxia (**Figure 4.4A**). Heme catabolism and Hmox1 upregulation are highly associated with oxidative stress and hypoxia, conditions observed in the tumor microenvironment (Panchenko et al., 2000). While hypoxia-inducible factor (HIF) regulates many of the cancer cell responses under hypoxia, knocking out *Hif1a* or *Hif2a* did not prevent Hmox1 stabilization in this context (**Figure 4.4B**). Building upon these observations, we hypothesized that upregulation of Hmox1 proteins, though normally beneficial for tumors (**Figures 4.4C-E**), likely makes heme a limiting molecule for tumor growth due to increased heme degradation. To test this possibility, we knocked out *Hmox1* in murine pancreatic cancer cells deficient for *Hmbs* and asked whether heme becomes a limiting metabolite for growth. Supporting this idea, blocking heme degradation by knocking out *Hmox1* partially rescued growth inhibition of tumors expressing *Hmbs* sgRNAs (**Figures 4.4F-G**).

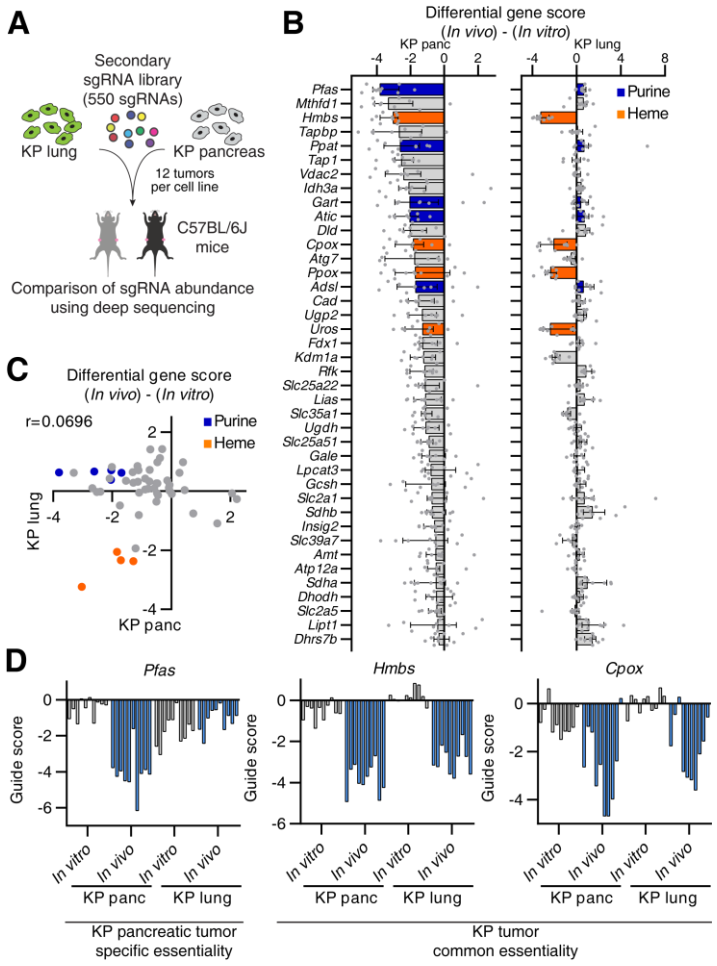

Figure 4.2. The tissue of origin partly dictates metabolic essentialities in *Kras*-driven cancers. (A) Schematic of focused genetic screens to identify common and different essential metabolic genes for KP pancreatic and KP lung tumor growth *in vivo*. (**B**) Top 40 genes scoring as differentially required *in vivo* in pancreatic tumors aligned to their differential gene scores in KP lung tumors. Genes involved in purine or heme synthesis are indicated. Bars are median differential gene scores with interquartile range. Dots are individual differential guide scores. (**C**) Gene scores of *in vivo* KP pancreas tumor growth versus KP lung tumor growth in C57BL/6J mice. Genes involved in purine or heme synthesis are indicated. (**D**) Guide scores of the indicated genes in the focused *in vivo* screens from KP pancreas and KP lung tumors.

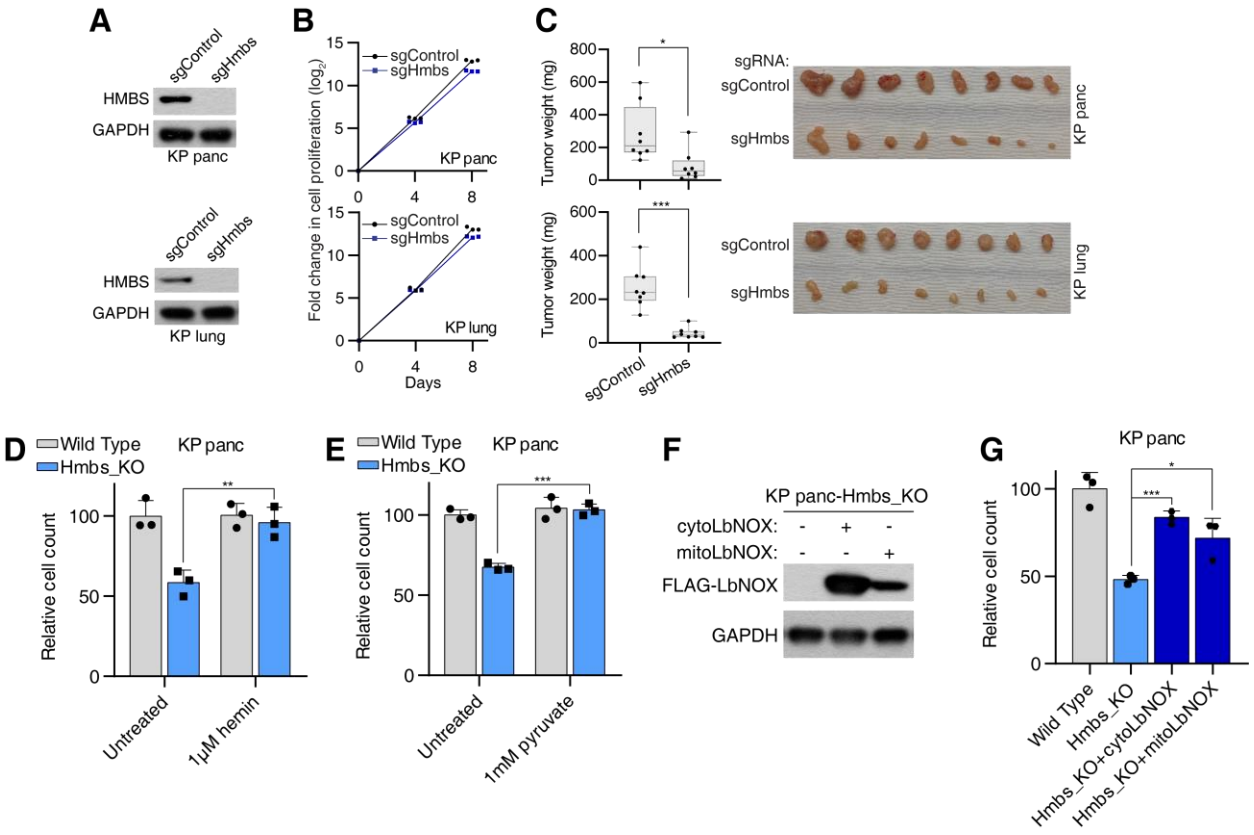

Figure 4.3. Heme synthesis is a metabolic dependency of *Kras*-driven tumors *in vivo*.
(**A**) Immunoblot of HMBS in the indicated KP pancreas and KP lung cancer cell lines. GAPDH was used as loading control. (**B**) Fold change in cell number (log_2) of the indicated KP pancreas and KP lung cancer cell lines after culturing *in vitro* for the indicated durations (mean ± SD, n=3). ***p < 0.001 versus sgControl. (**C**) Tumor weights of the indicated KP pancreas and KP lung tumors engrafted subcutaneously in C57BL/6J mice (box and whisker, n=8). *p < 0.05, ***p < 0.001 versus sgControl (left). Images of the indicated KP pancreas and KP lung tumors (right). (**D**) Relative cell count of indicated KP pancreas cell lines treated for 4 days with 1 μM hemin (mean ± SD, n=3). Counts were normalized to the average of the untreated wild type cells. **p < 0.01 versus untreated. (**E**) Relative cell count of indicated KP pancreas cell lines treated for 4 days with 1 mM pyruvate (mean ± SD, n=3). Counts were normalized to the average of the untreated wild type cells. ***p < 0.001 versus untreated. (**F**) Immunoblot of FLAG-LbNOX in the indicated KP pancreas Hmbs_KO cell lines. GAPDH was used as loading control. (**G**) Relative cell count of indicated KP pancreas cell lines grown for 4 days (mean ± SD, n=3). Counts were normalized to the average of the wild type cells. *p < 0.05, ***p < 0.001 versus Hmbs_KO.

To translate our findings to a more relevant *in vivo* model, we next asked whether targeting heme synthesis impacts the growth of patient-derived xenografts (PDXs). For this, we performed an *in vivo* loss-of-function competition assay using a pool of sgRNAs targeting control genomic regions or the *HMBS*, *CPOX* heme synthesis genes and *PPAT* purine synthesis gene as a positive control. Consistently, sgRNAs targeting the heme synthesis genes, but not those of controls, strongly inhibited the growth of tumors derived from the *KRAS* mutant pancreas PDXs (**Figure 4.4H**). Notably, using heme synthesis genes as a combined signature for scoring samples in the TCGA-PAAD dataset revealed a significant association between higher expression of heme synthesis

genes and lower disease-free survival compared to the group with lower expression (p=0.05) (**Figure 4.4I**). Taken together, our results identify heme synthesis as a metabolic liability imposed by the tumor microenvironment, independent of tissue of origin.

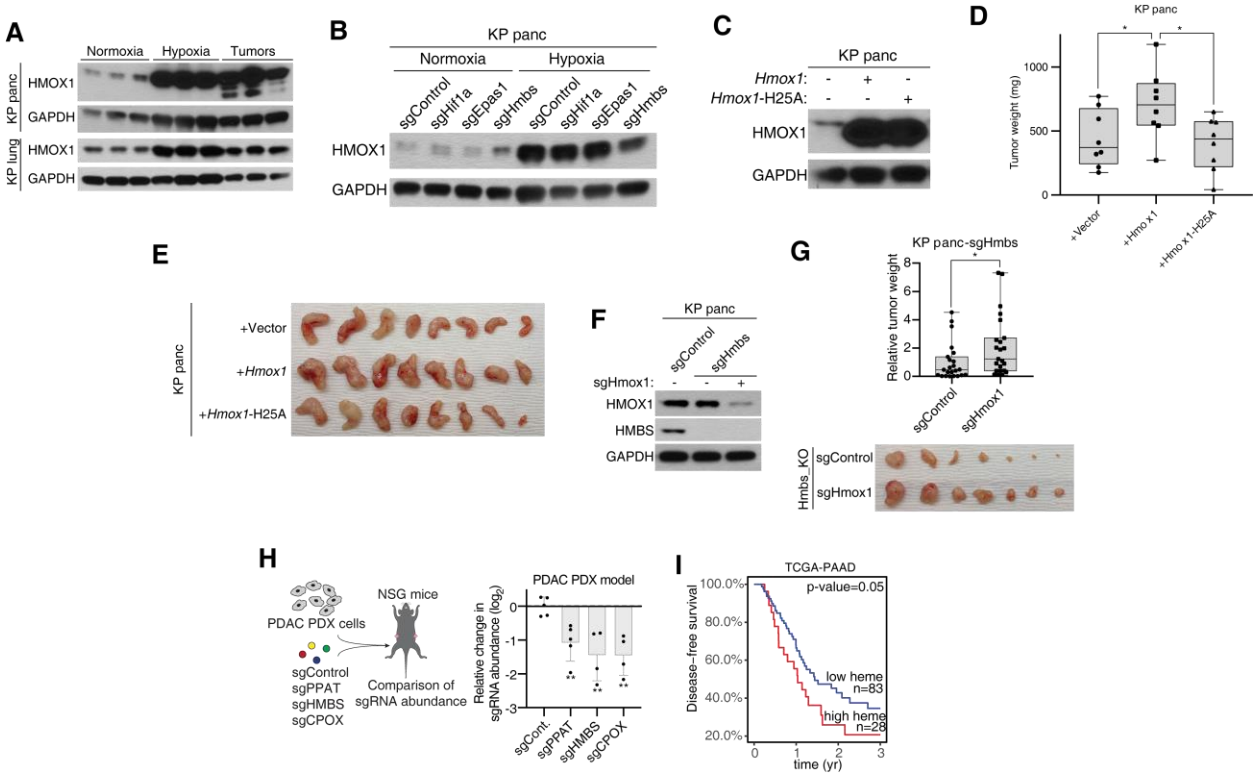

Figure 4.4. Hmox1 upregulation leads to heme synthesis dependency in *Kras*-driven tumors *in vivo*.

(**A**) Immunoblot of HMOX1 in KP pancreas and KP lung cancer cells grown *in vitro* under normoxia, hypoxia (0.5% oxygen) for 48 hrs and in subcutaneous tumors. GAPDH was used as loading control. (**B**) Immunoblot of HMOX1 in the indicated KP pancreas cell lines grown *in vitro* under normoxia or hypoxia (0.5% oxygen) for 48 hrs. GAPDH was used as loading control. (**C**) Immunoblot of Hmox1 in the indicated KP pancreas Hmbs_KO cell lines. GAPDH was used as loading control. (**D**) Tumor weights of the indicated KP pancreas tumors engrafted subcutaneously in C57BL/6J mice (box and whisker, n=8). *p < 0.05 versus Hmox1 overexpression. (**E**) Image of the indicated KP pancreas tumors. (**F**) Immunoblots of HMOX1 and HMBS in the indicated KP pancreas cell lines. GAPDH was used as loading control. (**G**) Relative tumor weights of the indicated KP pancreas Hmbs_KO tumors engrafted subcutaneously in C57BL/6J mice (box and whisker, n=23). *p < 0.05 versus Control (top). Representative image of the indicated KP pancreas Hmbs_KO tumors (bottom). (**H**) Schematic of competition assay using PDAC patient derived xenograft cells infected with the indicated sgRNAs. Cells were then engrafted subcutaneously in NSG mice (left). Relative fold change in sgRNA abundance (log2) from the PDX (mean ± SD, n=5). ***p < 0.001 versus sgControl (right). (**I**) Disease-free survival rates of TCGA PDAC patients with high or low heme synthesis gene expressions. Weighted average expressions of CPOX, HMBS, PPOX and UROS was used (low heme n=83, high heme n=28).

4.6 Identification of metabolic genes essential for pancreatic tumor immune evasion

We next asked whether any of the *in vivo* essential genes scored due to the presence of the immune system. As pancreatic tumors have immunosuppressive environments and are generally resistant to immunotherapy (Ryan et al., 2014), we hypothesized that a subset of the scoring metabolic genes may be involved in immune evasion and that their loss should enhance immune-mediated killing of cancer cells. To identify such genes, we repeated our genetic screens in immunodeficient NOD-SCID gamma (NSG) mice lacking mature T, B and natural killer (NK) cells and compared these hits to those obtained in immunocompetent mice (**Figure 4.5A**). Confirming the robustness of the screens, most genes scored similarly with a correlation of r=0.892 (**Figure 4.5B**).

Among the top genes differentially essential for tumor growth in immunocompetent mice were *Tap1* and *Tapbp*, genes required for the loading of antigen-derived peptides onto major histocompatibility complex (MHC) class I molecules for presentation (**Figures 4.5B-C**). In previously published work, loss of Tap proteins strongly blocks CD8+ T cell-mediated killing of cancer cells in co-culture assays *in vitro* (Kearney et al., 2018; Patel et al., 2017). However, our *in vivo* screens suggest that loss of key MHC class I-related genes has an opposite effect possibly because loss of MHC class I expression downstream of *Tap1* (**Figure 4.5D**) and *Tapbp* deletion can promote the killing of tumor cells by NK cells (Wu and Lanier, 2003). The only other hit from our screen was *Atg7*, a key enzyme involved in macroautophagy (**Figures 4.5B-C**). Of note, a similar autophagy gene, *Atg5*, also scored in our initial screen (**Figure 4.5E**), raising the possibility that autophagy may be a key process for immune evasion or immune-mediated cell death. Since cancer cell autophagy has hitherto not been associated with immune regulation, we decided to further explore the potential link between these two processes.

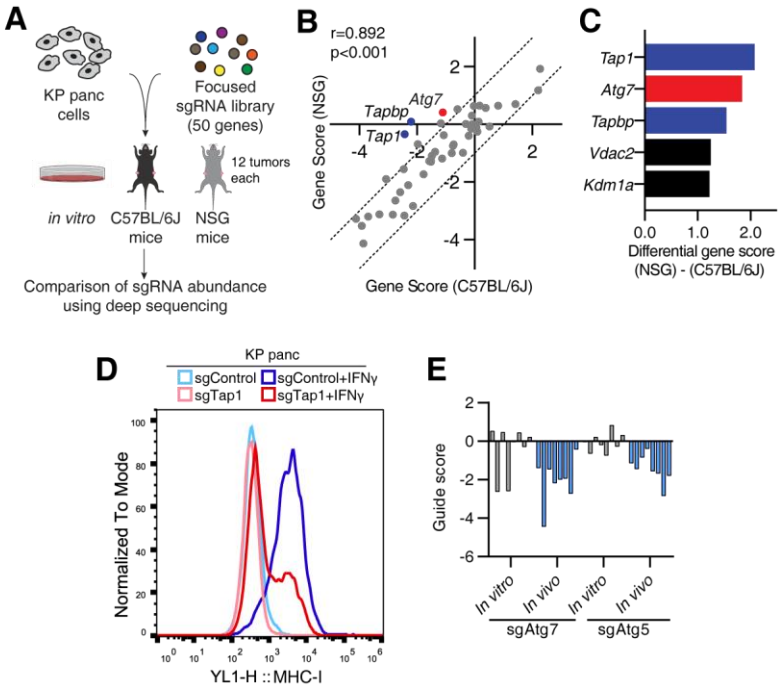

Figure 4.5. Autophagy is an immune-dependent metabolic liability and enables immune evasion in PDAC.

(**A**) Schematic of focused genetic screens to identify immune-dependent metabolic liabilities of KP pancreatic tumor growth *in vivo*. (**B**) Gene scores of *in vivo* KP pancreas tumor growth in immunodeficient NSG mice versus immunocompetent C57BL/6J mice. (**C**) Top 5 genes scoring as differentially required for KP pancreas tumor growth in immunocompetent mice compared to immunodeficient mice. Genes involved in TAP complex are indicated in blue. The autophagy gene *Atg7* is indicated in red. (**D**) Staining of MHC-I (H2-Kb) in the indicated KP pancreas cell lines treated for 24 hrs with 10 ng/mL IFNγ by flow cytometry. (**E**) Guide scores of *Atg* genes in the initial in vivo screen from **Figure 4.1**.

CHAPTER 5. Autophagy enables pancreatic tumor immune evasion.

5.1 Autophagy promotes pancreatic tumor development through cell autonomous and nonautonomous means

Pancreatic cancer cells display elevated autophagy, and inhibition of which suppresses tumor growth in xenografts (Guo et al., 2011; Perera et al., 2015) and genetically engineered mouse models (GEMM) (Yang et al., 2011, 2014, 2018). While several mechanisms have been proposed regarding how autophagy sustains pancreatic tumor growth (Amaravadi et al., 2016), the precise reason for the autophagy dependency of PDACs is not fully understood. Autophagy is well characterized as a process where unnecessary and damaged cell components are degraded. Biomolecules obtained through autophagy can then be recycled to provide nutrients during starvation or for cellular homeostasis. Autophagy has been shown to enable pancreatic tumor growth through both autonomous and nonautonomous mechanisms. Tumor autophagy has been shown to enable energy homeostasis in pancreatic cancer cells under various stresses (Kimmelman and White, 2017). On the other hand, inhibition of host autophagy in stromal and immune cells have also been shown to reduce pancreatic tumor growth by disrupting metabolic crosstalk and changing the tumor microenvironment (Yang et al., 2018; Poillet-Perez et al., 2020). Unlike these previous findings, our screen results suggest that tumor autophagy may help protect pancreatic cancer cells from immune-mediated growth suppression.

5.2 Tumor autophagy protects pancreatic cancer cells from immune cell-mediated cytotoxicity

Consistent with the previous findings, macroautophagy was dispensable for the growth of *Kras* mutant pancreatic cancer cells in culture (Eng et al., 2016) (**Figure 5.1A**). In contrast, *Atg7* deficient tumors in immunocompetent C57BL/6J mice were substantially smaller compared to those expressing sgRNA resistant *Atg7* cDNA (**Figures 5.1B-C**). Remarkably, this difference is dependent on the presence of lymphocytes, as the effect is completely abolished in NSG mice and mostly lost in Rag1-null mice, which lack mature T and B cells but not NK cells (**Figure 5.1C**). Similar to the mouse pancreatic cell line, *ATG7* loss in human *KRAS* mutant pancreatic tumors did not reduce tumor growth in NSG mice (**Figures 5.1D-E**). Immunohistochemical staining of tumor sections and immunoblotting showed increased caspase-3 cleavage in *Atg7* deficient tumors (**Figures 5.1F-G**), suggesting an immune-mediated increase in cell death. While we did not observe any increase in CD8+ T cell infiltration into *Atg7* deficient tumors (**Figure 5.2A**) or increases in the proportions of CD8+, CD4+ or NK cells within the infiltrating immune cells (**Figures 5.2B-D**), immune profiling showed an increase in IFNγ expression by both CD8+ T cells and NK cells (**Figures 5.2E-F**), in line with the small but significant decrease of tumor size in Rag1-null mice and the larger decrease in NSG mice. Notably, *ATG7* expression may be a predictive factor for patient outcomes, as pancreas cancer patients with low *ATG7* expression have significantly higher disease-free survival rates compared to patients with high *ATG7* expression (**Figure 5.2G**). A similar growth difference between *Atg7* deficient and proficient cells was observed in orthotopically injected tumors in the pancreas of C57BL/6J mice (**Figure 5.2H**). Finally, consistent with the increased IFNγ expression by CD8+ T cells, loss of *Atg7* sensitized pancreatic cancer cells expressing ovalbumin (OVA) antigen to OT-I T cell receptor-transgenic

CD8+ T cell-mediated killing in co-culture experiments (**Figures 5.2I-K**). Altogether, these results support a role for autophagy in PDAC immune evasion.

5.3 Autophagy protects cancer cells form TNFα-induced apoptosis

We next sought to understand how *Atg7* loss would enhance immune cell-mediated killing in pancreatic cancer cells. As presentation of neoantigens by MHC class I molecules enables detection of cancer cells by CD8+ T cells, autophagy inhibition may disrupt antigen presentation and promote immune evasion, as previously suggested (Loi et al., 2016; Yamamoto et al., 2020). However, we did not detect substantial differences in MHC-I protein levels or surface expression in either mouse or a subset of human pancreatic cancer cell lines when stimulated with IFNγ (**Figures 5.3A-H**). Autophagy inhibition has also been suggested to increase the expression of programmed death-ligand 1 (PD-L1) (Wang et al., 2019), but we did not observe any change in surface PD-L1 upon loss of autophagy (**Figure 5.3I**). To investigate alternative pathways that may lead to resistance to immune-mediated killing, we analyzed the transcriptome of *Atg7* deficient tumors and their isogenic counterparts complemented with *Atg7* cDNA using RNA-sequencing. Remarkably, iPAGE analysis revealed a strong enrichment for immune response pathways that are upregulated upon autophagy loss including gene sets that respond to TNFα or IFNγ, raising the possibility that *Atg7* loss may enhance the sensitivity of tumor cells to these cytokines (**Figures 5.4A-D**).

Building upon this observation, we asked whether autophagy protects cancer cells from cytokine-mediated cytotoxicity. Cell growth assays of pancreatic cancer cell lines with cytokines revealed that autophagy null PDAC cells are oversensitive to TNFα, but not to IFNγ (**Figures 5.5A-C**) and undergo Rip1-independent apoptosis upon TNFα treatment as assessed by immunoblotting of caspase-8 and caspase-3 cleavage (**Figures 5.5D-G**). While a change in the surface expression of the canonical receptor Tnfrsf1a may explain the protective effect of autophagy, we did not observe any differences in protein or surface expression levels of Tnfrsf1a in *Atg7* null cells (**Figures 5.6A-B**). Furthermore, CRISPR mediated knock out of the canonical receptor *Tnfrsf1a* completely abolished the sensitivity of autophagy deficient cells to TNFα (**Figure 5.6C**). Knock out of the alternate receptor *Tnfrsf1b* did not affect the sensitivity of autophagy deficient cells (**Figure 5.6D**), suggesting that autophagy may be specifically regulating the downstream response to Tnfrsf1a. This effect could also be recapitulated through pharmacological inhibition of autophagy with bafilomycin A1 or in autophagy deficient KP lung cancer cells and was independent of any secreted factors, supporting a generalized cell-autonomous link between autophagy and TNFα sensitivity (**Figures 5.6E-H**). Notably, consistent with both pro-apoptotic and pro-survival effects of TNFα signaling on tumors *in vivo* (Wang and Lin, 2008), expression of *Tnfrsf1a* sgRNAs in the pancreatic cancer cells severely reduced tumor growth regardless of autophagy proficiency (**Figure 5.6I**).

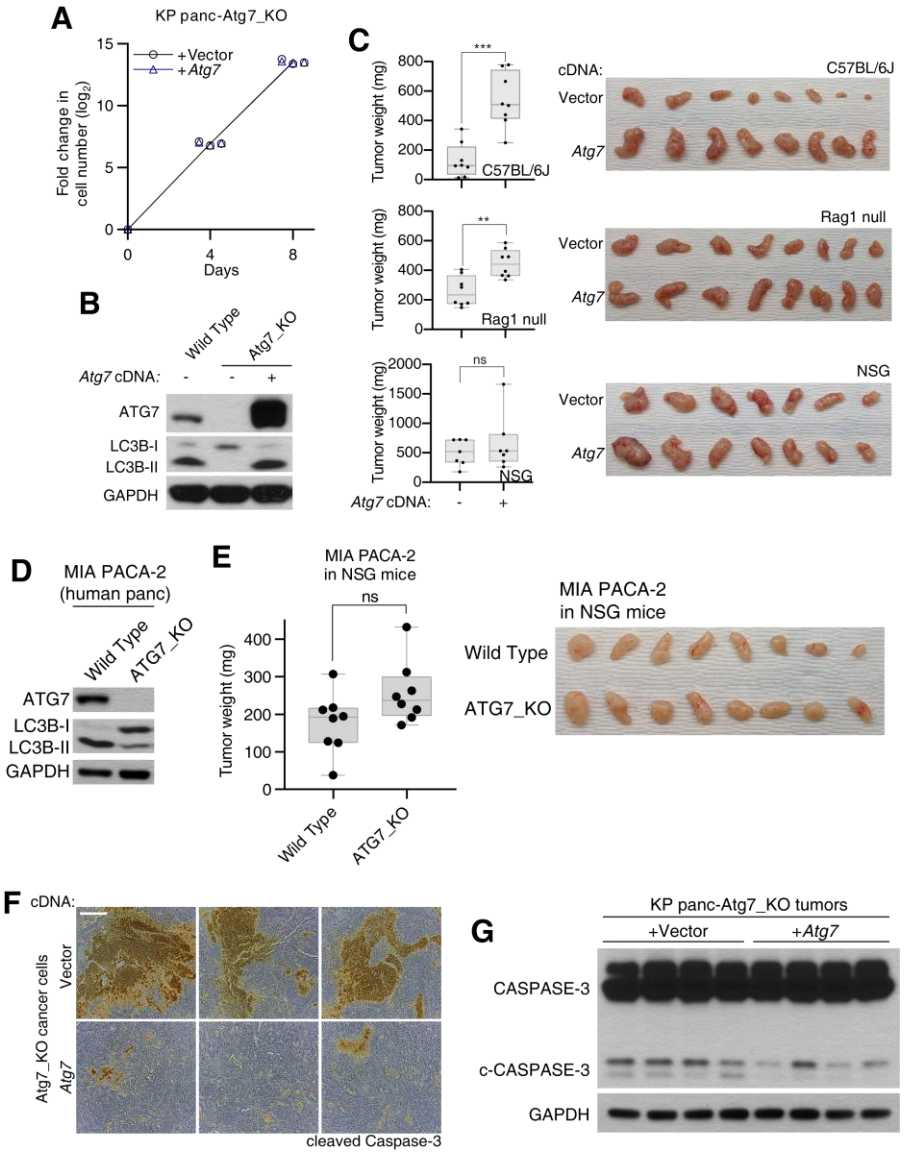

Figure 5.1. Autophagy enhances pancreatic tumor growth and prevents apoptosis in immunocompetent mice.

(**A**) Fold change in cell number (log_2) of the indicated KP pancreas Atg7_KO cell lines after culturing *in vitro* for the indicated durations (mean ± SD, n=3). (**B**) Immunoblots of ATG7 and LC3B in the indicated KP pancreas cell lines. GAPDH was used as loading control. (**C**) Tumor weights of the indicated KP pancreas Atg7_KO tumors engrafted subcutaneously in the indicated mice (box and whisker, n=8). **p < 0.01, ***p < 0.001 versus Atg7 addback (left). Image of the indicated KP pancreas Atg7_KO tumors from the indicated mice (right). (**D**) Immunoblot of ATG7 in the indicated human pancreas MIA PACA-2 cell lines. GAPDH was used as loading control. (**E**) Tumor weights of the indicated human pancreas MIA PACA-2 tumors engrafted subcutaneously in NSG mice (box and whisker, n=8). *p < 0.05 versus wild type (left). Image of the indicated human pancreas tumors (right). (**F**) Immunohistochemical staining of cleaved-CASPASE-3 in the indicated KP pancreas Atg7_KO tumors engrafted subcutaneously in C57BL/6J mice. Representative images are shown. Scale bar, 230 µm. (**G**) Immunoblot of CASPASE-3 in the indicated KP pancreas Atg7_KO tumors. GAPDH was used as loading control.

Figure 5.2. Loss of tumor autophagy suppresses immune cell activation and cytotoxic function.

(**A**) Immunohistochemical staining of Cd8a in the indicated KP pancreas Atg7_KO tumors engrafted subcutaneously in C57BL/6J mice. Representative images are shown. Scale bar, 200 μm. (**B**) Percentage CD8+ of CD45+ cells extracted from the indicated KP pancreas Atg7_KO tumors engrafted subcutaneously in C57BL/6J mice (mean ± SD, n=5). *p < 0.05 versus Atg7 addback. (**C**) Percentage NK1.1+ of CD3- CD8- cells extracted from the indicated KP pancreas Atg7_KO tumors engrafted subcutaneously in C57BL/6J mice (mean ± SD, n=5). *p < 0.05 versus Atg7 addback. (**D**) Percentage CD4+ of CD3+ CD8- cells extracted from the indicated KP pancreas Atg7_KO tumors engrafted subcutaneously in C57BL/6J mice (mean ± SD, n=5). (**E**) Percentage of IFNγ+ activated CD8+ T cells (left) or and NK cells (right) extracted from the indicated KP pancreas Atg7_KO tumors engrafted subcutaneously in C57BL/6J mice (mean ± SD, n=5). *p < 0.05, ***p < 0.001 versus Atg7 addback. (**F**) Percentage of IFNγ+ activated CD4+ T cells extracted from the indicated KP pancreas Atg7_KO tumors engrafted subcutaneously in C57BL/6J mice (mean ± SD, n=5). (**G**) Disease-free survival rates of TCGA PDAC patients with high or low ATG7 synthesis gene expressions. (low ATG7 n=35, high ATG7 n=76). (**H**) Tumor weights of the indicated KP pancreas Atg7_KO tumors engrafted orthotopically in the pancreas of C57BL/6J mice (box and whisker, n=12). **p < 0.01 versus Atg7 addback (left). Representative image of the orthotopic KP pancreas Atg7_KO tumors from the indicated mice (right). (**I**) Relative cell count of the indicated OVA-expressing KP pancreas Atg7_KO cell lines after co-culturing with activated OT-I CD8+ T cells for 48 hrs at the indicated E:T ratios (mean ± SD, n=3). Counts were normalized to the average of the monocultured cells of the same line. ***p < 0.001 versus Atg7 addback. (**J**) Percentage apoptotic (Annexin V+/DAPI+) KP pancreas Atg7_KO cell lines after co-culturing with activated OT-I CD8+ T cells for 48 hrs at the indicated E:T ratios (mean ± SD, n=3). ***p < 0.001 versus Atg7 addback. (**K**) Relative cell count of the indicated OVA- KP pancreas Atg7_KO cell lines after co-culturing with activated OT-I CD8+ T cells for 48 hrs at the indicated E:T ratios (mean ± SD, n=3). Counts were normalized to the average of the monocultured cells of the same line.

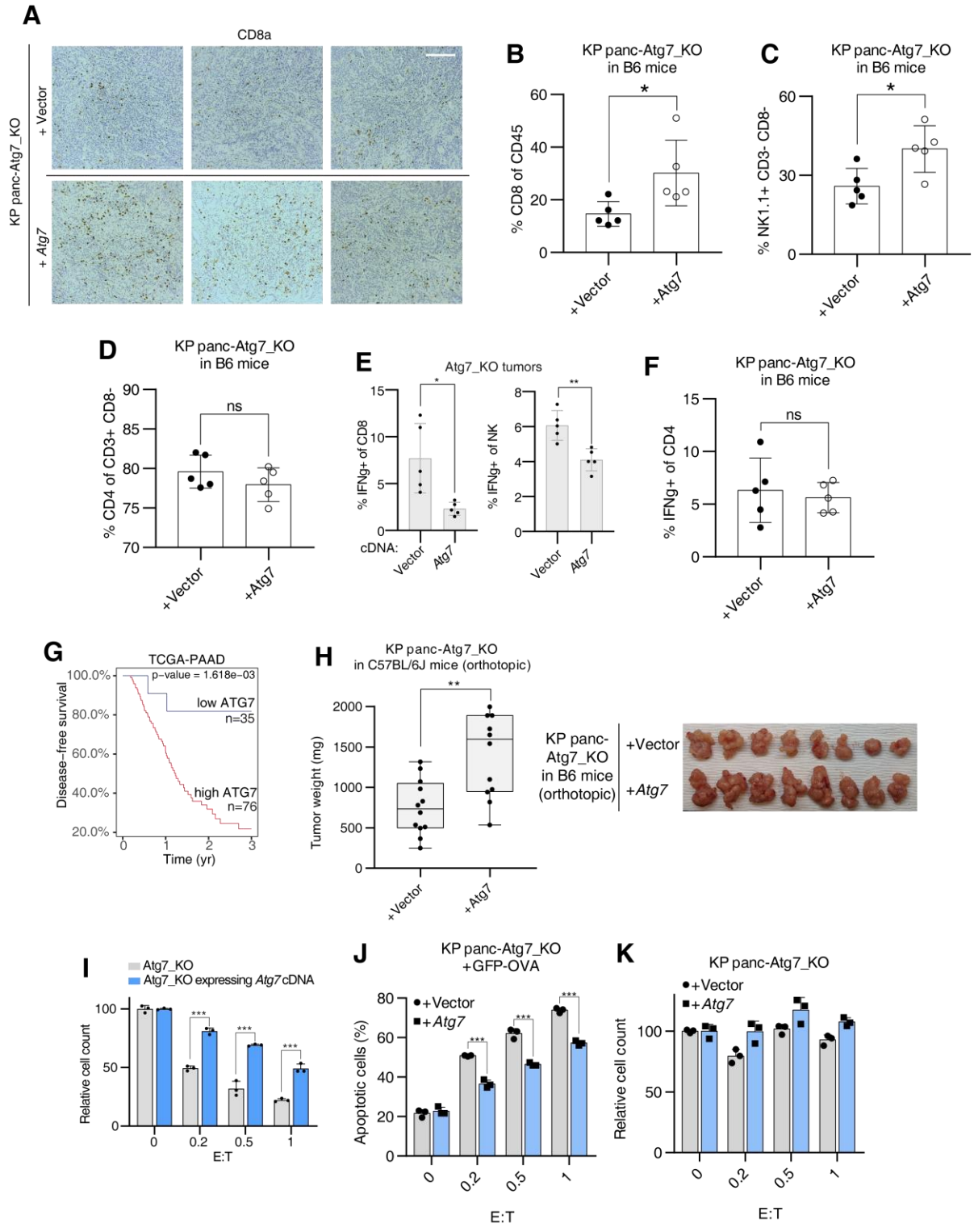
A
CD8a
KP panc-Atg7_KO
+ Vector
+ Atg7
B
KP panc-Atg7_KO
in B6 mice
% CD8 of CD45
+Vector
+Atg7
C
KP panc-Atg7_KO
in B6 mice
% NK1.1+ CD3- CD8-
D
KP panc-Atg7_KO
in B6 mice
% CD4 of CD3+ CD8-
ns
E
Atg7_KO tumors
% IFNg+ of CD8
% IFNg+ of NK
cDNA:
Vector
Atg7
F
KP panc-Atg7_KO
in B6 mice
% IFNg+ of CD4
G
TCGA-PAAD
p-value = 1.618e-03
low ATG7
n=35
high ATG7
n=76
Disease-free survival
Time (yr)
H
KP panc-Atg7_KO
in C57BL/6J mice (orthotopic)
Tumor weight (mg)
KP panc-
Atg7_KO
in B6 mice
(orthotopic)
+Vector
+Atg7
I
Atg7_KO
Atg7_KO expressing Atg7 cDNA
Relative cell count
E:T
J
KP panc-Atg7_KO
+GFP-OVA
+Vector
+Atg7
Apoptotic cells (%)
E:T
K
KP panc-Atg7_KO
+Vector
+Atg7
Relative cell count
E:T

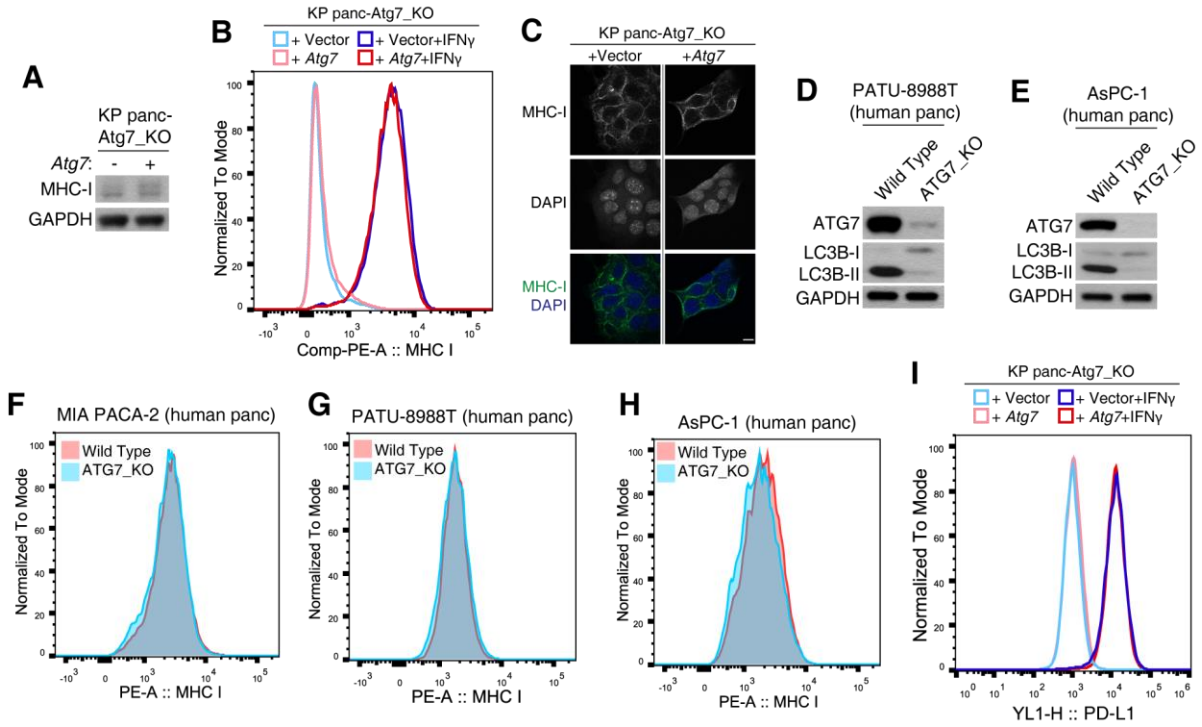

Figure 5.3. Loss of tumor autophagy does not affect surface MHC-I or PD-L1 levels of pancreatic cancer cells.

(**A**) Immunoblot of MHC-I (H2-Kb) in the indicated KP pancreas Atg7_KO cell lines. GAPDH was used as loading control. (**B**) Staining of MHC-I (H2-Kb) in the indicated KP pancreas Atg7_KO cell lines treated for 24 hrs with 10 ng/mL IFNγ by flow cytometry. (**C**) Immunofluorescence staining of MHC-I (H2-Kb) in the indicated KP pancreas Atg7_KO cell lines treated for 24 hrs with 70 ng/mL IFNγ. Scale bar, 10 μm. (**D**) Immunoblots of ATG7 and LC3B in the indicated human pancreas PATU-8988T cell lines. GAPDH was used as loading control. (**E**) Immunoblots of ATG7 and LC3B in the indicated human pancreas AsPC-1 cell lines. GAPDH was used as loading control. (**F**) Staining of MHC-I (HLA-A,B,C) in the indicated human pancreas MIA PACA-2 cell lines treated for 24 hrs with 1 ng/mL IFNγ by flow cytometry. (**G**) Staining of MHC-I (HLA-A,B,C) in the indicated human pancreas PATU-8988T cell lines treated for 24 hrs with 1 ng/mL IFNγ by flow cytometry. (**H**) Staining of MHC-I (HLA-A,B,C) in the indicated human pancreas AsPC-1 cell lines treated for 24 hrs with 1 ng/mL IFNγ by flow cytometry. (**I**) Staining of PD-L1 in the indicated KP pancreas Atg7_KO cell lines treated for 24 hrs with 10 ng/mL IFNγ by flow cytometry.

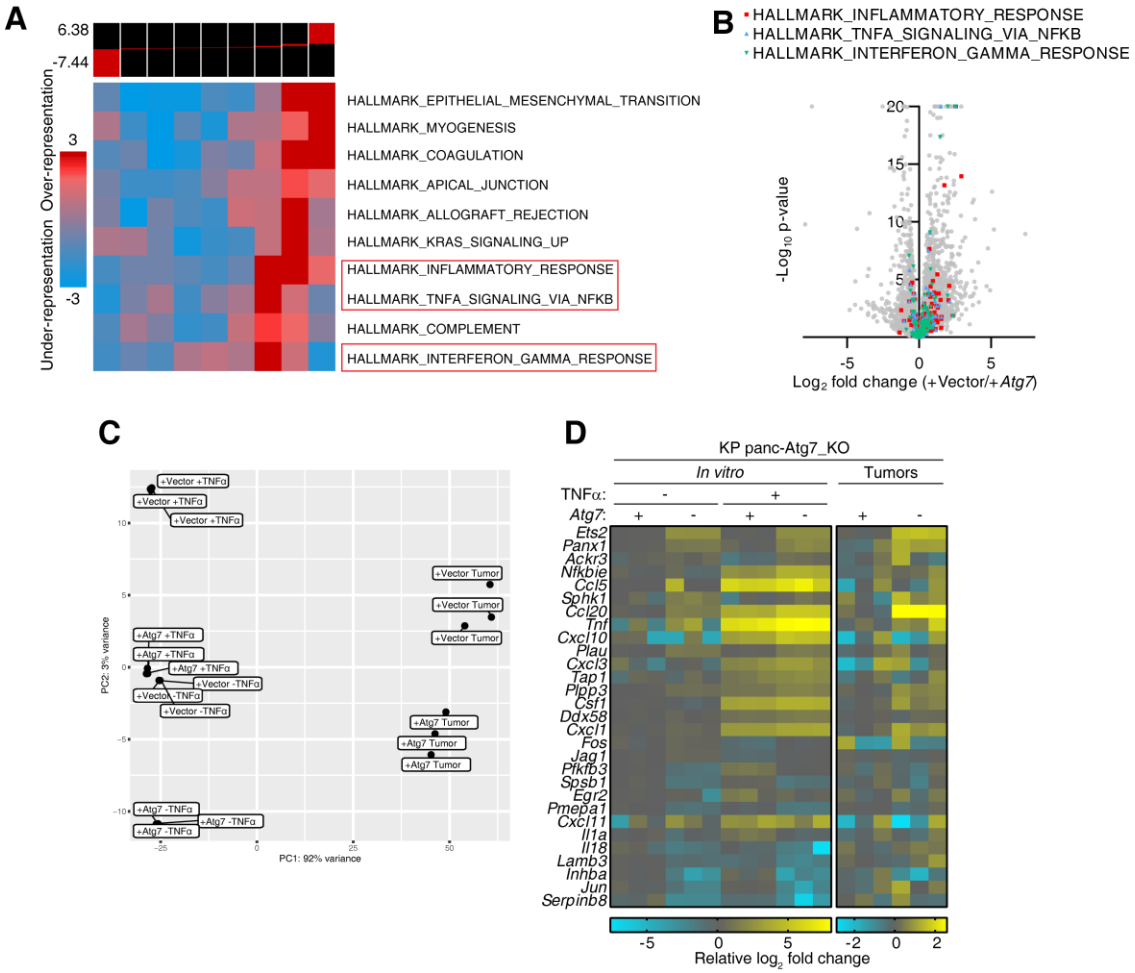

Figure 5.4. RNAseq analysis reveals enriched gene sets in autophagy deficient pancreatic cancers.

(**A**) RNAseq analysis of KP pancreas Atg7_KO tumors. Gene sets enriched in transcriptome of KP pancreas Atg7_KO tumors compared to Atg7 addback tumors engrafted subcutaneously in C57BL/6J mice (n=3). Immune-related gene sets are boxed in red. (**B**) Volcano plot of differential transcripts comparing the indicated KP pancreas Atg7_KO tumors. Gene in the indicated HALLMARK gene sets are highlighted. (**C**) Principal component analysis (PCA) of RNAseq results from the indicated KP pancreas Atg7_KO cell lines treated for 24hrs with 100 ng/mL TNFα (n=3) compared to KP pancreas Atg7_KO tumors. (**D**) RNAseq analysis of the indicated KP pancreas Atg7_KO cell lines treated for 24hrs with 100 ng/mL TNFα (n=3) compared to KP pancreas Atg7_KO tumors. Relative fold change (log_2) in mRNA levels of differentially regulated genes in HALLMARK_TNFA_SIGNALING_VIA_NFKB gene set were displayed. Fold changes were normalized to the average of Atg7 addback untreated cells or Atg7 addback tumors.

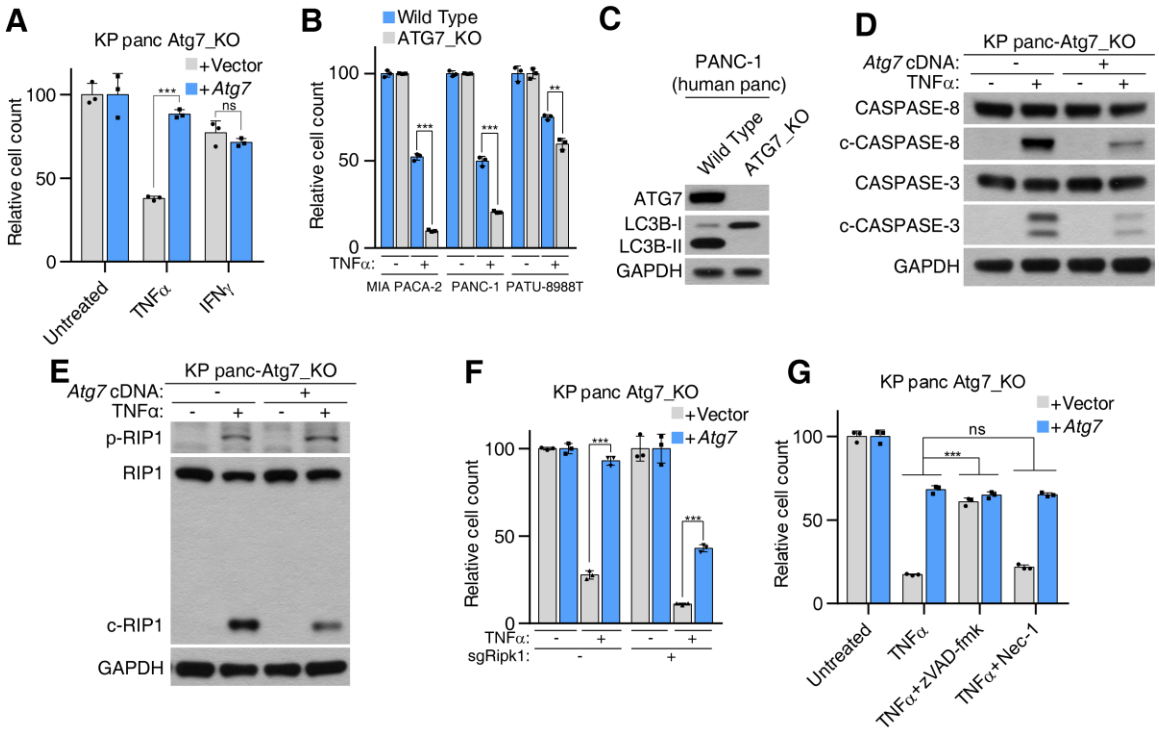

Figure 5.5. Loss of autophagy sensitizes pancreatic cancer cells to TNFα-induced apoptosis. (**A**) Relative cell count of indicated KP pancreas Atg7_KO cell lines treated for 48 hrs with 100 ng/mL TNFα or 100 ng/mL IFNγ (mean ± SD, n=3). Counts were normalized to the average of the untreated cells of the same line. ***p < 0.001 versus Atg7 addback. (**B**) Relative cell count of indicated human pancreatic cancer MIA PaCa-2, PANC-1 and PATU-8988T cell lines treated for 48 hrs with 100 ng/mL, 200 ng/mL and 600 ng/mL TNFα respectively (mean ± SD, n=3). Counts were normalized to the average of the untreated cells of the same line. **p < 0.01, ***p < 0.001 versus wild type. (**C**) Immunoblots of ATG7 and LC3B in the indicated human pancreas PANC-1 cell lines. GAPDH was used as loading control. (**D**) Immunoblot of CASPASE-8, cleaved CASPASE-8 and CASPASE-3 in the indicated KP pancreas Atg7_KO cell lines treated for 24 hrs with 100 ng/mL TNFα. GAPDH was used as loading control. (**E**) Immunoblot of phospho-RIP1, and RIP1 in the indicated KP pancreas Atg7_KO cell lines treated for 24 hrs with 100 ng/mL TNFα. GAPDH was used as loading control. (**F**) Relative cell count of indicated KP pancreas Atg7_KO cell lines treated for 48 hrs with 100 ng/mL TNFα (mean ± SD, n=3). Counts were normalized to the average of the untreated cells of the same line. ***p < 0.001 versus Atg7 addback. (**G**) Relative cell count of indicated KP pancreas Atg7_KO cell lines treated for 48 hrs with 100 ng/mL TNFα and 20μM zVAD-fmk or 10μM Necrostatin-1 (mean ± SD, n=3). Counts were normalized to the average of the untreated cells of the same line. ***p < 0.001.

Figure 5.6. Autophagy enables tumor immune evasion by increasing TNFα resistance.
(**A**) Immunoblot of TNFRSF1A in the indicated KP pancreas Atg7_KO cell lines. GAPDH was used as loading control. (**B**) Staining of TNFRSF1A in the indicated KP pancreas Atg7_KO cell lines by flow cytometry. (**C**) Relative cell count of indicated KP pancreas Atg7_KO cell lines treated for 48 hrs with 100 ng/mL TNFα (mean ± SD, n=3). Counts were normalized to the average of the untreated cells of the same line. ***p < 0.001. (**D**) Relative cell count of indicated KP pancreas Atg7_KO cell lines treated for 48 hrs with 100 ng/mL TNFα (mean ± SD, n=3). Counts were normalized to the average of the untreated cells of the same line. ***p < 0.001. (**E**) Relative cell count of KP pancreas cells treated for 48 hrs with 100 ng/mL TNFα or 50nM Bafilomycin A1 (BafA) (mean ± SD, n=3). Counts were normalized to the average of the untreated cells or those treated with BafA. ***p < 0.001. (**F**) Relative cell count of indicated KP pancreas Atg7_KO cell lines grown in 50% indicated conditioned media and treated for 48 hrs with 100 ng/mL TNFα (mean ± SD, n=3). Counts were normalized to the average of the untreated cells of the same line. ***p < 0.001 versus Atg7 addback. (**G**) Immunoblot of ATG7 in the indicated KP lung cell lines. GAPDH was used as loading control. (**H**) Relative cell count of indicated KP lung cell lines treated for 48 hrs with 200 ng/mL TNFα (mean ± SD, n=3). Counts were normalized to the average of the untreated cells of the same line. ***p < 0.001. (**I**) Tumor weights of the indicated KP pancreas Atg7_KO tumors engrafted subcutaneously in the indicated mice (box and whisker, n=8-12). **p < 0.01, ***p < 0.001 (left). Image of the indicated KP pancreas Atg7_KO tumors from the indicated mice (right). (**J**) Relative cell count of the indicated OVA-expressing KP pancreas Atg7_KO cell lines after co-culturing with activated OT-I CD8+ T cells for 48 hrs at the indicated E:T ratios with or without 40 μg/mL anti-TNFα (mean ± SD, n=3). Counts were normalized to the average of the untreated monocultured cells of the same line. ***p < 0.001 versus untreated cells.

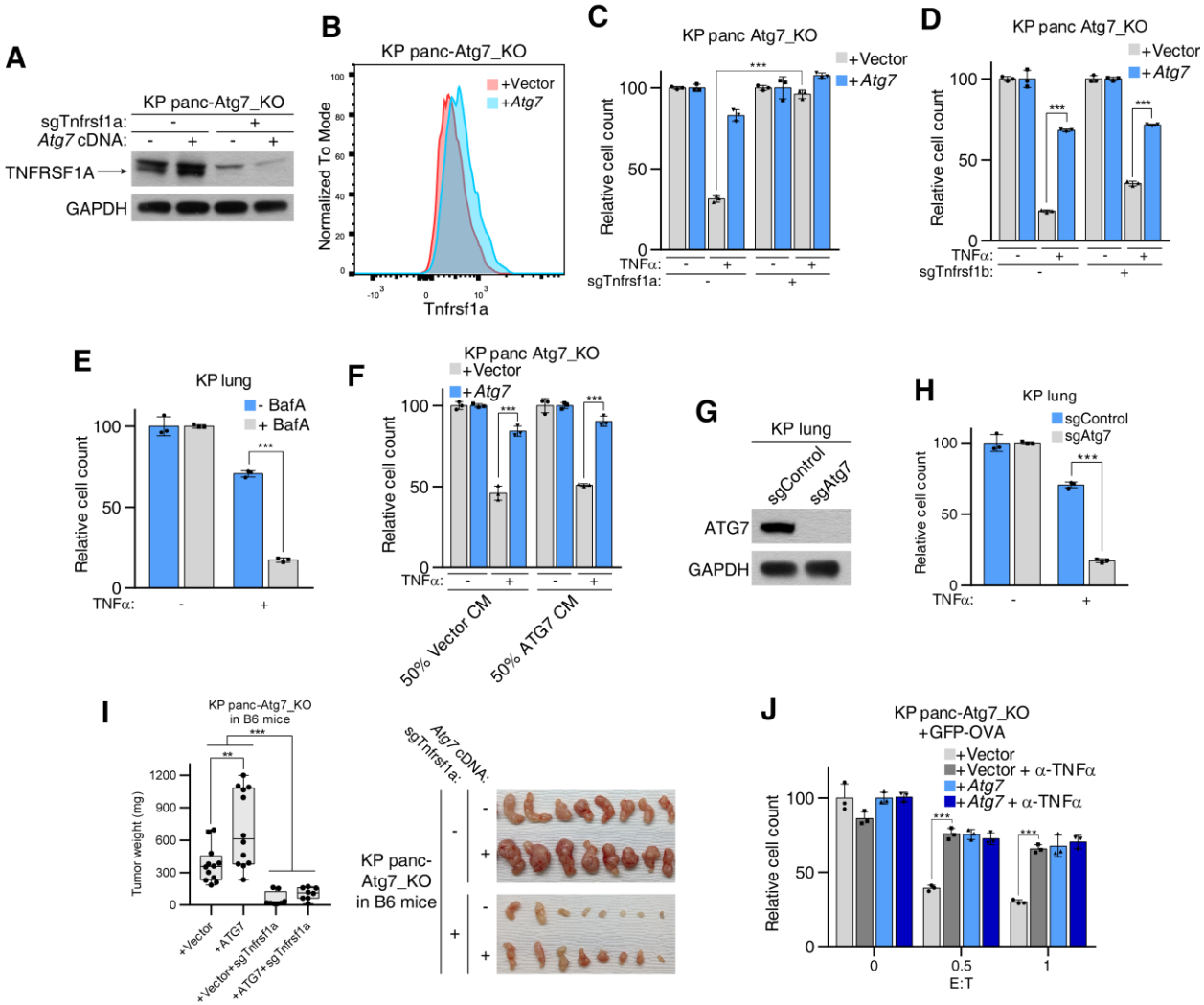
A
KP panc-Atg7_KO
sgTnfrsf1a:
Atg7 cDNA:
TNFRSF1A
GAPDH
B
KP panc-Atg7_KO
+Vector
+Atg7
Normalized To Mode
Tnfrsf1a
C
KP panc Atg7_KO
+Vector
+Atg7
Relative cell count
TNFα:
sgTnfrsf1a:
D
KP panc Atg7_KO
+Vector
+Atg7
Relative cell count
TNFα:
sgTnfrsf1b:
E
KP lung
- BafA
+ BafA
Relative cell count
TNFα:
F
KP panc Atg7_KO
+Vector
+Atg7
Relative cell count
TNFα:
50% Vector CM
50% ATG7 CM
G
KP lung
sgControl
sgAtg7
ATG7
GAPDH
H
KP lung
sgControl
sgAtg7
Relative cell count
TNFα:
I
KP panc-Atg7_KO
in B6 mice
Tumor weight (mg)
+Vector
+ATG7
+Vector+sgTnfrsf1a
+ATG7+sgTnfrsf1a
Atg7 cDNA:
sgTnfrsf1a:
KP panc-
Atg7_KO
in B6 mice
J
KP panc-Atg7_KO
+GFP-OVA
+Vector
+Vector + α-TNFα
+Atg7
+Atg7 + α-TNFα
Relative cell count
E:T

Finally, we tested whether TNFα sensitivity accounts for the increased T-cell killing of autophagy deficient mouse pancreatic cancer cells in an antigen specific *in vitro* co-culture assay. Specifically, we used an OVA antigen-expressing pancreatic cancer cell line as a target cell and OT-I CD8+ T cells as the effector cells. *Atg7* null cells and their *Atg7* expressing counterparts were co-cultured with OT-I CD8+ T cells for 48 hrs in the presence or absence of a neutralizing anti-mouse TNFα antibody. The remaining live cancer cells were counted after co-culture and revealed that the oversensitivity of autophagy deficient cancer cells to CD8+ T cells was completely rescued by addition of the anti-TNFα neutralizing antibody (**Figure 5.6J**). Altogether, these results suggest that autophagy protects PDAC cells from cell death in tumors resulting from TNFα secreted by immune cells such as CD8+ T cells.

Using parallel loss-of-function screens, our study provides a comparative compendium of metabolic dependencies of pancreatic cancer cells grown in culture and as tumors. Surprisingly, the high degree of correlation between metabolic essentialities *in vitro* and *in vivo* suggests that culture conditions may recapitulate a substantial portion of the metabolic dependencies in tumors and may provide a reasonable approximation to study cancer metabolism. Altogether, our screens reveal metabolic dependencies arising from microenvironmental limitations and the immune system, providing a resource for potential metabolism based anti-cancer strategies.

CHAPTER 6. Future directions and perspectives.

By employing both unbiased large-scale genetic screens and mechanistic biochemical studies, our work attempted to characterize the molecular regulation of saturated lipid toxicity and to decipher the metabolic dependencies of pancreatic tumor growth *in vivo*. By focusing on a specific metabolic dependency, we were able to map out all the major metabolic regulators of saturated lipid toxicity. We demonstrated that saturated lipid toxicity arose from accumulation of saturated phospholipids on the ER membrane as key upstream enzymes in the ER glycerolipid synthesis pathway were implicated in our screens. Through a whole genome screen, we also identified CHP1 as a previously uncharacterized regulator of ER glycerolipid synthesis. We revealed CHP1's activation of GPAT4 through its myristoylation moiety and showed the plasticity of cellular glycerolipid metabolism.

Though this strategy has been largely successful as an in-depth analysis of a known metabolic dependency, most of the metabolic challenges faced by cancer cells specifically in their unique endogenous microenvironment are not well known. We hence subsequently took an unbiased approach to identify the most critical metabolic dependencies of pancreatic tumor growth in an *in vivo* setting. By comparing cancer cells grown in culture and as tumors, we were able to reveal metabolic pathways that are only essential for tumors *in vivo* and not for cultured cells. Further analyses also confirmed metabolic dependencies due to environmental challenges such as heme synthesis and those due to immune regulation such as autophagy. Ultimately, we have demonstrated the validity of both approaches in characterizing metabolic dependencies of cancer growth and present an optimized framework in identifying potential therapeutic targets of cancer cells using a combination of these approaches. Our findings also revealed previously unappreciated facets of certain areas of cell metabolism including glycerolipid synthesis, heme metabolism and autophagy, leading to more outstanding questions. Further work will be necessary to address many of these remaining areas of interest. Potential experimental strategies and the implications of our findings will be discussed in this chapter.

6.1 Mechanism of saturated lipid toxicity

Toxicity of excess lipids has long been appreciated but the molecular mechanism of this toxicity is currently still under debate. Lipid toxicity or lipotoxicity is defined as the accumulation of lipids in cell types that do not normally store lipids. Adipocytes are specialized cell types that store lipids in large lipid droplets, but most cell types do not have this capacity and exhibit a variety of dysfunctional phenotypes upon lipid accumulation. For example, hepatocytes with excess fatty acids trigger apoptotic pathways, initiate ER stress and activate death receptors (Alkhouri et al., 2009). Excess fatty acids in the cardiac tissue also lead to the unfolded protein response in the ER and eventually apoptosis (Wende and Abel, 2010). It has been largely unclear why non-adipose cell types are unable to store large amounts of lipids while the direct link between excess lipids and the observed toxic phenotypes is also unclear. Apart from ER stress, other mechanisms of cellular lipid toxicity include oxidative stress (Hauck and Bernlohr, 2016) and accumulation of toxic lipid species such as ceramide (Rodriguez-Cuenca et al., 2017). However, these mechanisms are linked to specific minor lipid species and are unlikely generalizable phenomena observed in a wide variety of tissues. ER stress has been the most widely accepted mechanism for cellular lipid

toxicity, but the identity and role of the causative lipid species have remained unclear until recently.

In both studies involving liver (Alkhouri et al., 2009) and heart (Wende and Abel, 2010), saturated fatty acids have been implicated as contributing to the toxicity in cells. Studies have also shown that the ratio of saturated and unsaturated fatty acids governs lipid toxicity while increasing unsaturated fatty acids can decrease the toxic effects of saturated fatty acids (Chitraju et al., 2017; Listenberger et al., 2003). Increasing lines of evidence also suggest that diversion of lipid intermediates away from phospholipid synthesis through increasing flux of triacylglycerol synthesis (Ackerman et al., 2018) or beta oxidation (Wende and Abel, 2010) can prevent saturated lipid toxicity. Our findings by genetic characterization and a recent biophysical analysis of ER solid membrane formation (Shen et al., 2017) suggest with great confidence that the primary and most immediate mechanism of saturated lipid toxicity arises from the overproduction of saturated phospholipids on the ER membrane, leading to ER membrane rigidity, stress response and eventual apoptosis.

Our study consistently shows that ER glycerolipid synthesis is causal for saturated lipid toxicity. Inhibition of the ER glycerolipid synthesis pathway by knockout of CHP1 or GPAT4 prevented the synthesis of saturated phospholipids on the ER membrane. Upon CHP1-GPAT4 inhibition, acyl-CoA is also diverted away to alternative lipid synthesis pathways of acylcarnitine and cholesteryl esters. The opposing phenotypes of ACSL4 and ACSL3 knockouts upon treatment with saturated and unsaturated fatty acids also indicate an essential requirement for the balance of lipid saturation within the cells. Our results corroborate previous studies which have implicated saturated ER phospholipids as the main cause of cellular lipid toxicity. While we cannot conclusively rule out the contribution of other potential downstream effects of saturated lipids, our results demonstrate that formation of solid membrane on the ER is the most direct and immediate form of toxicity within the cell. It will be interesting to unravel the contributions from other proposed mechanisms of lipid toxicity such as oxidative stress and ceramide accumulation. One method to screen for other minor pathways of lipid toxicity would be to carry out a palmitate toxicity screen using CHP1 knockout cells. It is plausible that genes related to oxidative stress and the synthesis of other toxic lipid species will score, providing us a clue to the other minor or late pathways of saturated lipid toxicity when the main route through ER glycerolipid synthesis is inhibited. Although we have shown that ER solid membrane formation is the most relevant mechanism of toxicity in the cell lines that we have tested, it may still be possible that these other mechanisms may contribute more predominantly within other cell types.

6.2 Regulation of CHP1 and GPATs in glycerolipid synthesis

While there are a few reports on the regulation of GPAT4 (Pagac et al., 2016; Shan et al., 2010; Yu et al., 2018), precisely how ER GPAT activity is regulated in mammalian cells is not completely understood. We identify CHP1 as a major regulatory partner for GPAT4, but whether CHP1-GPAT4 interaction and CHP1 myristoylation are regulated steps of lipid metabolism is still unclear. Myristoylation does not alter GPAT4 localization and may cause a conformational change to prime its catalytic site. This suggests that potential upstream pathways may impact GPAT4 activity rather than its localization. However, future work combining molecular and structural studies will clarify the upstream pathways that regulate CHP1-GPAT4 interaction.

A clearer view of the interaction between CHP1 and GPAT4 will require additional structural analysis. Although we have identified the interaction domain on GPAT4, the interaction domain on CHP1 remains to be discovered. Identification of the interaction domain on CHP1 will help to clarify how CHP1 binds to GPAT4 and whether the interaction is regulated. Our immunoprecipitation experiments have shown that the interaction between CHP1 and GPAT4 is transient as the binding is tremendously improved by crosslinking before immunoprecipitation. This suggests that CHP1 or GPAT4 may be subject to upstream signaling pathways that alter their interaction or affinity. While we did not see any changes in interaction upon addition of free fatty acids with variable degrees of saturation, it is plausible that other upstream or downstream lipid species may be the signal sensed by the CHP1-GPAT4 complex. Our delivery of free fatty acids through conjugation to albumin may also not reflect the endogenous signals that feed into this glycerolipid synthesis pathway. Additional experiments that make use of small lipid molecule screens may be necessary to identify the metabolite that influences CHP1-GPAT4 interaction.

Additionally, the ability of the myristoyl moiety on CHP1 to activate GPAT4 also suggests that myristoylation itself may be a signal transduction mechanism. Myristate is a 12-carbon long saturated fatty acid and the myristoylation of CHP1 may be dependent on the concentration of myristate within the cells. We have also demonstrated that fatty acids of other lengths and saturation such as palmitate and palmitoleate can be conjugated to CHP1 at its myristoylation domain, in place of myristate. This raises the possibility that CHP1 myristoylation may not be strictly restricted to the conjugation of myristate but may also be inclusive of other more abundant fatty acids in the cell such as palmitate. However, we have not been able to demonstrate the functionality of other fatty acids replacing myristate at the myristoylation domain. Structural studies to solve the structure of the CHP1-GPAT4 complex in the presence and absence of the myrisoylation domain will be critical in understanding the activation of GPAT4's enzymatic activity.

The fact that CHP1 null cells survive and proliferate raises the question of how mammalian cells can proliferate without ER GPAT activity. Previous work suggests that mitochondrial GPATs are a major route of glycerolipid synthesis in some cell or tissue types and may compensate for ER GPATs (Lewin et al., 2008; Wendel et al., 2013). In contrast, our genetic screens with CHP1 null cells show an alternative metabolic pathway involving peroxisomal GNPAT as the major route for glycerolipid synthesis. It will be necessary to determine whether this metabolic plasticity is a feature of proliferating cells or other differentiated cell types as well. If true, our data raises the possibility that ER GPATs may use different metabolite pools from their mitochondrial counterparts. Our characterization of livers from Chp1 knockout mice also showed that lipid metabolism is minimally altered at basal conditions, without a significant increase in peroxisomal ether lipids. This suggests that there may be other more complex compensatory pathways in tissues, unlike that of cultured cells. Additional characterization of the lipid pools in each cellular compartment in each cell type will be required to fully understand the relative contribution of each GPAT isoform. Methods which rapidly isolate intracellular organelles such as MITO-Tag (Bayraktar et al., 2019) should be employed to differentiate the functioning GPAT isoform and its metabolite pools in each compartment.

Another interesting aspect of CHP1 is its role in modulating plasmalogen synthesis. Plasmalogens are a special class of phospholipids with a vinyl-ether bond at the *sn*-1 position of the glycerol backbone. Synthesis of plasmalogens begins in the peroxisome and is completed in the ER. Plasmalogens make up about 20% of all phospholipids in humans and are enriched in the brain

and heart. Defects in plasmalogen synthesis lead to a myriad of developmental deficiencies in the brain, heart, lung, and several other tissues (Braverman and Moser, 2012). Our results demonstrate that peroxisomal glycerolipid synthesis compensates for the loss of ER synthesis upon CHP1 inhibition. As plasmalogens are synthesized uniquely in the peroxisome, cellular plasmalogen levels increase significantly with loss of CHP1. This suggests that plasmalogen synthesis is diverted to compensate for the loss of ER glycerolipid synthesis. Although the molecular function of plasmalogen in the cell is still unclear, CHP1 inhibition may be a potential strategy to increase plasmalogen levels in patients with certain types of plasmalogen deficiency. It will also be necessary to determine the precise changes in peroxisomal lipid content through analysis of rapidly isolated peroxisomes (Ray et al., 2020).

6.3 Physiological function of CHP1 in other tissues

It will be of interest to understand whether our findings have therapeutic implications. As a conserved regulatory subunit in the membrane and triacylglycerol synthesis pathway, CHP1 likely plays a role in human physiology. Our studies on the Chp1 liver knockout animals indicate that Chp1 is necessary for the accumulation of excess lipids in livers in a NASH model, highlighting CHP1 and GPAT4 to be promising therapeutic targets for fatty liver disease patients. Combining with additional mechanistic studies on CHP1-GPAT4 regulation, it may be possible to develop small molecule inhibitors that disrupt the interaction the two proteins or prevent the myristoylation of CHP1. Given that inhibition of GPAT4 ameliorates metabolic syndrome in mouse models (Zhang et al., 2014, Kuhajda et al., 2011), targeting CHP1-GPAT4 interaction or CHP1 myristoylation with small molecule inhibitors may lead to effective therapies for dysfunctional lipid accumulation. Interestingly, we did not see overt differences in liver lipid content of Chp1 liver knockout mice at basal conditions. This may suggest that the liver derives most of its lipids from external sources or there are other GPATs that compensate for the loss of GPAT4. Our results are in disagreement with the findings from Gpat4 knockout mice where liver triacylglycerol content is severely reduced (Vergnes et al., 2006). However, our liver specific knockout may indeed present different phenotypes to the whole body Gpat4 knockout mice. It is plausible that Chp1 activity and glycerolipid synthesis present in other tissues compensate for the reduced glycerolipid synthesis in the liver. The differences between our Chp1 liver knockout mice and the whole body Gpat4 knockout mice also suggest that the liver may not be the top contributor of glycerolipids synthesized in the body. A better understanding of the physiological function of CHP1 in all other tissues will be necessary to elucidate its role in organismal metabolism.

A recent study identified CHP1 mutations in patients with cerebellar ataxia (Mendoza-Ferreira et al., 2018). Interestingly, similar ataxic phenotypes are associated with loss-of-function mutations in lipin enzymes downstream of GPATs (Dwyer et al., 2012). Since CHP1 may impact other biological processes (Lin and Barber, 1996), it should be determined whether any of these effects is related to CHP1's role in lipid metabolism. However, it is still puzzling why constitutive Chp1 knockout mice do not survive till birth. As our liver studies did not reveal any overt phenotypes in the liver-specific Chp1 knockout mice, it is unlikely that the lethality is caused by an inhibition of lipid metabolism in the liver. While we are currently attempting to probe the role of Chp1 in adipose tissue with an adipose-specific Chp1 knockout mouse model, it may also be probable that Chp1 is essential in the early development of neurons given the ataxic phenotypes associated with CHP1 mutations in humans. Careful analysis of neurons and other cell types may be necessary to fully elucidate the physiological role of CHP1, especially in organs not involved in lipid

metabolism. Additionally, it will be necessary to identify whether CHP1 does have a role in the regulation of the sodium-proton pump NHE1 in specific tissues, as suggested by previous studies (Lin and Barber, 1996).

6.4 Lipid metabolic dependencies in tumors

As saturated lipid toxicity is implicated in hypoxic cancers (Ackerman et al., 2018) and we have characterized most of the critical metabolic regulators of lipid toxicity in our *in vitro* screens, we initially expected some of the lipid saturation genes to be essential in our *in vivo* screens. Not only did we not see any lipid saturation genes being essential *in vivo*, but our screen results also suggest that tumor cells may not be dependent on *de novo* lipid synthesis. Genes involved in *de novo* lipid synthesis such as *Acly* and *Pcyt2* score as essential only in cultured cells and not in tumors *in vivo*. This suggests that cancer cells in culture are most likely limited by the availability of fatty acids in the culture media and depend on *de novo* lipid synthesis for their lipid supplies. On the other hand, our data suggest that cancer cells *in vivo* may have a greater availability of fatty acids and lipids in circulation and in the tumor microenvironment. This is also in line with a previous tracing study which showed that cancer cells prefer exogenous fatty acids as a source of membrane lipids (Yao et al., 2016). However, this lipid availability will likely be highly dependent on tumor types and the tissue environment where the tumor is growing. As our tumors are derived from pancreatic cancer cells engrafted as subcutaneous tumors, our results indicate that at least in this specific microenvironment, lipid availability is not limiting for tumor growth. Under such circumstances, it is reasonable that lipid saturation genes are not essential for *in vivo* tumor growth even when hypoxic stress is present. Our results and other studies have indicated that availability of unsaturated fatty acids in the environment greatly reduces the toxicity of saturated lipids. If lipids are not limited in the tumor microenvironment, it reasons that both saturated and unsaturated lipids should be largely available, dampening the effect of SCD inhibition within the cells by hypoxia. Targeting lipid saturation for cancer therapy will thus be highly dependent on the tumor type and microenvironment. It will be necessary to probe for lipid availability in different tissues by lipidomics analysis of interstitial fluids to assess the availability of unsaturated fatty acids in the tumor microenvironment.

6.5 Pancreatic tumor and its complex desmoplasia

Our work characterized the metabolic dependencies of pancreatic tumor growth as a subcutaneous engraftment and validated some of the dependencies such as autophagy in its orthotopic setting. However, one unique characteristic of pancreatic tumors is the presence of a dense desmoplasia consisting of fibroblasts and stellate cells which contribute significantly to the growth and survival of pancreatic cancer cells (Korc, 2007). Desmoplastic stromal cells provide multiple growth factors and cytokines to fuel cancer cell proliferation. Additionally, pancreatic stellate cells have also been found to directly provide cancer cells with alanine as a metabolic fuel source (Sousa et al., 2016). Although our model can account for some of the direct environmental influences on pancreatic cancer cell growth in an *in vivo* setting, the lack of stromal cells in our engraftment fails to account for some of the critical cancer-stromal interactions in pancreatic tumors.

The next step to better model the endogenous pancreatic tumor microenvironment will be to include stromal cells in the engraftment by co-injection of cancer cells and pancreatic stellate cells

(Hwang et al., 2008). Carrying out our *in vivo* genetic screens in the presence of stromal cells will allow us to identify stromal-dependent metabolic liabilities of pancreatic tumor growth that will not have been discovered through mono-injection of cancer cells. A complementary approach will be to infect the stellate cells with the metabolism sgRNA library at the same time but with a different barcode. This will allow us to carry out a two-cell type screen by screening for genes essential in both cancer cells and stromal cells when they are interacting together in a tumor. Such an approach will better model the endogenous interactions between the two cell types and screen for metabolic co-dependencies simultaneously in both cell types. Altogether, this strategy enables us to identify corresponding metabolic pathways involved in stromal-supported cancer cell growth and will allow us to further validate them in a more controlled *in vitro* co-culture system.

6.6 Regulation of heme synthesis, degradation, and transport in cancer cells

Our work identified a subset of metabolic dependencies unique to the tumor environment and shared by both *Kras* mutant pancreatic and lung cancer cells. In particular, we discovered heme synthesis as a common metabolic liability in tumors, indicating the significance of recent efforts to better model tumor nutrient conditions (Cantor et al., 2017; Vande Voorde et al., 2019). The dependency on heme synthesis is likely due to upregulation of Hmox1 through hypoxia or ROS, which imposes a stronger demand for heme availability in subcutaneously engrafted tumors. Interestingly, Hmox1 has previously been shown to be regulated by multiple stress conditions and signaling pathways (Alam and Cook, 2007). For example, lung tumors upregulate Hmox1 through activation of NRF2, the master regulator of the antioxidant response pathway (Lignitto et al., 2019). Despite this, the precise mechanism for Hmox1 upregulation in different tumor contexts remains to be identified. Our results also demonstrate that individual knockout of Hif1a or Hif2a fails to prevent the upregulation of Hmox1 by hypoxia. This corroborates previous studies that indicate the presence of multiple components to transcriptionally activate *Hmox1* (Alam and Cook, 2007). Better characterization of the transcriptional control of *Hmox1* will be necessary to elucidate how it can be regulated and targeted in cancer progression.

Though heme is essential for cell survival, specifically as a cofactor for many key enzymes, its transport and regulation within the cell is largely uncharacterized. Heme is synthesized within the mitochondria and must be transported to each cellular compartment where it is required. However, the transporters for heme both on the mitochondrial and plasma membranes remain unconfirmed (Swenson et al., 2020). Since we have identified heme synthesis as a metabolic liability for tumors under environmental challenges, a better characterization of the regulation and transport of heme in cancer cells will be crucial to advance the development of therapeutic strategies which limit heme synthesis in cancer patients. Our screening approach presents a viable strategy to identify the plasma membrane and organellar membrane transporters of heme. As we have demonstrated that cells with knockouts in heme synthesis genes are viable, we can compare knockout cells to their wild type counterparts and screen for essential genes only in the heme synthesis knockout cells. Genes that score in this screen will highly likely be heme transporters or other regulators of heme availability within the cell.

6.7 Autophagic control of proteins in immune signaling pathways

Interestingly, among all the scoring pathways in our focused *in vivo* genetic screen, autophagy was the only metabolic process that enabled pancreatic cancer cells to evade the immune system. While our experiments suggest a protective role for autophagy from TNFα-mediated cell death, previous work suggests that autophagy is also involved in MHC-I presentation and impacts the trafficking of surface MHC-I molecules (Loi et al., 2016; Yamamoto et al., 2020). Given that the effect of autophagy loss on MHC-I expression is variable in different cell lines, autophagy may enable immune evasion through multiple mechanisms depending on the context. Additionally, recent studies also corroborated our finding that autophagy protects cancer cells from TNFα-mediated cell death by T cells (Lawson et al., 2020; Young et al., 2020). Furthermore, the complexity of the tumor microenvironment does not preclude that a combination of MHC-I presentation and cytokine insensitivity both may play roles in immune evasion.

While loss of autophagy increases the TNFα sensitivity of pancreatic cancer cell lines, the exact mechanism of this enhanced sensitivity and how autophagy protects cells from cytokine mediated death are not well understood. Though several studies have associated autophagy with TNFα signaling in other cell types due to increased necroptosis (Lim et al., 2019) or Rip1-dependent apoptosis (Orvedahl et al., 2019), our results show a similar phenotype in pancreatic cancer cells independent of Rip1. A TNFα downstream adaptor protein TRADD has also been implicated as being regulated by autophagy and is necessary for signal transduction to apoptotic pathways (Xu et al., 2020). These findings suggest that autophagy may be associated with other downstream TNFα adaptor proteins. TNFα is a multifunctional cytokine that has been shown to both promote and suppress tumor growth in different contexts (Wang and Lin, 2008). Consistent with this, blocking TNFα *in vivo* is disruptive to tumor growth and may mask the effect of autophagy loss on TNFα-mediated apoptosis. Future work such as immunoprecipitation is required to determine affected downstream adaptor proteins, which may improve our understanding of how autophagy protects cells from TNFα mediated cell death and lead to therapeutic strategies. As interferon-γ signaling was also implicated in our tumor RNAseq data, it is also likely that autophagy may be affecting the signaling of other immune pathways through the potential regulation of their downstream adaptors. Another immune signaling pathway, cGAS-STING, has also been found to be dependent on autophagy as STING signaling activates autophagy (Gui et al., 2019) while STING itself is also degraded by autophagy (Prabakaran et al., 2018). Since many pancreatic cancers display high autophagic flux and have immunosuppressive environments, we reveal an underappreciated facet of targeting autophagy-associated immunomodulation of pancreatic tumor growth, which may be effectively combined with current immunotherapies.

It will also be necessary to differentiate whether the effect of autophagy on TNFα signaling is dependent on the autophagic process itself or the non-autophagic functions of the autophagy related proteins. Our metabolism library only contained two autophagy genes (*Atg7* and *Atg5)* and both scored as essential for *in vivo* tumor growth in immunocompetent mice. A smaller custom library that includes all the known autophagy related genes will be required to specifically identify the genes and steps in the autophagic process that is necessary for the evasion of TNFα-induced cell death. Alternatively, if we were to identify the TNFα adaptor protein that is mediated by autophagy related proteins, rapid isolation of the lysosome by LysoIP (Abu-Remaileh et al., 2017) and determination of the adaptor protein within the lysosome with pharmacological inhibition of autophagy will clarify whether the effect is dependent on the autophagic process or only on the association with autophagy related proteins.

6.8 Need for better *in vivo* screening techniques of tumor growth

In this work, we unbiasedly characterized the metabolic dependencies of pancreatic tumor growth *in vivo* through CRISPR genetic screens. However, we are aware of several limitations to our screening approach. As *in vivo* screening approach for a comprehensive CRISPR library requires a large number of tumors to achieve efficient representation of guides, we used subcutaneous tumors rather than orthotopic counterparts or GEMMs, which are physiologically more relevant. While it is possible that we may have missed some organ-specific metabolic liabilities, our screens still provide a valuable resource for the comparison of metabolic dependencies of pancreatic cancer cells in culture and *in vivo*. Additionally, it should be noted that, within large-scale pooled CRISPR screens, we culture a population of knockout cells with those that still express the functional gene product. This heterogeneity may enable the transfer of metabolites and growth factors and may mask certain dependencies under pooled conditions. Finally, the number of cell lines used in this study is limited. Therefore, metabolic limitations and downstream mechanisms we identified may not be generalizable to most tumor types. We also mainly used engrafted tumor cells and not GEMMs, which can best recapitulate tumor biology even from an early initiation step.

To carry out genetic screens in more physiologically relevant models such as GEMMs, alternative methods to introduce sgRNAs and screen for genes in the tumor initiation steps will be necessary. Current trends have included the introduction of sgRNA libraries into tissues through direct injection or the use of tissue-tropic adeno-associated viruses (AAVs) (Chow and Chen, 2018). At their current stages, these techniques are limited in their efficiency and accuracy. Infection rates are much more variable in tissues of live animals and it is still difficult to control for cells with multiple sgRNAs infected. Better optimization and development will be required to effectively screen for oncogenes and tumor suppressors in their endogenous context. As new screening techniques emerge, more advanced genetic screens, especially in GEMMs, would enable us to better identify metabolic dependencies and adaptations of individual tumor types in their natural microenvironment.

6.9 Towards a complete understanding of cell metabolism

This work successfully characterized the genetic regulators of saturated lipid toxicity and identified CHP1 as a novel mediator of glycerolipid synthesis. Additionally, we revealed the environmental and immune-related metabolic dependencies of pancreatic tumor development, providing a model to systematically assess metabolic liabilities of each cancer type. Despite the known limitations of CRISPR screening techniques and their reduced effectiveness *in vivo*, our approaches undoubtedly present a path forward to identify metabolic dependencies of tumor growth. We hope this approach can be optimized and extended to screen for metabolic dependencies of tumors in additional tissue types, specifically in orthotopic tumors and GEMMs. As we increasingly appreciate the heterogeneity of cancer cells and as cancer therapy becomes more personalized, individual genetic screenings of cell lines can only account for a small percentage of human patients. However, studying cancer metabolism as a model also allows us to unravel fundamental discoveries in cell and organismal metabolism. Our approaches allowed us to discover CHP1 as a novel metabolic regulator and also identify new roles of autophagy in immune regulation. A combination of large-scale screens and mechanistic studies will thus continue to help us address both the translational and basic questions in tumor biology.

MATERIALS AND METHODS

Table 7.1. List of key reagents used in this work.

REAGENT	SOURCE	IDENTIFIER
Antibodies		
ACSL4/ACSL3	GeneTex	GTX100260, RRID:AB_1240790
β-ACTIN	GeneTex	GTX109639, RRID:AB_1949572
CHP1	GeneTex	GTX113936, RRID:AB_2036564
GFP	Proteintech	66002-1-Ig, RRID:AB_11182611
Custom GPAT4	This paper (YenZym)	N/A
GPAT3	GeneTex	GTX87708, RRID:AB_10724633
GPAT1	GeneTex	GTX85034, RRID:AB_10721826
HA	Cell Signaling	3724, RRID:AB_1549585
GNPAT	GeneTex	GTX81658, RRID:AB_11168329
FLAG	Sigma	F1804, RRID:AB_262044
CALNEXIN	Cell Signaling	2679S, RRID:AB_2228381
HMBS	GeneTex	GTX113460, RRID:AB_10617763
GAPDH	Cell Signaling Technology	2118, RRID:AB_561053
HMOX1	Proteintech	10701-1-AP, RRID:AB_2118685
ATG7	Cell Signaling Technology	8558, RRID:AB_10831194
LC3B	Cell Signaling Technology	3868, RRID:AB_2137707
Caspase-8	Cell Signaling Technology	4790, RRID:AB_10545768
Cleaved caspase-8	Cell Signaling Technology	8592, RRID:AB_10891784
Caspase-3	Cell Signaling Technology	9665, RRID:AB_2069872
TNF-R1	Cell Signaling Technology	13377, RRID:AB_2798194

Anti-mouse H-2Kb/H-2Db	BioLegend	114602, RRID:AB_313593
PE anti-mouse H-2Kb/H-2Db	BioLegend	114607, RRID:AB_313598
Anti-mouse H-2Kb	Dr. Jon Yewdell	
PE anti-human HLA-A,B,C	BioLegend	311405, RRID:AB_314874
PE anti-mouse PD-L1	BioLegend	124307, RRID:AB_2073557
RIP	Cell Signaling Technology	3493, RRID:AB_2305314
Phospho-RIP (Ser166)	Cell Signaling Technology	31122, RRID:AB_2799000
BUV395 Rat Anti-Mouse CD45	BD Biosciences	564279, RRID:AB_2651134
Brilliant Violet 605 anti-mouse CD8a	BioLegend	100744, RRID:AB_2562609
Brilliant Violet 711 anti-mouse CD3ε	BioLegend	100349, RRID:AB_2565841
Brilliant Violet 785 anti-mouse NK-1.1	BioLegend	108749, RRID:AB_2564304
Brilliant Violet 421 anti-mouse CD4	BioLegend	100438, RRID:AB_11203718
APC anti-mouse IFN-γ	BioLegend	505810, RRID:AB_315404
APC anti-mouse TNF-R1	BioLegend	113005, RRID:AB_2208780
Anti-mouse CD16/CD32	BioXCell	BE0307, RRID:AB_2736987
Anti-rabbit IgG, HRP-linked	Cell Signaling	7074S, RRID:AB_2099233
Peroxidase Goat Anti-Rabbit IgG (H+L)	Jackson ImmunoResearch Labs	111-035-144, RRID:AB_2307391
m-IgGκ BP-HRP	Santa Cruz	sc-516102, RRID:AB_2687626
Rabbit IgG, Isotype Control	Invitrogen	026102, RRID:AB_2532938
Anti-Mouse Secondary Antibody, Alexa Fluor 568	Thermo Fisher Scientific	A10037, RRID:AB_2534013
Anti-Rabbit Secondary Antibody, Alexa Fluor 488	Thermo Fisher Scientific	A21206, RRID:AB_141708
Bacterial and Virus Strains		
NEB Stable Competent E. coli	NEB	C3040
Chemicals, Peptides, and Recombinant Proteins		
RPMI 1640	Gibco	11875

DMEM	Gibco	11965
Trypsin	Gibco	25200
BSA Fatty Acid-free	Alfa Aesar	J64944
Palmitic acid	Cayman Chemical	10006627
Arachidonic acid	Cayman Chemical	90010
Penicillin-Streptomycin	Gibco	15140122
FBS	Sigma	12306C
Charcoal/Dextran Treated FBS	HyClone	SH30068
Methanol	Fisher Scientific	A456
Water	Fisher Scientific	W6
Chloroform	Fisher Scientific	C607
[U-^{13}C16]-palmitic acid	Cambridge Isotope Laboratories	CLM-409
Phusion High-Fidelity PCR Master Mix with HF Buffer	NEB	M0531
BsmBI	NEB	R0580
T4 DNA Ligase	NEB	M0202
X-tremeGENE 9 DNA Transfection Reagent	Roche	6365779001
BamHI	NEB	R3136
NotI	NEB	R3189
Polybrene	Sigma	H9268
Puromycin	Sigma	P8833
Blasticidin	Invivogen	ant-bl
Matrigel Growth Factor Reduced	Corning	354230
MEM Amino Acids Solution (50X)	Thermo Fisher	11130
Fos-choline-13	Anatrace	F310
Alexa Fluor 488 Phalloidin	Invitrogen	A12379
HCS LipidTOX Deep Red Neutral Lipid Stain	Invitrogen	H34477
Isopropanol	Fisher Scientific	A461
Oil red O	Sigma	O0625
Nile red	Sigma	72485
TRIzol	Invitrogen	15596026
Fluoromount-G	Southern Biotech	0100-01
Dithiobis(succinimidyl propionate)	Thermo Fisher Scientific	22585
Anti-FLAG-M2 Affinity Gel	Sigma	A2220
Pierce Anti-HA Magnetic Beads	Thermo Fisher Scientific	88837
[^{14}C]-glycerol-3-phosphate	PerkinElmer	NEC608V050uci
ScintiSafe Econo Cocktail	Fisher Scientific	SX22
Bifunctional x-alk-16	(Peng and Hang, 2015)	N/A
SYBR Green PCR Master Mix	Applied Biosystems	4309155
Normal donkey serum	Jackson ImmunoResearch	017-000-121

Recombinant Mouse IL-2	BioLegend	575404
Dynabeads Mouse T-Activator CD3/CD28	Thermo Fisher	11456D
Recombinant Mouse IFN-γ	BioLegend	575306
Recombinant Human IFN-γ	BioLegend	570206
APC Annexin V	BioLegend	640920
DAPI	Thermo Fisher	D1306
Zombie NIR Fixable Viability Dye	BioLegend	423106
Recombinant Mouse TNF-α	BioLegend	575202
Recombinant Human TNF-α	BioLegend	570104
Bafilomycin A1	Cayman Chemical	11038
Hemin	Sigma-Aldrich	H9039
Sodium pyruvate	Sigma-Aldrich	P2256
Necrostatin-1	Cayman Chemical	11658
Z-VAD-FMK	Selleckchem	S7023
ProLong Gold Antifade Mountant	Thermo Fisher	P36934
Metabolomics Amino Acid Mix Standard	Cambridge Isotope Laboratories	MSK-A2-1.2
XF RPMI Base medium, pH 7.4 (for seahorse)	Agilent	103576-100
Oligomycin	Sigma	O4876
FCCP	Santa Cruz	sc-203578
Antimycin A	MilliporeSigma	A8674-25MG
Dynabeads M-280 Sheep Anti-Rabbit IgG	Invitrogen	11203D
Molecular Probes ER-Tracker Blue-White DPX	Invitrogen	E12353
HBSS	Gibco	14025092
Fibronectin	Corning	54008
Critical Commercial Assays		
CellTiter-Glo Luminescent Cell Viability Assay	Promega	G7573
DNeasy Blood & Tissue Kit	Qiagen	69506
Zyppy Plasmid Miniprep Kit	Zymo Research	D4019
Pierce BCA Protein Assay Kit	Thermo Fisher Scientific	23225
CD8a+ T Cell Isolation Kit, mouse	Miltenyi Biotec	130-104-075
Superscript III First Strand Synthesis System	Invitrogen	18080051
Seahorse XF Palmitate-BSA fatty acid oxidation (FAO) Substrate	Agilent	102720-100
RNeasy Mini Kit	Qiagen	74104
Experimental Models: Cell Lines		
Jurkat	ATCC	N/A
HeLa	ATCC	N/A
HepG2	Dr. Wei Min	N/A
HEK293T	ATCC	N/A
KP panc	Dr. Nabeel M. Bardeesy	N/A
KP lung	Dr. Nabeel M. Bardeesy	N/A

AsPC-1	ATCC	N/A
MIA PACA-2	ATCC	N/A
PATU-8988T	ATCC	N/A
3T3-F442A	Dr. Paul Cohen	N/A
Experimental Models: Organisms/Strains		
Mouse: C57BL/6J	The Jackson Laboratory	000664
Mouse: C57BL/6	Charles River	027
Mouse: B6.129S7-Rag1tm1Mom/J (Rag1 KO)	The Jackson Laboratory	002216
Mouse: C57BL/6-Tg(TcraTcrb)1100Mjb/J (OT-I)	The Jackson Laboratory	003831
Mouse: NOD.Cg-Prkdcscid Il2rgtm1Wjl/SzJ (NSG)	The Jackson Laboratory	005557
C. elegans: N2 wild type	Dr. Shai Shaham	N/A
D. melanogaster: RNAi of *white*	Bloomington Drosophila Stock Center	33623
D. melanogaster: RNAi of *Elm*	Vienna Drosophila Stock Center	108624
D. melanogaster: *Actin5C* Gal4	Bloomington Drosophila Stock Center	3954
Oligonucleotides		
DNA oligonucleotides and primers	This Study	See **Table 7.2**
Recombinant DNA		
CRISPR Cas9 sgRNA Human Library	(Birsoy et al., 2015)	N/A
CRISPR Cas9 sgRNA KO mouse metabolism library	This Study	N/A
CRISPR Cas9 sgRNA KO focused mouse metabolism library	This Study	N/A
pLenti CRISPR	Addgene	49535
pLenti CRISPR V2	Addgene	52961
pMXS-IRES-Blast	Cell Biolabs	RTV-016
pSECB	(Minton et al., 2018)	N/A
pLenti CRISPR sgACSL4_1	This Study	N/A
pLenti CRISPR sgACSL4_2	This Study	N/A
pLenti CRISPR sgACSL3_1	This Study	N/A
pLenti CRISPR sgACSL3_2	This Study	N/A
pLenti CRISPR sgCHP1_1	This Study	N/A
pLenti CRISPR sgCHP1_2	This Study	N/A
pMXS-IRES-Blast ACSL4	This Study	N/A
pMXS-IRES-Blast ACSL3	This Study	N/A
pMXS-IRES-Blast CHP1	This Study	N/A
pLenti CRISPR sgmCHP1_1	This Study	N/A

pLenti CRISPR sgmCHP1_2	This Study	N/A
pMXS-IRES-Blast FLAG-CHP1	This Study	N/A
pMXS-IRES-Blast 3XFLAG-CHP1	This Study	N/A
pLenti CRISPR sgGPAT4_1	This Study	N/A
pLenti CRISPR sgGPAT4_2	This Study	N/A
pMXS-IRES-Blast HA-GPAT4	This Study	N/A
pMXS-IRES-Blast HA-GPAT4-ΔN	This Study	N/A
pMXS-IRES-Blast HA-GPAT4-ΔS	This Study	N/A
pMXS-IRES-Blast HA-GPAT4-ΔN1/2	This Study	N/A
pMXS-IRES-Blast HA-GPAT4-ΔN1	This Study	N/A
pMXS-IRES-Blast HA-GPAT4-ΔN2	This Study	N/A
pMXS-IRES-Blast HA-GPAT4-ΔN3	This Study	N/A
pMXS-IRES-Blast HA-GPAT4-ΔNs1	This Study	N/A
pMXS-IRES-Blast HA-GPAT4-ΔNs2	This Study	N/A
pMXS-IRES-Blast HA-GPAT4-ΔNs3	This Study	N/A
pMXS-IRES-Blast HA-GPAT4-ΔNs4	This Study	N/A
pMXS-IRES-Blast HA-GPAT4-ΔNs5	This Study	N/A
pMXS-IRES-Blast HA-GPAT4-ΔNs6	This Study	N/A
pMXS-IRES-Blast HA-GPAT4-ΔNs7	This Study	N/A
pMXS-IRES-Blast HA-GPAT4-ΔNs8	This Study	N/A
pMXS-IRES-Blast HA-GPAT4-ΔNs9	This Study	N/A
pMXS-IRES-Blast HA-GPAT4-ΔNs10	This Study	N/A
pLenti CRISPR sgGPAT3	This Study	N/A
pMXS-IRES-Blast FLAG-CHP1-NES_mut	This Study	N/A
pMXS-IRES-Blast FLAG-CHP1-myr_mut	This Study	N/A
pMXS-IRES-Blast FLAG-CHP1-EF_mut	This Study	N/A
pMXS-IRES-Blast FLAG-CHP1-myr_EF_mut	This Study	N/A
pMXS-IRES-Blast 3XFLAG-CHP1-myr_mut	This Study	N/A
pSECB sgCHP1	This Study	N/A
pLenti CRISPR V2 sgGNPAT_1	This Study	N/A
pLenti CRISPR V2 sgGNPAT_2	This Study	N/A
pLenti CRISPR V2 sgmHmbs	This Study	N/A
pSECB sgmHmox1	This Study	N/A
pLenti CRISPR V2 sgmAtg7	This Study	N/A
pLenti CRISPR V2 sgATG7	This Study	N/A
pLenti CRISPR V2 sgmRipk1	This Study	N/A
pLenti CRISPR V2 sgmTnfrsf1a	This Study	N/A
pLenti CRISPR V2 sgmTnfrsf1b	This Study	N/A
pLenti CRISPR V2 sgmHif1a	This Study	N/A
pLenti CRISPR V2 sgmEpas1	This Study	N/A
pLenti CRISPR V2 sgmTap1	This Study	N/A
pMXS-IRES-Blast mAtg7	This Study	N/A
pMP71-eGFP-OVA	This Study	N/A
pMP71-eGFP	This Study	N/A
pMXS-IRES-Blast cytoLbNOX	This Study	N/A
pMXS-IRES-Blast mitoLbNOX	This Study	N/A

pMXS-IRES-Blast mHmox1	This Study	N/A
pMXS-IRES-Blast mHmox1-H25A	This Study	N/A
Other		
Z2 Coulter Counter	Beckman	Model Z2
SpectraMax Microplate Reader	Molecular Devices	Model M3
Primovert Microscope	Carl Zeiss	415510-1105-000
REVOLVE4 Microscope	Echo Laboratories	FJSD1001

Cell culture

The mouse cell line 3T3-F442A was kindly provided by Dr. Paul Cohen (Rockefeller University). The female mouse cell lines KP panc and KP lung were kindly provided by Dr. Nabeel M. Bardeesy (Massachusetts General Hospital Cancer Center). Human cells lines Jurkat, HeLa, HepG2, AsPC-1, MIA-PaCa-2, PATU-8988T and HEK293T were purchased from the ATCC. Cell lines were verified to be free of mycoplasma contamination and the identities of all were authenticated by STR profiling. Jurkat, KP panc, KP lung and AsPC-1 cells were maintained in RPMI media (Gibco) containing 2 mM glutamine, 10% fetal bovine serum, 1% penicillin and streptomycin. HeLa, HepG2, 3T3-F442A, MIA PaCa-2, PATU-8988T and HEK293T cells were maintained in DMEM media (Gibco) containing 4.5g/L glucose, 110mg/L pyruvate, 4mM glutamine, 10% fetal bovine serum, penicillin, and streptomycin. For experiments involving sensitivity to fatty acids, regular RPMI was supplemented with 10% charcoal/dextran treated fetal bovine serum (HyClone). All cells were maintained at 37°C and 5% CO_2.

Mouse studies

All animal studies and procedures were conducted according to a protocol approved by the Institutional Animal Care and Use Committee (IACUC) at the Rockefeller University. All mice were maintained on a standard light-dark cycle with food and water ad libitum, unless otherwise stated. High fat diet (D12492) and NASH diet (D12492) were from Research Diets. At the end of diet studies, mice were fasted for 6 hours before sacrifice. All tumor studies were randomized and injections were performed by blinded investigators. Subcutaneous tumor growth experiments were performed by injecting subcutaneously into the flanks of female 6-8-week-old C57BL/6J, Rag1 KO or NOD scid gamma (NSG) mice (The Jackson Laboratory), unless otherwise indicated at 1-2 x 10^6 cells in 100 uL 40% Matrigel (Corning). Mice were sacrificed and tumors were dissected after 2-3 weeks. In no cases did any tumor size surpass the limit permitted by our protocol (2 cm). The immune-dependent difference we observed is not due to rejection by mice of the opposite gender as almost identical results were obtained in C57BL/6J mice of both genders (Figure S3C). For orthotopic pancreas injections, mice were anaesthetized by an intraperitoneal injection of ketamine. A small incision was made on the upper left quadrant of the abdomen and the pancreas was externalized. Cells were suspended in 50 μl of Matrigel : PBS (1:1) solution and injected into the pancreatic tail with insulin syringes (29-gauge needle, BD). Approximately 1×10^5 KP panc cells were injected and after the procedures, the peritoneum was closed with a 3-0 Vicryl Violet suture (Ethicon), and the skin was closed using the BD AutoClip Wound Closing System (BD). Mice were sacrificed and tumors were dissected after 2 weeks.

CRISPR-based screens

The whole genome, metabolism and focused sgRNA libraries were designed and screens were performed as previously described (Zhu et al., 2021; Garcia-Bermudez et al., 2019; Zhu et al., 2019; Wang et al., 2017). Focused sgRNA screens for KP panc and KP lung cell lines in C57BL/6J and NSG mice were carried out together. Oligonucleotides for sgRNAs were synthesized by CustomArray Inc. and amplified by PCR. For *in vivo* screens, library infected cells were injected subcutaneously into the flanks of 6-8-week-old C57BL/6J or NOD scid gamma (NSG) mice (The Jackson Laboratory) at 1 x 10^6 cells in 100 uL 40% Matrigel. Tumors were grown for 2-3 weeks and gDNAs were extracted with DNeasy Blood & Tissue Kit (Qiagen). gDNAs from 4 tumors were pooled as one sample and amplified by PCR. PCR amplicons were then sequenced together with the initial and *in vitro* samples as per standard *in vitro* CRISPR-based screens. We then performed PCA analysis on normalized counts from each mouse, as well as the initial and *in vitro* samples. Based on this outlier analysis, one of the mice was filtered from the downstream analysis. Sequencing counts from *in vivo* tumor samples were then summed, normalized (count per million), and analyzed as a single condition. The fitness score for each guide was calculated as $\log_2$ ratio of normalized counts. The median of the guides was used as the fitness score for each gene, and t test was used to assess whether the guides were significantly deviating from 0. For iPAGE analysis of fitness scores between *in vivo* and *in vitro* screens, the differential scores across all genes were used as input to iPAGE with the following parameters: ebins=3, max_p=0.05, and using MSigDB c2 gene sets. A complete list of differential gene scores for each screen is provided in Table S1.

Immunoblot

Cell pellets were washed twice with ice-cold PBS prior to lysis in RIPA buffer (10 mM Tris-Cl pH 7.5, 150 mM NaCl, 1 mM EDTA, 1% Triton X-100, 0.1% SDS) supplemented with protease inhibitors and phosphatase inhibitors (Roche). For liver and tumor tissue samples, 50 mg tissues were taken from each sample and homogenized in RIPA buffer by Bead Ruptor 24 (Omni International). For immunoblots with GPAT4, cell pellets were lysed with fos-choline buffer (50 mM Tris-HCl pH 7.5, 150 mM NaCl, 1 mM EDTA, 0.2% fos-choline-13 (Anatrace)) supplemented with protease inhibitors and phosphatase inhibitors (Roche). Each lysate was sonicated and, after centrifugation for 5 min at 4°C and 20,000 x g, supernatants were collected. Sample protein concentrations were determined by using Pierce BCA Protein Assay Kit (Thermo Scientific) with bovine serum albumin as a protein standard. Samples were resolved on 12% or 10-20% SDS-PAGE gels and analyzed by immunoblotting with standard protocols.

Generation of knock-out and cDNA overexpression cell lines

sgRNAs were cloned into lentiCRISPR-v1 or -v2 linearized with BsmBI by T4 ligase (NEB). Full list of sgRNAs used is provided in **Table 7.2**. sgRNA expressing vector along with lentiviral packaging vectors Delta-VPR and CMV VSV-G were transfected into HEK-293T cells using the XTremeGene 9 transfection reagent (Roche). Similarly, for overexpression cell lines, gBlocks (IDT) containing the cDNA of interest were cloned into pMXS linearized with BamHI and NotI by Gibson Assembly (NEB). cDNA vectors along with retroviral packaging vectors gag-pol and CMV VSV-G were transfected into HEK-293T cells. For FLAG and HA tagged proteins, tags were added to the C terminus of each protein. The virus-containing supernatant was collected 48

hrs after transfection and passed through a 0.22 μm filter to eliminate cells. Target cells in 6-well tissue culture plates were infected in media containing 8 μg/mL of polybrene and a spin infection was performed by centrifugation at 2,200 rpm for 1 hour. Post-infection, virus was removed and cells were selected with puromycin or blasticidin. For clonal knockout cells, after selection, cells were single-cell diluted into the wells of a 96-well plate. Cells were grown for two weeks, and the resultant colonies were expanded. Clones were validated for loss of the relevant protein via immunoblotting.

Table 7.2. List of sgRNAs and qPCR primers used in this work.

Primer Name	**Sequence**
sgmControl TOP	caccgACTGTCGAGAACCAGAGAGA
sgmControl BOT	aaacTCTCTCTGGTTCTCGACAGTc
sgmHmbs TOP	caccgCATACAGACCGACACTGTGG
sgmHmbs BOT	aaacCCACAGTGTCGGTCTGTATGc
sgmHmox1 TOP	caccGGCCTTGCCCAGCTCTGGGG
sgmHmox1 BOT	aaacCCCCAGAGCTGGGCAAGGCC
sgmAtg7 TOP	caccGAAGTTGAACGAGTACCGCC
sgmAtg7 BOT	aaacGGCGGTACTCGTTCAACTTC
sgATG7 TOP	caccgATAGCTGGGCAGCAACGGGC
sgATG7 BOT	aaacGCCCGTTGCTGCCCAGCTATc
sgmRipk1 TOP	caccGAGAAGACAGACCTAGACAG
sgmRipk1 BOT	aaacCTGTCTAGGTCTGTCTTCTC
sgmTnfrsf1a TOP	caccGATGGGGATACATCCATCAG
sgmTnfrsf1a BOT	aaacCTGATGGATGTATCCCCATC
sgmTnfrsf1b TOP	caccGACCAGCGCGACCCAGAGGG
sgmTnfrsf1b BOT	aaacCCCTCTGGGTCGCGCTGGTC
sgmHif1a TOP	caccGTTCACCAAAGTTGAATCAG
sgmHif1a BOT	aaacCTGATTCAACTTTGGTGAAC
sgmEpas1 TOP	caccGGAGCTCACACTGTGAGGCA
sgmEpas1 BOT	aaacTGCCTCACAGTGTGAGCTCC
sgmTap1 TOP	caccGCAGCAGCCAGTCCACCAGA
sgmTap1 BOT	aaacTCTGGTGGACTGGCTGCTGC
sgACSL4_1 TOP	caccGGAACAGCAGCCATAAGTGT
sgACSL4_1 BOT	aaacACACTTATGGCTGCTGTTCC
sgACSL4_2 TOP	caccGTGAAAGAATACCTGGACTG
sgACSL4_2 BOT	aaacCAGTCCAGGTATTCTTTCAC
sgACSL3_1 TOP	caccGGACTACAATACTGGCAGAG
sgACSL3_1 BOT	aaacCTCTGCCAGTATTGTAGTCC
sgACSL3_2 TOP	caccGCATACCATGGCTGCAGTGG
sgACSL3_2 BOT	aaacCCACTGCAGCCATGGTATGC
sgCHP1_1 TOP	caccGAGGCGAGTGATTTGACTGT
sgCHP1_1 BOT	aaacACAGTCAAATCACTCGCCTC
sgCHP1_2 TOP	caccgCAGGTGCTACGCATGATGGT
sgCHP1_2 BOT	aaacACCATCATGCGTAGCACCTGc

sgmCHP1_1 TOP	caccGAGGAGATCAAGAAGGAGAC
sgmCHP1_1 BOT	aaacGTCTCCTTCTTGATCTCCTC
sgmCHP1_2 TOP	caccGTTCTCCCCTTTGTCCAGGC
sgmCHP1_2 BOT	aaacGCCTGGACAAAGGGGAGAAC
sgGPAT4_1 TOP	caccGGTGGTGGGCACAACTGTGG
sgGPAT4_1 BOT	aaacCCACAGTTGTGCCCACCACC
sgGPAT4_2 TOP	caccGTGTGGGCAGGCCTTCACCA
sgGPAT4_2 BOT	aaacTGGTGAAGGCCTGCCCACAC
sgGPAT3 TOP	caccgACTGATCCCAATGAAAGCCA
sgGPAT3 BOT	aaacTGGCTTTCATTGGGATCAGTc
sgGNPAT_1 TOP	caccgATGGCTAAAAGGCTTAACCC
sgGNPAT_1 BOT	aaacGGGTTAAGCCTTTTAGCCATc
sgGNPAT_2 TOP	caccgAGATGAACTGGAAGACTCCA
sgGNPAT_2 BOT	aaacTGGAGTCTTCCAGTTCATCTc
dElm F	AACCAAATCGAGCGACTTTACT
dElm R	CAGTTCCGGGATACGCATCAG
dRpl32l F	CCCAAGGGTATCGACAACAGA
dRpl32l R	CGATCTCGCCGCAGTAAAC
CHP1 F	CTTGCCATCAACCCACTGG
CHP1 R	CCACGGAAGTTTACCTGGTCC
GPAT4 F	ACTCATGGGTGTGATTCAGAGA
GPAT4 R	GGCGATCCTTCACTTCCGA
RPL32 F	TGTCCTTTGTGCCTACTGCTA
RPL32 R	CTTGTTCAGACGGTGTCTCTC
mPparg F	GTGCCAGTTTCGATCCGTAGA
mPparg R	GGCCAGCATCGTGTAGATGA
mAdiponectin F	GCACTGGCAAGTTCTACTGCAA
mAdiponectin R	GTAGGTGAAGAGAACGGCCTTGT
mTbp F	GGGTATCTGCTGGCGGTTT
mTbp R	TGAAATAGTGATGCTGGGCACT

Cell proliferation and survival assays

For cell proliferations assays with fold change in cell numbers, indicated cell lines were cultured in replicates of three in 96-well plates at 1000 (suspension) or 150 (adherent) cells per well in 200 uL RPMI base media under the conditions described in each experiment, and a separate group of 3 wells was also plated for each cell line with no treatment for an initial time point. Immediately (untreated cells for initial time point) or after 4 days (with varying treatment conditions), 40 uL of Cell Titer Glo reagent (Promega) was added to each well, mixed briefly, and the luminescence read on a luminometer (Molecular Devices). Initial reading and treatment for adherent cells were carried out after cells were allowed to adhere overnight. For each well, the fold change in luminescence relative to the initial luminescence was measured and reported in a $\log_2$ scale as the number of population doublings. Cell culture images were taken using a Primovert microscope (Zeiss).

For cell proliferation assays with KP panc and KP lung cells, cells were plated in triplicates in 6-well plates at 10000 cells/well. Cells were dissociated with trypsin at the indicated days and counted by Z2 Coulter Counter (Beckman). 300000 cells/well were then plated in new plates and counted again at the indicated days. For survival assays with chemical treatments, cells were plated in triplicates in 12-well plates and allowed to adhere for 2 hrs before adding chemicals. Chemicals were added on the day of plating unless otherwise indicated. Cells were plated at 200000 cells/well and counted after 2 days or plated at 100000 cells/well and counted after 3 days.

Bovine serum albumin (BSA) conjugation of fatty acids

All fatty acids used for treatment were conjugated to BSA. A 12 mM solution of the indicated fatty acid was made by dissolving the fatty acid in 20 mL of 0.01M NaOH and stirred for 30 min at 70°C. Dissolved fatty acid solution was added into a stirring 60 mL 10% BSA solution in PBS to make a final concentration of 3 mM. Solution was incubated with stirring for 1hr at 37°C to allow fatty acids to conjugate with BSA. Solution was then 0.22 μm filtered and stored in a glass container.

Lipid metabolite profiling and isotope tracing

For lipid metabolite profiling experiments, Jurkat cells (3×10^6 cells per replicate) were cultured as triplicates in 6-well plates and treated for 24 hrs with the indicated conditions prior to collection of cells and washing with 1 mL of cold 0.9% NaCl. Cell pellets were resuspended in 500 uL of cold LC/MS grade methanol, and non-polar metabolites extracted by consecutive addition of 250 uL LC/MS grade water followed by 400 uL of LC/MS grade chloroform. HeLa and 3T3-F442A cells (6×10^5 cells per replicate) were cultured as triplicates in 6-well plates and allowed to adhere overnight. Cells were subsequently treated for 24 hrs with the indicated conditions and washed in-well with 1mL of cold 0.9% NaCl. After consecutive addition of 600 uL of LC/MS grade methanol and 300 uL of LC/MS grade water, cells were scraped off and 750 uL of the suspension was mixed with 400 uL of LC/MS grade chloroform for non-polar metabolites extraction. After 10 min extraction by vortexing at 4°C and centrifugation for 10 min at 10,000 x g and 4°C, 350 μL of the lower lipid-containing layer was carefully collected and dried under nitrogen. Dried lipid extracts were stored at -80°C until LC/MS analysis. For isotope tracing experiments, cells were treated with 500 uM [U-^{13}C16]-palmitate (Cambridge Isotope Laboratories) for 24 hrs before metabolite extraction. For liver tissue samples, 50 mg tissues were taken from each sample and homogenized in 500 uL methanol + 250 uL water + 400 uL chloroform by Bead Ruptor 24 (Omni International). Lipids were then extracted by vortexing and subsequent processing similarly to Jurkat cells. For *C. elegans* samples, 1000 worms were collected and for *D. melanogaster*, 10 mg of migut tissue was pooled from multiple flies for each replicate. Samples were treated the same way as Jurkat cells except for a longer vortexing step of 1 hr.

Lipids were separated on an Ascentis Express C18 2.1 x 150 mm 2.7 μm column (Sigma-Aldrich) connected to a Vanquish UHPLC system and a QExactive Plus benchtop orbitrap mass spectrometer (Thermo Fisher Scientific) equipped with a heated electrospray ionization (HESI) probe. Dried lipid extracts were reconstituted in 50 uL 65:30:5 acetonitrile:isopropanol:water (v/v/v) and 5 uL of sample were injected into the LC/MS/MS, with separate injections for positive and negative ionization modes. Mobile phase A in the chromatographic method consisted of 60:40

water:acetonitrile with 10 mM ammonium formate and 0.1% formic acid, and mobile phase B consisted of 90:10 isopropanol:acetonitrile, with 10 mM ammonium formate and 0.1% formic acid. The chromatographic gradient was described previously (Hu et al., 2008). The column oven and autosampler were held at 55°C and 4°C, respectively. The mass spectrometer parameters were described previously (Bird et al., 2011). The spray voltage was set to 3.0 kV, and the heated capillary and the HESI were held at 285°C and 350°C, respectively. The S-lens RF level was set to 45, sweep gas at 1 and the sheath and auxiliary gas were set to 60 and 20 units, respectively. These conditions were held constant for both positive and negative ionization mode acquisitions. External mass calibration was performed every 7 days using the standard calibration mixture.

Mass spectra were acquired in both full-scan and data-dependent MS/MS mode. For the full-scan acquisition, the resolution was set to 70,000, the AGC target was 1×10^6, the maximum injection time was 50 msec, and the scan range was m/z = 120-2000. For data-dependent MS/MS, the top 10 ions in each full scan were isolated with a 1.2-Da window, fragmented with a step-wise collision energy of 20, 30, and 40 units, and analyzed at a resolution of 17,500 with an AGC target of 1×10^5 and a maximum injection time of 75 msec. The underfill ratio was set to 0. The selection of the top 10 ions was set to isotopic exclusion, a dynamic exclusion window of 8.0 sec.

High-throughput identification and relative quantification of lipids were performed separately for positive and negative ionization mode data, using LipidSearch software (ThermoFisher Scientific/ Mitsui Knowledge Industries) (Taguchi and Ishikawa, 2010; Yamada et al., 2013) using the default parameters for QExactive product search and alignment. After alignment, raw peak areas for all identified lipids were exported to Microsoft Excel and filtered according to the following predetermined quality control criteria: Rej ("Reject" parameter calculated by LipidSearch) equal to 0; PQ ("Peak Quality" parameter calculated by LipidSearch software) greater than 0.85; CV (standard deviation / mean peak area across triplicate injections of a represented (pooled) biological sample) below 0.4; R (linear correlation across a three-point dilution series of the representative (pooled) biological sample) greater than 0.9. Typically, approximately 70% of identified lipids passed all four quality control criteria. Raw peak areas of the filtered lipids were added together to create a total lipid signal for each sample, and individual lipid peak areas were normalized to this total signal as a control for lipid extraction efficiency, as well as sample loading. Lipid groups with CV more than 0.15 were then excluded.

Stimulated Raman scattering microscopy

The setup for SRS microscopy was similar to what was described earlier (Shen et al., 2014), which integrates picoEmerald laser system (Applied Physics and Electronics) and a laser-scanning microscope (FV1200MPE; Olympus). The images were taken through a 60× objective (water immersion, N.A. = 1.2, UPlanAPO/IR; Olympus). The lasers were tuned so that C-D bond vibration at 2101 cm^{-1} could be selectively imaged. Images were acquired by Fluoview Software and were later assigned pseudo colors in ImageJ. CH_3 bond vibration signal was collected for use as protein content normalization.

Fluorescence microscopy

In 6-well plates, 300,000 cells were seeded on coverslips previously coated with fibronectin. 12 hours later, cells were fixed for 15 min with 4% paraformaldehyde diluted in PBS at room

temperature. After three washes with PBS, cells on the coverslips were permeabilized by incubation with 0.01% TritonX-100 in PBS for 1 min at room temperature prior to another three PBS washes. Coverslips were incubated with Alexa 488 Phalloidin (20X diluted in PBS) at room temperature for 20 min and washed thrice with PBS. Coverslips were then incubated with LipidTOX neutral lipid stain (1000X diluted in PBS) at room temperature for 30 min. After three washes with PBS, coverslips were incubated with a 200 nM solution of DAPI in PBS for 5 min in dark, washed three times with PBS and finally mounted onto slides with Prolong Gold antifade mounting media (Invitrogen). Images were taken on a Delta Vision bright-field fluorescence Inverted Olympus IX-71 microscope (GE Healthcare).

Differentiation and oil red O staining of 3T3-F442A cells

For differentiation, 3T3-F442A cells were subcultured in 6-well collagen-coated plates (Corning BioCoat) and grown to confluence. Differentiation was induced by treating confluent cells with medium containing 10% FBS, 1 µM dexamethasone, 1 µM rosiglitazone, 850 nM insulin, and 1 nM T3 for 48 hrs. On day 2 of differentiation, cells were switched to medium containing 10% FBS, 1 µM rosiglitazone, 850 nM insulin, and 1 nM T3. From day 4 and onwards, differentiated cells were kept in maintenance medium containing 10% FBS, 850 nM insulin, and 1 nM T3, changing the medium every 48 hrs. On day 7, differentiated cells were subject to analyses. Cells in each well were washed with 2 mL of PBS once and fixed with 4% paraformaldehyde for 15 min at room temperature. Paraformaldehyde was aspirated and each well was washed with 60% isopropanol. Cells were incubated with oil red O working solution for 15 min at room temperature and washed with 60% isopropanol. Cells were then washed with deionized water and kept in PBS for imaging. Micrographs were taken with a REVOLVE4 microscope (Echo Laboratories).

Nile red staining of *C. elegans*

Feeding RNAi was performed on N2 (wildtype) *C. elegans* as described (Kamath et al., 2000). The Y71H2AL.c clone (*pbo-1*) from the Vidal RNAi feeding library was used (Rual et al., 2004). 500-1000 worms were collected and washed twice with PBS + 0.1% Triton X-100. Worms were then fixed with 200 µL of 40% isopropanol for 3 min. Excess supernatant was removed and the worms were stained in 150 µL of Nile red working solution (6 µL of 0.5 mg/mL Nile red dissolved in acetone) for 30 min at room temperature in dark with gentle rocking. Nile red working solution was removed and worms were resuspended in 50 µL M9 buffer and mounted on a 2% agarose pad for microscopy. Nile red stain was observed under the FITC channel. Fluorescence images were taken using a Primovert microscope (Zeiss).

Nile red staining and qPCR of *D. melanogaster*

D. melanogaster lines were kept at a 12-hour light/dark cycle and all crosses were performed at 22-25°C. The following fly stocks were provided from Bloomington Drosophila Stock Center (BDSC) and Vienna Drosophila Resource Center (VDRC). The stock numbers (#) were given in parentheses. Those stocks used in here are: *White* RNAi (BDSC#33623), *elm* RNAi (VDRC#108624), *Actin5C Gal4* (BDSC#3954). Adult flies were directly homogenized in 1 mL TRIzol (Life Technologies) and total RNA was isolated according to the manufacturer's protocol (RNeasy mini kit, QIAGEN). cDNA library was prepared from 5 µg total RNA, by using oligo(dT)

amplification and the Superscript III First Strand synthesis kit (Invitrogen). cDNA library was used to amplify the *Elm* and *Rp32l* transcripts with the forward 5'-AACCAAATCGAGCGACTTTACT-3', reverse 5'-CAGTTCCGGGATACGCATCAG-3' and forward 5'-CCCAAGGGTATCGACAACAGA-3', reverse 5'-CGATCTCGCCGCAGTAAAC-3' primers, respectively. 5 days old adult midguts and fat bodies were dissected in ice cold PBS and kept on ice until required sample size obtained. Tissues were then fixed in ice cold 4% paraformaldehyde/PBS for 20 min at room temperature and washed with PBS for 3 x 10 min. Tissues were stained with 0.25 ug/mL Nile Red/PBS solution for 30 min at room temperature. Following the staining, samples were washed in PBS for 3 x 10 min at room temperature. Specimens were finally mounted in Fluoromount-G (Southern Biotech) and analyzed with confocal microscopy.

Immunoprecipitation

Before lysis for immunoprecipitation, proteins were crosslinked in live cells in media by adding dithiobis(succinimidyl propionate) to a working concentration of 2.5 mM and incubating for 15 min at room temperature. Crosslinking reaction was quenched by adding 1/10 volume of 1M Tris pH 8.5 to the media and incubating for 2 min at room temperature. Cells were washed with ice cold TBS (150 mM NaCl) twice and lysed as described for immunoblotting. For anti-FLAG immunoprecipitations, the FLAG-M2 affinity gel was washed with 1 mL TBS (150 mM NaCl) twice and 40 uL or 20uL of a 50% slurry of the affinity gel was then added to the lysate supernatant and incubated with rotation at 4°C for 120 min. Affinity gel was washed twice with wash buffer (TBS, 150 mM NaCl, 0.01% Tween-20, 0.2% fos-choline-13) and once with TBS (300 mM NaCl). Proteins were eluted by incubating with 500 ng/uL of 3XFlag peptide in TBS (300 mM NaCl) with 0.2% fos-choline-13 for 15 min at room temperature. For anti-HA immunoprecipitations, HA magnetic beads were washed with wash buffer twice and 25 uL of a 50% slurry of the magnetic beads was then added to the lysate supernatant and incubated with rotation at room temperature for 30 min. Beads were washed twice with wash buffer and once with TBS (300 mM NaCl). Proteins were eluted by incubating with 0.1M glycine, pH 2.0 with 0.2% fos-choline-13 for 10 min at room temperature. Low pH was neutralized by adding 15 uL 1M Tris, pH 8.5 for each 100 uL of eluate. For anti-GPAT4 immunoprecipitation, 50 µL of Dynabeads M-280 Sheep Anti-Rabbit IgG slurry was washed 1mL wash buffer twice and incubated with either anti-GPAT4 antibody or isotype control IgG for 1 hr with rotation at 4°C. Conjugated beads were washed twice with wash buffer and incubated with lysate supernatant for 120 min with rotation at 4°C. Beads were washed and proteins were eluted as outlined for anti-HA immunoprecipitations.

Proteomics from immunoprecipitate

Following immunoprecipitation, proteins were either cleaned up by ice cold acetone precipitation (HA-GPAT4) or by running samples shortly into SDS-PAGE (FLAG-CHP1). SDS-PAGE cleaned-up samples were reduced, alkylated (10 mM DTT, 30 mM iodoacetamide, Sigma) and digested with trypsin (Shevchenko et al., 1996). Precipitated protein samples where reduced and alkylated (10 mM DTT, 40 mM iodoacetamide, Sigma), in 8 M urea and digested with Endoproteinase LysC (Wako Chemicals) and trypsin (Promega). The acidified digests were desalted (Rappsilber et al., 2007) and analyzed by reversed phase nano-LC-MS/MS using either a Fusion Lumos or a Q-Exactive Plus (Thermo Scientific).

Data were quantified and searched against a Uniprot human database (March 2016) using ProteomeDiscoverer v. 1.4.0.288 (Thermo Scientific) combined with Mascot v. 2.5.1 (Matrix Science). Oxidation of methionine and protein N-terminal acetylation were allowed as variable modifications and all cysteines where treated as carbamidomethylated. Peptide matches were filtered using a Percolator (Käll et al., 2007), calculated false discovery rate of 1%. Contaminants are further removed by comparison to proteins in the CRAPome v1.1 (Mellacheruvu et al., 2013) with an average SC of 0.2 and above and a FLAG-GFP control immunoprecipitation.

GPAT activity assay

Cell lysates were prepared as described for immunoblotting. 200 ug of each lysate was resuspended in 300 uL of assay buffer (75 mM Tris-HCl, pH 7.5, 4 mM $MgCl_2$, 1 mg/ml fatty acid free BSA). Samples were supplemented with or without 50 uM palmitoyl-CoA as indicated. Each sample was incubated with 0.5 µCi or 10.4 µM [^{14}C]-glycerol-3-phosphate for 30 min at 37°C. Reaction was stopped by adding 500 µL 1-butanol. After adding 800 µL of deionized water and vortexing, samples were centrifuged at 14,000 x g for 5 min at room temperature. The bottom polar layer was removed and the non-polar layer was washed with 1200 µL of butanol-saturated water. Samples were vortexed and centrifuged at 14,000 x g for 5 min at room temperature. 200 µL of the non-polar layer was mixed in scintillation vials with 5 mL of ScintiSafe Econo Cocktail (Fisher). Radioactivity was measured in a Tri-Carb 2910 Liquid Scintillation Analyzer (Perkin Elmer) and the counts per minute (cpm) for each vial were normalized by microgram of protein.

UV crosslinking with bifunctional fatty acid reporter

The bifunctional x-alk-16 was synthesized as previously described (Peng and Hang, 2015). Cells were grown in 6-well plates and incubated in regular DMEM supplemented with 2% charcoal/dextran treated fetal bovine serum (HyClone) with DMSO control or 50 µM x-alk-16 for 2 hrs at 37°C and 5% CO_2. Cell media was changed to PBS and cells were UV irradiated at 365 nm on ice for 10 min using a Spectrolinker XL-1000 UV crosslinker (Spectronics) at a distance of 3 cm. Cells were then lysed and analyzed by immunoprecipitation for the crosslinked proteins as described above.

Real time PCR assays

For HeLa cells, RNA was isolated using the RNeasy Kit (Qiagen) according to the manufacturer's protocol. For 3T3-F442A cells, cells were lysed in-well with 0.5 mL of Trizol (Life Technologies) and RNA was isolated using manufacturer's protocol. RNA was spectrophotometrically quantified and equal amounts were used for cDNA synthesis with the Superscript III RT Kit (Invitrogen). qPCR analysis was performed on a ABI Real Time PCR System (Applied Biosystems) with the SYBR green Master Mix (Applied Biosystems). *Rpl32* was used as control for HeLa while *Tbp* was used as control for 3T3-F442A.

Polar metabolite profiling for palmitoyl-CoA quantification

Jurkat cells (3 x 10^6 cells per replicate) were cultured as triplicates in 6-well plates and treated for 24 hrs with the indicated conditions prior to collection of cells and washing with 1 mL of cold 0.9% NaCl. Polar metabolites were extracted in 0.5 mL of cold 80% methanol containing internal standards (Cambridge Isotope Laboratories). After extraction, samples were nitrogen-dried and stored at -80C until analysis by LC-MS. Analysis was conducted on a QExactive benchtop orbitrap mass spectrometer equipped with an Ion Max source and a HESI II probe, which was coupled to a Dionex UltiMate 3000 UPLC system (Thermo Fisher Scientific). External mass calibration was performed using the standard calibration mixture every 7 days.

Dried polar samples were resuspended in 100 µL water and 2 µL were injected into a ZIC-pHILIC 150 x 2.1 mm (5 µm particle size) column (EMD Millipore). Chromatographic separation was achieved using the following conditions: Buffer A was 20 mM ammonium carbonate, 0.1% ammonium hydroxide; buffer B was acetonitrile. The column oven and autosampler tray were held at 25°C and 4°C, respectively. The chromatographic gradient was run at a flow rate of 0.150 mL/min as follows: 0–20 min.: linear gradient from 80% to 20% B; 20–20.5 min.: linear gradient from 20% to 80% B; 20.5–28 min.: hold at 80% B. The mass spectrometer was operated in full-scan, polarity switching mode with the spray voltage set to 3.0 kV, the heated capillary held at 275°C, and the HESI probe held at 350°C. The sheath gas flow was set to 40 units, the auxiliary gas flow was set to 15 units, and the sweep gas flow was set to 1 unit. The MS data acquisition was performed in a range of 70–1000 m/z, with the resolution set at 70,000, the AGC target at 10e6, and the maximum injection time at 20 msec. Relative quantitation of polar metabolites was performed with XCalibur QuanBrowser 2.2 (Thermo Fisher Scientific) using a 5 ppm mass tolerance and referencing an in-house library of chemical standards. Metabolite levels were normalized to the total protein amount for each condition.

Seahorse fatty acid oxidation assay

HeLa cells were seeded into Seahorse XF 96-well plates at 30,000 cells/well. Seahorse fatty acid oxidation assay was carried out following manufacturer's protocol using the Seahorse XF Palmitate-BSA fatty acid oxidation (FAO) Substrate (Agilent) on a Seahorse XFe96 Analyzer (Agilent). Maximal respiration due to exogenous fatty acids was calculated as the maximal Palm:BSA-Eto rate minus maximal BSA-Eto rate minus oxygen consumption rate due to uncoupling by fatty acids.

Click chemistry

Immunoprecipitation of the FLAG-CHP1 constructs were carried out as described above. Before the elution step, beads were incubated with 22 µL lysis buffer with 3 µL freshly prepared click chemistry reaction cocktail (azido-rhodamine (0.55 µL, 10 mM stock solution in DMSO), tris(2-carboxyethyl)phosphine hydrochloride (TCEP) (0.55 µL, 50 mM freshly prepared stock solution in deionized water), tris[(1-benzyl-1H-1,2,3-triazol-4-yl)methyl]amine (TBTA) (1.36 µL, 10 mM stock solution in DMSO/t-butanol) and $CuSO_4 \cdot 5H_2O$ (0.55 µL, 50 mM freshly prepared stock solution in deionized water)) at room temperature for 1 h. Beads were then eluted and analyzed by SDS-PAGE as described above. Gel was scanned on a GE Healthcare Typhoon 9400 variable

mode imager with excitation and emission at 532 nm and 580 nm, respectively. The same gel was then transferred onto a PVDF membrane for downstream Western blotting analysis.

Quantitative TMT proteomics

After the indicated treatment conditions, cell pellets were processed as per immunoblot protocol and lysed with lysis buffer (50 mM Tris-Cl pH 7.5, 150 mM NaCl, 1 mM EDTA, 2% Triton X-100) supplemented with protease inhibitors and phosphatase inhibitors (Roche). For liver tissue samples, 50 mg tissues were taken from each sample and first homogenized in lysis buffer by Bead Ruptor 24 (Omni International). Detergent was removed by Wessel/Flügge extraction (Wessel and Flügge, 1984) and the resulting protein pellet was solubilized in 8M urea, 50mM triethylammonium bicarbonate (TEAB). Disulfide bonds were reduced by addition of dithiothreitol (EMD Chemicals) to a final concentration of 10 mM and incubated at room temperature for 1 hour. Thiols were alkylated using 20 mM iodoacetamide (Sigma) for 1 hour at room temperature in the dark. Urea was diluted using 50 mM TEAB and proteins were digested, first with lysyl endopeptidase (Wako Chemicals) for 3 hours and then overnight with sequencing grade modified trypsin (Promega). Digestion was halted by the addition of TFA. Peptides were purified by solid-phase extraction using Oasis HLB cartridges (Waters) according to manufacturer specifications.

Peptide pellets were redissolved in 100 mM TEAB and labeled with tandem mass tags (TMT, Thermo Scientific) in either a 6- or 10-plex format, depending on the experiment. Labeling proceeded for 1 hour at room temperature and was quenched by the addition of hydroxylamine (Thermo Scientific). Peptides were pre-fractionated using a Dionex 3000 Ultimate loading pump equipped with a 2.1*150mm 3.5µm Xbridge C18 column (Waters). Solvent A consisted of 10 mM ammonium hydroxide (Sigma-Aldrich) in water, pH 10 and solvent B consisted of 10 mM ammonium hydroxide, 90% acetonitrile (ACN) in water, pH 10. Peptides were fractionated across a 60-minute gradient and collected fractions were concatenated.

Fractionated peptides were separated using a Dionex 3000 Ultimate HPLC equipped with a NCS3500RS nano- and microflow pump (Dionex). Trapping and separation was carried out using a 100 µm*20mm Acclaim PepMap C18 trap column (Thermo Scientific) and a a 75µm*120mm pulled-emitter nanocolumn (Nikkyo Technos) respectively. Solvent A was 0.1% formic acid in water and solvent B was 0.1% formic acid, 80 % ACN in water. All LC-MS solvents are of HPLC grade and purchased from Sigma. The HPLC was connected to a Q-Exactive HF mass spectrometer (Thermo Scientific) operating in positive ion DDA mode. The MS2 resolution was set to 60k for the 10-plex samples and 30k for the 6-plex samples.

Raw data was searched using MaxQuant v. 1.6.6.0 using standard settings (Cox and Mann, 2008). Spectra were queried against the Mus musculus proteome (obtained from uniprot.org on February 2019) with a false discovery rate (FDR) of 1%. Further data analysis was performed within the Perseus framework (Tyanova et al., 2016). An FDR-corrected student's t-test (FDR=1%) was used to test for significant changes between the two conditions.

Patient-derived pancreatic cancer xenografts

PDX model was described previously(Yamaguchi et al., 2019). Low passage PDX pancreatic tumor was chopped finely with a scalpel and placed in a 50 ml conical tube with a solution of Dulbecco's Modified Eagle Medium (Gibco) supplemented with 10% v/v fetal bovine serum (Corning), L-glutamine (2 mM; Gibco), penicillin-streptomycin (100 U/ml; Gibco), Amphotericin (1 μg/ml; Lonza), sodium pyruvate (1 mM; Gibco) and Collagenase, Type IV (200 U/ml; Worthington) and placed in a 37°C shaker at 220 rpm for 30 min. After centrifugation and removal of supernatant, the sample was subjected to ACK lysis buffer (Lonza) for 3 min at room temperature to remove red blood cells. After centrifugation and removal of ACK lysis buffer, the sample was subjected to a density gradient with Optiprep (1114542, Axis-Shield) to remove dead cells. The sample was washed in media and subjected to a 100-μm cell strainer and followed by a 70-μm cell strainer. Mouse cells were removed from the single-cell suspension via magnetic-associated cell sorting using the Mouse Cell Depletion Kit ((130-104-694, Miltenyi), resulting in a single-cell suspension of predominantly pancreatic cancer cells of human origin. 10 million PDX pancreatic cancer cells were transduced with the indicated sgRNA library and washed with PBS. Cells were resuspended in cold PBS with 50% Matrigel and one million cells were injected subcutaneously into NSG mice. When the tumors reached palpable size (70 mm^3), mouse was euthanized and the tumors were removed and sectioned in a manner similar to the *in vivo* CRISPR-based screens.

Immunohistochemistry

Liver and tumor samples were removed from mice at the time of sacrifice and fixed in 10% buffered formalin for 48 hrs. Samples were maintained in 70% ethanol. Fixed tumor samples were then embedded in paraffin, sectioned and stained with the indicated antibodies with standard protocols.

Immune profiling of tumors

Tumors were excised and digested for one hour at 37°C with 400U/ml of collagenase D (Roche). Hematopoietic cells enrichment was achieved by density gradient centrifugation with 40/90 Percoll (GE Healthcare Life Sciences) for 25 min at 2500rpm at 22°C with zero breaks. Interphase containing the hematopoietic cells was isolated and washed with PBE. Red cell lysis was performed with ACK lysis buffer (GIBCO). For cytokine staining, cells were incubated at 37°C for 4h in complete RPMI media supplemented with Brefeldin A (Sigma), phorbol 12-myristate 13-acetate (PMA) (Sigma) and Ionomycin (Sigma). After incubation cells were washed with PBE. Cells were incubated for 5 min with 1ug/ml of anti-CD16/32 (2.4G2, BioXcell) at room temperature. Cells were washed with PBS and stained with Zombie fixable viability dye (Biolegend) for 15 min at room temperature. Cells were washed with PBE and stained with appropriate surface markers antibodies for CD4 and CD8 T cells and NK cells for 20 min at 4°C. Cells were washed with PBE fixed and permeabilized with Cytofix/Cytoperm kit (BD). Intercellular staining for IFNγ and TNFα was performed for 30 min at 4°C. Cells were washed and resuspended in PBE. Samples were acquired on the BD FACSymphony. Data were analyzed using FlowJo v.10.0.8 software.

OT-I T cell co-culture

OT-I T cells were isolated from OT-I transgenic mice (The Jackson Laboratory) by extracting cells from lymph nodes using the CD8a$^+$ T Cell Isolation Kit (Miltenyi Biotec) and following manufacturer's instructions. T cells were cultured in T cell media (RPMI media (Gibco) containing 2 mM glutamine, 10% fetal bovine serum, 1% penicillin and streptomycin, 1 mM pyruvate, 50 µM 2-mercaptoethanol and 1X MEM Amino Acids Solution (Gibco) with 20 ng/mL IL-2). T cells were activated by Dynabeads Mouse T-Activator CD3/CD28 (Thermo Fisher Scientific) and allowed to proliferate for 6 days. One day prior to co-culture, KP panc cancer cells were seeded in 12-well plates at 50000 or 100000 cells/well with 100 ng/mL IFNγ. The following day, each well with cancer cells was changed to 500 µL fresh media. Activated CD8+ T cells were resuspended in the indicated E:T ratios and added to each well in 500 µL T cell media. After 48 hrs, T cells were washed off and cancer cells were counted. For flow cytometry of apoptotic cells, cancer cells were dissociated and washed with PBS. Cells were stained for 15 min at room temperature in the dark with APC Annexin V (BioLegend) and resuspended in PBS with DAPI. Cells were analyzed on a LSRFortessa (BD Biosciences).

Flow cytometry

For staining of MHC-I, cells were treated for 24 hrs with the indicated concentration of IFNγ and one million cells were resuspended in PBS supplemented with 0.5% BSA and 2mM EDTA (PBE). Cells were incubated for 5 min with 1ug/ml of anti-CD16/32 (2.4G2, BioXcell) at room temperature. Cells were washed with PBS and stained with Zombie fixable viability dye (Biolegend) 15 min at room temperature. Cells were washed with PBE and stained with PE anti-mouse H-2Kb/H-2Db or PE anti-human HLA-A,B,C (Biolegend) antibody for 20 min at 4°C. Cells were washed and resuspended in PBE. Samples were acquired on the BD FACSymphony. Data were analyzed using FlowJo v.10.0.8 software.

For staining of TNFRI, one million cells were resuspended in PBS supplemented with 1% BSA and 1mM EDTA (FACS buffer). Cells were washed with FACS buffer and stained with APC anti-mouse TNFRI (Biolegend) antibody for 15 min at 4°C in the dark. Cells were washed and resuspended in FACS buffer with 60 ng/mL DAPI. Samples were acquired on the BD FACSymphony. Data were analyzed using FlowJo v.10.0.8 software.

RNAseq

For *in vitro* samples, cells were cultured as indicated and RNA was extracted using RNeasy mini kit (Qiagen) following manufacturer's protocol. For tumor samples, tumors were dissected 2 weeks after injection. A 20 mg tissue from each sample was homogenized using Bead Ruptor 24 (Omni International) and RNA was processed using RNeasy mini kit following manufacturer's protocol. Purified total RNA was cleaned up and mRNA was sequenced by NextSeq High Output. For analysis, reads were mapped to the mouse transcriptome (mm10, Ensembl annotations) using STAR (v2.7). FeatureCounts (v1.6) was used to count exonic reads (with -O option) and DESeq2 v1.20 (R v3.5.1) was used to normalize and compare samples. PCA plots were generated using the plotPCA function (DESeq2) after variance stabilization and dispersion estimation. Log-fold changes across all genes were used as input to iPAGE with the following parameters: ebins=9,

max_p=0.005, and using MSigDB h gene sets (i.e. the Hallmarks gene set collection). The RNAseq dataset generated in this study is available at GEO (accession number GSE158707).

Survival Analysis

TCGA-PAAD gene expression data (FPKM, downloaded from Genomic Data Commons on 10/13/2016) and the associated clinical data (cBioportal) were used to perform survival analysis. For gene signatures, the expression of each gene was first z-score normalized and the signature score was calculated as the weighted sum of the z-scores. Given the short survival of PAAD patients, the analysis was limited to 3 years. To determine the separation threshold, the samples were divided based on their signature score or expression levels at every value between the 10^{th} and 90^{th} percentiles. Survival analysis was then performed using the survdiff function (survival package in R) and the value with the lowest *p*-value was selected as the threshold. The function survfit was then used to perform the analysis at that threshold and visualize the Kaplan-Meier plot.

Immunofluorescence

For immunofluorescence assays in 6-well plates, 150,000 cells were seeded on coverslips previously coated with fibronectin. 12 hours later, cells were treated with 1 mM oleate or control BSA. Subsequently, cells were stained with 1 µM ER-Tracker Blue-White DPX in HBSS for 30 min at 37°C before fixing for 15 min with 4% paraformaldehyde in PBS at room temperature. After three washes with PBS, cells on the coverslips were permeabilized by incubation with 0.2% Triton X-100 in PBS for 10 min prior to another three PBS washes. After incubation with blocking solution (5% normal donkey serum in PBS) for 1 hour, coverslips were incubated with the indicated primary antibodies (1:500 in blocking solution) for an additional hour, and washed 3 times with PBS. Secondary Alexa Fluor 488 donkey anti-rabbit antibody was diluted in blocking solution (1:250) and added to the coverslips for 45 min at room temperature, prior to three washes with PBS. Coverslips were finally mounted onto slides with Prolong Gold antifade mounting media (Invitrogen). Images were taken on an inverted LSM 780 laser scanning confocal microscope (Zeiss).

For immunofluorescence assays in glass-bottom 8-well slides, cells were seeded at 7500 cells per well after pretreating the glass with fibronectin. 24 hours later, cells were treated with 70 ng/mL IFNγ. After 22 hours, cells were stained with anti-H-2Kb/H-2Db antibody (1:200, Biolegend) for 2h at 37°C before fixing with 4% paraformaldehyde in PBS for 10 min at room temperature. After three washes with PBS, cells on coverslips were permeabilized and blocked by incubation with 0.2% Triton-X in PBS + 5% normal donkey serum (NDS) for 1 hour at room temperature, shaking. Cells on coverslips were subsequently incubated with anti-H-2Kb/H-2Db 1:200 for 16 hours at 4°C before washing 3 times with PBS. Coverslips were then incubated with secondary (Alexa Fluor 568 anti-mouse) 1:500 in 5% NDS + 0.2% Triton in PBS for 1 hr and washed 3 times with PBS. Finally, coverslips were mounted onto slides with Prolong Gold Antifade mounting media (Invitrogen).

Confocal images were acquired with a Zeiss inverted LSM 780 laser scanning confocal microscope (Zeiss) using a 63x/1.4 DIC Plan-Apochromat oil immersion objective. Images were obtained with excitation and emission wavelengths as follows: DAPI 405-464, Alexa Fluor 568 561-605. The

images are 1192 x 1192 pixels with a pixel depth of 16-bit, with a pixel size of 14.0204µm per pixel, a dwell time of 1.58µs, a pinhole size of 11.2 (1Airy unit), and a line averaging of 1.

Generation of CRISPR CHP1 knockout mice

Mouse CHP1_KO1 gRNA sequence from **Figure 2.6C** was used to generate CRISPR knockout mice. The synthetic crRNA and tracrRNA (Alt-RTM CRISPR guide RNAs, IDT) in equimolar was annealed to form ctRNA duplex in a final concentration of 100uM in IDTE. To assemble the Cas9 ribonucleoprotein, Cas9 protein and ctRNA duplex were mixed in IDTE buffer (final concentration, Cas9 protein: 30ng/ul, ctRNAs duplex: 0.2uM, 0.06uM and 0.02uM), incubated at 37°C for 15 min, and passed through Millipore Centrifugal Filter unit.

All animal experiments performed complied with the IACUC approved protocols. C57BL/6 mice at 3–4 weeks of age (Charles River Laboratories) were superovulated by intraperitoneal injection of 5 IU pregnant mare serum gonadotropin, followed 48 h later by injection of 5 IU human chorionic gonadotropin. To obtain mouse zygotes, C57BL/6 stud males were mated with superovulated C57BL/6 females. One-cell stage fertilized mouse embryos were retrieved at 0.5 day post coitum (dpc). Pronuclear injections were performed in Rockefeller University Transgenic Lab using standard protocol. After injection, embryos were cultured in KSOM in CO^2 incubator (5% CO_2 at 37°C) overnight. Surviving 2-cell stage embryos were transferred to Swiss Webster pseudopregnant female mice via oviduct-transfer.

Statistical analysis

Sample size, mean, and significance p values are indicated in the text and figure legends. Error bars in the experiments represent standard deviation (SD) from either independent experiments or independent samples. Student's t test was used for comparisons with single variable. ANOVA was used for comparisons with two or more variables. Statistical analyses were performed using GraphPad Prism 8 or reported by the relevant computational tools.

REFERENCES

Abu-Remaileh, M., Wyant, G.A., Kim, C., Laqtom, N.N., Abbasi, M., Chan, S.H., Freinkman, E., and Sabatini, D.M. (2017). Lysosomal metabolomics reveals V-ATPase- and mTOR-dependent regulation of amino acid efflux from lysosomes. 8.

Ackerman, D., and Simon, M.C. (2014). Hypoxia, lipids, and cancer: surviving the harsh tumor microenvironment. Trends in Cell Biology *24*, 472–478.

Ackerman, D., Tumanov, S., Qiu, B., Michalopoulou, E., Spata, M., Azzam, A., Xie, H., Simon, M.C., and Kamphorst, J.J. (2018). Triglycerides promote lipid homeostasis during hypoxic stress by balancing fatty acid saturation. Cell Reports *24*, 2596-2605.e5.

Agarwal, A.K., Sukumaran, S., Cortés, V.A., Tunison, K., Mizrachi, D., Sankella, S., Gerard, R.D., Horton, J.D., and Garg, A. (2011). Human 1-acylglycerol-3-phosphate O-acyltransferase isoforms 1 and 2: biochemical characterization and inability to rescue hepatic steatosis in Agpat2(-/-) gene lipodystrophic mice. Journal of Biological Chemistry *286*, 37676–37691.

Alam, J., and Cook, J.L. (2007). How many transcription factors does it take to turn on the heme oxygenase-1 gene? Am J Respir Cell Mol Biol *36*, 166–174.

Alkhouri, N., Dixon, L.J., and Feldstein, A.E. (2009). Lipotoxicity in nonalcoholic fatty liver disease: not all lipids are created equal. Expert Rev Gastroenterol Hepatol *3*, 445–451.

Alvarez, S.W., Sviderskiy, V.O., Terzi, E.M., Papagiannakopoulos, T., Moreira, A.L., Adams, S., Sabatini, D.M., Birsoy, K., and Possemato, R. (2017). NFS1 undergoes positive selection in lung tumours and protects cells from ferroptosis. Nature *551*, 639–643.

Amaravadi, R., Kimmelman, A.C., and White, E. (2016). Recent insights into the function of autophagy in cancer. Genes Dev. *30*, 1913–1930.

Badgley, M.A., Kremer, D.M., Maurer, H.C., DelGiorno, K.E., Lee, H.-J., Purohit, V., Sagalovskiy, I.R., Ma, A., Kapilian, J., Firl, C.E.M., et al. (2020). Cysteine depletion induces pancreatic tumor ferroptosis in mice. Science *368*, 85–89.

Balkwill, F.R., Capasso, M., and Hagemann, T. (2012). The tumor microenvironment at a glance. J Cell Sci *125*, 5591–5596.

Barron, C.C., Bilan, P.J., Tsakiridis, T., and Tsiani, E. (2016). Facilitative glucose transporters: Implications for cancer detection, prognosis and treatment. Metabolism *65*, 124–139.

Bayraktar, E.C., Baudrier, L., Özerdem, C., Lewis, C.A., Chan, S.H., Kunchok, T., Abu-Remaileh, M., Cangelosi, A.L., Sabatini, D.M., Birsoy, K., et al. (2019). MITO-Tag Mice enable rapid isolation and multimodal profiling of mitochondria from specific cell types in vivo. Proc Natl Acad Sci USA *116*, 303–312.

Becker, L.M., O'Connell, J.T., Vo, A.P., Cain, M.P., Tampe, D., Bizarro, L., Sugimoto, H., McGow, A.K., Asara, J.M., Lovisa, S., et al. (2020). Epigenetic reprogramming of cancer-associated fibroblasts deregulates glucose metabolism and facilitates progression of breast cancer. Cell Reports *31*, 107701.

Bird, S.S., Marur, V.R., Sniatynski, M.J., Greenberg, H.K., and Kristal, B.S. (2011). Serum lipidomics profiling using LC-MS and high-energy collisional dissociation fragmentation: focus on triglyceride detection and characterization. Analytical Chemistry *83*, 6648–6657.

Birsoy, K., Possemato, R., Lorbeer, F.K., Bayraktar, E.C., Thiru, P., Yucel, B., Wang, T., Chen, W.W., Clish, C.B., and Sabatini, D.M. (2014). Metabolic determinants of cancer cell sensitivity to glucose limitation and biguanides. Nature *508*, 108–112.

Birsoy, K., Wang, T., Chen, W.W., Freinkman, E., Abu-Remaileh, M., and Sabatini, D.M. (2015). An essential role of the mitochondrial electron transport chain in cell proliferation is to enable aspartate synthesis. Cell *162*, 540–551.

Braverman, N.E., and Moser, A.B. (2012). Functions of plasmalogen lipids in health and disease. Biochimica et Biophysica Acta (BBA) - Molecular Basis of Disease *1822*, 1442–1452.

Cantor, J.R., Abu-Remaileh, M., Kanarek, N., Freinkman, E., Gao, X., Louissaint, A., Lewis, C.A., and Sabatini, D.M. (2017). Physiologic medium rewires cellular metabolism and reveals uric acid as an endogenous inhibitor of UMP synthase. Cell *169*, 258-272.e17.

Chan, S.Y., Zhang, Y.-Y., Hemann, C., Mahoney, C.E., Zweier, J.L., and Loscalzo, J. (2009). MicroRNA-210 controls mitochondrial metabolism during hypoxia by repressing the iron-sulfur cluster assembly proteins ISCU1/2. Cell Metabolism *10*, 273–284.

Chang, C.-H., Qiu, J., O'Sullivan, D., Buck, M.D., Noguchi, T., Curtis, J.D., Chen, Q., Gindin, M., Gubin, M.M., van der Windt, G.J.W., et al. (2015). Metabolic Competition in the Tumor Microenvironment Is a Driver of Cancer Progression. Cell *162*, 1229–1241.

Chitraju, C., Mejhert, N., Haas, J.T., Diaz-Ramirez, L.G., Grueter, C.A., Imbriglio, J.E., Pinto, S., Koliwad, S.K., Walther, T.C., and Farese, R.V. (2017). Triglyceride synthesis by DGAT1 protects adipocytes from lipid-induced ER stress during lipolysis. Cell Metabolism *26*, 407-418.e3.

Chow, R.D., and Chen, S. (2018). Cancer CRISPR screens in vivo. Trends in Cancer *4*, 349–358.

Colegio, O.R., Chu, N.-Q., Szabo, A.L., Chu, T., Rhebergen, A.M., Jairam, V., Cyrus, N., Brokowski, C.E., Eisenbarth, S.C., Phillips, G.M., et al. (2014). Functional polarization of tumour-associated macrophages by tumour-derived lactic acid. Nature *513*, 559–563.

Commisso, C., Davidson, S.M., Soydaner-Azeloglu, R.G., Parker, S.J., Kamphorst, J.J., Hackett, S., Grabocka, E., Nofal, M., Drebin, J.A., Thompson, C.B., et al. (2013). Macropinocytosis of protein is an amino acid supply route in Ras-transformed cells. Nature *497*, 633–637.

Cox, J., and Mann, M. (2008). MaxQuant enables high peptide identification rates, individualized p.p.b.-range mass accuracies and proteome-wide protein quantification. Nat Biotechnol *26*, 1367–1372.

Dang, C.V. (2012). Links between metabolism and cancer. Genes Dev. *26*, 877–890.

Datta, N.S., and Hajra, A.K. (1984). Does microsomal glycerophosphate acyltransferase also catalyze the acylation of dihydroxyacetone phosphate? FEBS Letters *176*, 264–268.

Dwyer, J.R., Donkor, J., Zhang, P., Csaki, L.S., Vergnes, L., Lee, J.M., Dewald, J., Brindley, D.N., Atti, E., Tetradis, S., et al. (2012). Mouse lipin-1 and lipin-2 cooperate to maintain glycerolipid homeostasis in liver and aging cerebellum. Proceedings of the National Academy of Sciences *109*, E2486–E2495.

Eng, C.H., Wang, Z., Tkach, D., Toral-Barza, L., Ugwonali, S., Liu, S., Fitzgerald, S.L., George, E., Frias, E., Cochran, N., et al. (2016). Macroautophagy is dispensable for growth of KRAS mutant tumors and chloroquine efficacy. Proc Natl Acad Sci USA *113*, 182–187.

Ericsson, J., Jackson, S.M., Kim, J.B., Spiegelman, B.M., and Edwards, P.A. (1997). Identification of glycerol-3-phosphate acyltransferase as an adipocyte determination and differentiation factor 1- and sterol regulatory element-binding protein-responsive gene. Journal of Biological Chemistry *272*, 7298–7305.

Farazi, T.A., Waksman, G., and Gordon, J.I. (2001). The biology and enzymology of protein N-myristoylation. Journal of Biological Chemistry *276*, 39501–39504.

Faubert, B., Li, K.Y., Cai, L., Hensley, C.T., Kim, J., Zacharias, L.G., Yang, C., Do, Q.N., Doucette, S., Burguete, D., et al. (2017). Lactate metabolism in human lung tumors. Cell *171*, 358-371.e9.

Fukuda, Y., Wang, Y., Lian, S., Lynch, J., Nagai, S., Fanshawe, B., Kandilci, A., Janke, L.J., Neale, G., Fan, Y., et al. (2017). Upregulated heme biosynthesis, an exploitable vulnerability in MYCN-driven leukemogenesis. JCI Insight *2*, e92409.

Galluzzi, L., Pietrocola, F., Levine, B., and Kroemer, G. (2014). Metabolic Control of Autophagy. Cell *159*, 1263–1276.

Garcia-Bermudez, J., Baudrier, L., Bayraktar, E.C., Shen, Y., La, K., Guarecuco, R., Yucel, B., Fiore, D., Tavora, B., Freinkman, E., et al. (2019). Squalene accumulation in cholesterol auxotrophic lymphomas prevents oxidative cell death. Nature *567*, 118–122.

Goodarzi, H., Elemento, O., and Tavazoie, S. (2009). Revealing global regulatory perturbations across human cancers. Molecular Cell *36*, 900–911.

Gui, X., Yang, H., Li, T., Tan, X., Shi, P., Li, M., Du, F., and Chen, Z.J. (2019). Autophagy induction via STING trafficking is a primordial function of the cGAS pathway. Nature *567*, 262–266.

Guo, J.Y., Chen, H.-Y., Mathew, R., Fan, J., Strohecker, A.M., Karsli-Uzunbas, G., Kamphorst, J.J., Chen, G., Lemons, J.M.S., Karantza, V., et al. (2011). Activated Ras requires autophagy to maintain oxidative metabolism and tumorigenesis. Genes & Development *25*, 460–470.

Haas, J.T., Miao, J., Chanda, D., Wang, Y., Zhao, E., Haas, M.E., Hirschey, M., Vaitheesvaran, B., Farese, R.V., Kurland, I.J., et al. (2012). Hepatic insulin signaling is required for obesity-dependent expression of SREBP-1c mRNA but not for feeding-dependent expression. Cell Metabolism *15*, 873–884.

Hajra, A.K., Larkins, L.K., Das, A.K., Hemati, N., Erickson, R.L., and MacDougald, O.A. (2000). Induction of the peroxisomal glycerolipid-synthesizing enzymes during differentiation of 3T3-L1 adipocytes. Role in triacylglycerol synthesis. Journal of Biological Chemistry *275*, 9441–9446.

Hanahan, D., and Weinberg, R.A. (2011). Hallmarks of cancer: The next generation. Cell *144*, 646–674.

Hantschel, O., Nagar, B., Guettler, S., Kretzschmar, J., Dorey, K., Kuriyan, J., and Superti-Furga, G. (2003). A myristoyl-phosphotyrosine switch regulates c-Abl. Cell *112*, 845–857.

Harris, A.L. (2002). Hypoxia — a key regulatory factor in tumour growth. Nat Rev Cancer *2*, 38–47.

Hauck, A.K., and Bernlohr, D.A. (2016). Oxidative stress and lipotoxicity. Journal of Lipid Research *57*, 1976–1986.

Henneberry, A.L., and McMaster, C.R. (1999). Cloning and expression of a human choline/ethanolaminephosphotransferase: synthesis of phosphatidylcholine and phosphatidylethanolamine. Biochemical Journal *339*, 291–298.

Hensley, C.T., Wasti, A.T., and DeBerardinis, R.J. (2013). Glutamine and cancer: cell biology, physiology, and clinical opportunities. Journal of Clinical Investigation *123*, 3678–3684.

Hu, C., van Dommelen, J., van der Heijden, R., Spijksma, G., Reijmers, T.H., Wang, M., Slee, E., Lu, X., Xu, G., van der Greef, J., et al. (2008). RPLC-ion-trap-FTMS method for lipid profiling of plasma: method validation and application to p53 mutant mouse model. Journal of Proteome Research *7*, 4982–4991.

Hui, S., Ghergurovich, J.M., Morscher, R.J., Jang, C., Teng, X., Lu, W., Esparza, L.A., Reya, T., Le Zhan, Yanxiang Guo, J., et al. (2017). Glucose feeds the TCA cycle via circulating lactate. Nature *551*, 115–118.

Hwang, R.F., Moore, T., Arumugam, T., Ramachandran, V., Amos, K.D., Rivera, A., Ji, B., Evans, D.B., and Logsdon, C.D. (2008). Cancer-associated stromal fibroblasts promote pancreatic tumor progression. Cancer Res *68*, 918–926.

Käll, L., Canterbury, J.D., Weston, J., Noble, W.S., and MacCoss, M.J. (2007). Semi-supervised learning for peptide identification from shotgun proteomics datasets. Nature Methods *4*, 923–925.

Kamath, R.S., Martinez-Campos, M., Zipperlen, P., Fraser, A.G., and Ahringer, J. (2000). Effectiveness of specific RNA-mediated interference through ingested double-stranded RNA in Caenorhabditis elegans. Genome Biology *2*, 1–10.

Kamphorst, J.J., Cross, J.R., Fan, J., de Stanchina, E., Mathew, R., White, E.P., Thompson, C.B., and Rabinowitz, J.D. (2013). Hypoxic and Ras-transformed cells support growth by scavenging unsaturated fatty acids from lysophospholipids. Proceedings of the National Academy of Sciences *110*, 8882–8887.

Kearney, C.J., Vervoort, S.J., Hogg, S.J., Ramsbottom, K.M., Freeman, A.J., Lalaoui, N., Pijpers, L., Michie, J., Brown, K.K., Knight, D.A., et al. (2018). Tumor immune evasion arises through loss of TNF sensitivity. Sci. Immunol. *3*, eaar3451.

Kelloff, G.J., Hoffman, J.M., Johnson, B., Scher, H.I., Siegel, B.A., Cheng, E.Y., Cheson, B.D., O'Shaughnessy, J., Guyton, K.Z., Mankoff, D.A., et al. (2005). Progress and promise of FDG-PET imaging for cancer patient management and oncologic drug development. Clin Cancer Res *11*, 2785–2808.

Kemiläinen, H., Adam, M., Mäki-Jouppila, J., Damdimopoulou, P., Damdimopoulos, A.E., Kere, J., Hovatta, O., Laajala, T.D., Aittokallio, T., Adamski, J., et al. (2016). The hydroxysteroid (17β) dehydrogenase family gene HSD17B12 is involved in the prostaglandin synthesis pathway, the ovarian function, and regulation of fertility. Endocrinology *157*, 3719–3730.

Kerr, E.M., Gaude, E., Turrell, F.K., Frezza, C., and Martins, C.P. (2016). Mutant Kras copy number defines metabolic reprogramming and therapeutic susceptibilities. Nature *531*, 110–113.

Kimmelman, A.C., and White, E. (2017). Autophagy and tumor metabolism. Cell Metabolism *25*, 1037–1043.

Kishton, R.J., Sukumar, M., and Restifo, N.P. (2017). Metabolic regulation of T cell longevity and function in tumor immunotherapy. Cell Metabolism *26*, 94–109.

Klett, E.L., Chen, S., Yechoor, A., Lih, F.B., and Coleman, R.A. (2017). Long-chain acyl-CoA synthetase isoforms differ in preferences for eicosanoid species and long-chain fatty acids. Journal of Lipid Research *58*, 884–894.

Korc, M. (2007). Pancreatic cancer–associated stroma production. The American Journal of Surgery *194*, S84–S86.

Kuhajda, F.P., Aja, S., Tu, Y., Han, W.F., Medghalchi, S.M., El Meskini, R., Landree, L.E., Peterson, J.M., Daniels, K., Wong, K., et al. (2011). Pharmacological glycerol-3-phosphate acyltransferase inhibition decreases food intake and adiposity and increases insulin sensitivity in diet-induced obesity. American Journal of Physiology-Regulatory, Integrative and Comparative Physiology *301*, R116–R130.

Lawson, K.A., Sousa, C.M., Zhang, X., Kim, E., Akthar, R., Caumanns, J.J., Yao, Y., Mikolajewicz, N., Ross, C., Brown, K.R., et al. (2020). Functional genomic landscape of cancer-intrinsic evasion of killing by T cells. Nature *586*, 120–126.

Lewin, T.M., de Jong, H., Schwerbrock, N.J.M., Hammond, L.E., Watkins, S.M., Combs, T.P., and Coleman, R.A. (2008). Mice deficient in mitochondrial glycerol-3-phosphate acyltransferase-1 have diminished myocardial triacylglycerol accumulation during lipogenic diet and altered phospholipid fatty acid composition. Biochimica et Biophysica Acta (BBA) - Molecular and Cell Biology of Lipids *1781*, 352–358.

Li, C., and Stocker, R. (2009). Heme oxygenase and iron: from bacteria to humans. Redox Report *14*, 95–101.

Liberti, M.V., and Locasale, J.W. (2016). The Warburg effect: How does it benefit cancer cells? Trends in Biochemical Sciences *41*, 211–218.

Lignitto, L., LeBoeuf, S.E., Homer, H., Jiang, S., Askenazi, M., Karakousi, T.R., Pass, H.I., Bhutkar, A.J., Tsirigos, A., Ueberheide, B., et al. (2019). Nrf2 activation promotes lung cancer metastasis by inhibiting the degradation of Bach1. Cell *178*, 316-329.e18.

Lim, J., Park, H., Heisler, J., Maculins, T., Roose-Girma, M., Xu, M., Mckenzie, B., van Lookeren Campagne, M., Newton, K., and Murthy, A. (2019). Autophagy regulates inflammatory programmed cell death via turnover of RHIM-domain proteins. ELife *8*, e44452.

Lin, X., and Barber, D.L. (1996). A calcineurin homologous protein inhibits GTPase-stimulated Na-H exchange. Proceedings of the National Academy of Sciences *93*, 12631–12636.

Lin, K.H., Xie, A., Rutter, J.C., Ahn, Y., Lloyd-Cowden, J.M., Nichols, A.G., Soderquist, R.S., Koves, T.R., Muoio, D.M., MacIver, N.J., et al. (2019). Systematic dissection of the metabolic-apoptotic interface in AML reveals heme biosynthesis to be a regulator of drug sensitivity. Cell Metabolism *29*, 1217-1231.e7.

Listenberger, L.L., Han, X., Lewis, S.E., Cases, S., Farese, R.V., Ory, D.S., and Schaffer, J.E. (2003). Triglyceride accumulation protects against fatty acid-induced lipotoxicity. PNAS *100*, 3077–3082.

Liu, D., Nagan, N., Just, W.W., Rodemer, C., Thai, T.-P., and Zoeller, R.A. (2005). Role of dihydroxyacetonephosphate acyltransferase in the biosynthesis of plasmalogens and nonether glycerolipids. Journal of Lipid Research *46*, 727–735.

Loi, M., Müller, A., Steinbach, K., Niven, J., Barreira da Silva, R., Paul, P., Ligeon, L.-A., Caruso, A., Albrecht, R.A., Becker, A.C., et al. (2016). Macroautophagy proteins control MHC class I levels on dendritic cells and shape anti-viral CD8+ T cell responses. Cell Reports *15*, 1076–1087.

Maguire, O.A., Ackerman, S.E., Szwed, S.K., Maganti, A.V., Marchildon, F., Huang, X., Kramer, D.J., Rosas-Villegas, A., Gelfer, R.G., Turner, L.E., et al. (2021). Creatine-mediated crosstalk between adipocytes and cancer cells regulates obesity-driven breast cancer. Cell Metabolism *33*, 499-512.e6.

Marques, O., Porto, G., Rêma, A., Faria, F., Cruz Paula, A., Gomez-Lazaro, M., Silva, P., Martins da Silva, B., and Lopes, C. (2016). Local iron homeostasis in the breast ductal carcinoma microenvironment. BMC Cancer *16*, 187.

Mayers, J.R., Torrence, M.E., Danai, L.V., Papagiannakopoulos, T., Davidson, S.M., Bauer, M.R., Lau, A.N., Ji, B.W., Dixit, P.D., Hosios, A.M., et al. (2016). Tissue of origin dictates branched-chain amino acid metabolism in mutant Kras-driven cancers. Science *353*, 1161–1165.

Mellacheruvu, D., Wright, Z., Couzens, A.L., Lambert, J.-P., St-Denis, N.A., Li, T., Miteva, Y.V., Hauri, S., Sardiu, M.E., Low, T.Y., et al. (2013). The CRAPome: a contaminant repository for affinity purification–mass spectrometry data. Nature Methods *10*, 730–736.

Mendoza-Ferreira, N., Coutelier, M., Janzen, E., Hosseinibarkooie, S., Löhr, H., Schneider, S., Milbradt, J., Karakaya, M., Riessland, M., Pichlo, C., et al. (2018). Biallelic CHP1 mutation causes human autosomal recessive ataxia by impairing NHE1 function. Neurology Genetics *4*, e209.

Metallo, C.M., and Vander Heiden, M.G. (2013). Understanding metabolic regulation and its influence on cell physiology. Molecular Cell *49*, 388–398.

Meyers, R.M., Bryan, J.G., McFarland, J.M., Weir, B.A., Sizemore, A.E., Xu, H., Dharia, N.V., Montgomery, P.G., Cowley, G.S., Pantel, S., et al. (2017). Computational correction of copy number effect improves specificity of CRISPR–Cas9 essentiality screens in cancer cells. Nature Genetics *49*, 1779–1784.

Minton, D.R., Nam, M., McLaughlin, D.J., Shin, J., Bayraktar, E.C., Alvarez, S.W., Sviderskiy, V.O., Papagiannakopoulos, T., Sabatini, D.M., Birsoy, K., et al. (2018). Serine catabolism by SHMT2 is required for proper mitochondrial translation initiation and maintenance of formylmethionyl-tRNAs. Molecular Cell *69*, 610-621.e5.

Mitchell, A.G., and Martin, C.E. (1995). A novel cytochrome b5-like domain is linked to the carboxyl terminus of the Saccharomyces cerevisiae delta-9 fatty acid desaturase. Journal of Biological Chemistry *270*, 29766–29772.

Nguyen, P., Leray, V., Diez, M., Serisier, S., Bloc'h, J.L., Siliart, B., and Dumon, H. (2008). Liver lipid metabolism. Journal of Animal Physiology and Animal Nutrition *92*, 272–283.

Ohtsubo, K., and Marth, J.D. (2006). Glycosylation in cellular mechanisms of health and disease. Cell *126*, 855–867.

Orvedahl, A., McAllaster, M.R., Sansone, A., Dunlap, B.F., Desai, C., Wang, Y.-T., Balce, D.R., Luke, C.J., Lee, S., Orchard, R.C., et al. (2019). Autophagy genes in myeloid cells counteract IFNγ-induced TNF-mediated cell death and fatal TNF-induced shock. Proc Natl Acad Sci USA *116*, 16497–16506.

Pagac, M., Cooper, D.E., Qi, Y., Lukmantara, I.E., Mak, H.Y., Wu, Z., Tian, Y., Liu, Z., Lei, M., Du, X., et al. (2016). SEIPIN regulates lipid droplet expansion and adipocyte development by modulating the activity of glycerol-3-phosphate acyltransferase. Cell Reports *17*, 1546–1559.

Palorini, R., Votta, G., Pirola, Y., Vitto, H.D., Palma, S.D., Airoldi, C., Vasso, M., Ricciardiello, F., Lombardi, P.P., Cirulli, C., et al. (2016). Protein Kinase A Activation Promotes Cancer Cell Resistance to Glucose Starvation and Anoikis. PLOS Genet *12*, e1005931.

Panchenko, M.V., Farber, H.W., and Korn, J.H. (2000). Induction of heme oxygenase-1 by hypoxia and free radicals in human dermal fibroblasts. American Journal of Physiology-Cell Physiology *278*, C92–C101.

Patel, S.J., Sanjana, N.E., Kishton, R.J., Eidizadeh, A., Vodnala, S.K., Cam, M., Gartner, J.J., Jia, L., Steinberg, S.M., Yamamoto, T.N., et al. (2017). Identification of essential genes for cancer immunotherapy. Nature *548*, 537–542.

Peck, B., and Schulze, A. (2016). Lipid desaturation – the next step in targeting lipogenesis in cancer? FEBS J *283*, 2767–2778.

Peng, T., and Hang, H.C. (2015). Bifunctional fatty acid chemical reporter for analyzing S-palmitoylated membrane protein-protein interactions in mammalian cells. Journal of the American Chemical Society *137*, 556–559.

Perera, R.M., and Bardeesy, N. (2015). Pancreatic cancer metabolism: Breaking it down to build it back up. Cancer Discovery *5*, 1247–1261.

Perera, R.M., Stoykova, S., Nicolay, B.N., Ross, K.N., Fitamant, J., Boukhali, M., Lengrand, J., Deshpande, V., Selig, M.K., Ferrone, C.R., et al. (2015). Transcriptional control of autophagy–lysosome function drives pancreatic cancer metabolism. Nature *524*, 361–365.

Peterson, T.R., Sengupta, S.S., Harris, T.E., Carmack, A.E., Kang, S.A., Balderas, E., Guertin, D.A., Madden, K.L., Carpenter, A.E., Finck, B.N., et al. (2011). mTOR complex 1 regulates lipin 1 localization to control the SREBP pathway. Cell *146*, 408–420.

Poillet-Perez, L., Sharp, D.W., Yang, Y., Laddha, S.V., Ibrahim, M., Bommareddy, P.K., Hu, Z.S., Vieth, J., Haas, M., Bosenberg, M.W., et al. (2020). Autophagy promotes growth of tumors with high mutational burden by inhibiting a T-cell immune response. Nat Cancer *1*, 923–934.

Pompeia, C., Freitas, J.J.S., Kim, J.S., Zyngier, S.B., and Curi, R. (2002). Arachidonic acid cytotoxicity in leukocytes: implications of oxidative stress and eicosanoid synthesis. Biology of the Cell *94*, 251–265.

Prabakaran, T., Bodda, C., Krapp, C., Zhang, B., Christensen, M.H., Sun, C., Reinert, L., Cai, Y., Jensen, S.B., Skouboe, M.K., et al. (2018). Attenuation of cGAS-STING signaling is mediated by a p62/SQSTM1-dependent autophagy pathway activated by TBK1. The EMBO Journal *37*, e97858.

Rappsilber, J., Mann, M., and Ishihama, Y. (2007). Protocol for micro-purification, enrichment, pre-fractionation and storage of peptides for proteomics using StageTips. Nature Protocols *2*, 1896–1906.

Ray, G.J., Boydston, E.A., Shortt, E., Wyant, G.A., Lourido, S., Chen, W.W., and Sabatini, D.M. (2020). A PEROXO-Tag enables rapid isolation of peroxisomes from human cells. IScience *23*, 101109.

Ringel, A.E., Drijvers, J.M., Baker, G.J., Catozzi, A., García-Cañaveras, J.C., Gassaway, B.M., Miller, B.C., Juneja, V.R., Nguyen, T.H., Joshi, S., et al. (2020). Obesity shapes metabolism in the tumormicroenvironment to suppress anti-tumor immunity. Cell *183*, 1848-1866.e26.

Rodriguez-Cuenca, S., Pellegrinelli, V., Campbell, M., Oresic, M., and Vidal-Puig, A. (2017). Sphingolipids and glycerophospholipids – The "ying and yang" of lipotoxicity in metabolic diseases. Progress in Lipid Research *66*, 14–29.

Rual, J.-F., Ceron, J., Koreth, J., Hao, T., Nicot, A.S., Hirozane-Kishikawa, T., Vandenhaute, J., Orkin, S.H., Hill, D.E., van den Heuvel, S., et al. (2004). Toward improving Caenorhabditis elegans phenome mapping with an ORFeome-based RNAi library. Genome Research *14*, 2162–2168.

Ryan, D.P., Hong, T.S., and Bardeesy, N. (2014). Pancreatic adenocarcinoma. N Engl J Med *371*, 1039–1049.

Santana-Codina, N., Roeth, A.A., Zhang, Y., Yang, A., Mashadova, O., Asara, J.M., Wang, X., Bronson, R.T., Lyssiotis, C.A., Ying, H., et al. (2018). Oncogenic KRAS supports pancreatic cancer through regulation of nucleotide synthesis. Nat Commun *9*, 4945.

Semenza, G.L. (2003). Targeting HIF-1 for cancer therapy. Nat Rev Cancer *3*, 721–732.

Shan, D., Li, J., Wu, L., Li, D., Hurov, J., Tobin, J.F., Gimeno, R.E., and Cao, J. (2010). GPAT3 and GPAT4 are regulated by insulin-stimulated phosphorylation and play distinct roles in adipogenesis. Journal of Lipid Research *51*, 1971–1981.

Shen, Y., Xu, F., Wei, L., Hu, F., and Min, W. (2014). Live-cell quantitative imaging of proteome degradation by stimulated Raman scattering. Angewandte Chemie International Edition *53*, 5596–5599.

Shen, Y., Zhao, Z., Zhang, L., Shi, L., Shahriar, S., Chan, R.B., Di Paolo, G., and Min, W. (2017). Metabolic activity induces membrane phase separation in endoplasmic reticulum. Proceedings of the National Academy of Sciences *114*, 13394–13399.

Shevchenko, A., Wilm, M., Vorm, O., and Mann, M. (1996). Mass spectrometric sequencing of proteins silver-stained polyacrylamide gels. Analytical Chemistry *68*, 850–858.

Sousa, C.M., Biancur, D.E., Wang, X., Halbrook, C.J., Sherman, M.H., Zhang, L., Kremer, D., Hwang, R.F., Witkiewicz, A.K., Ying, H., et al. (2016). Pancreatic stellate cells support tumour metabolism through autophagic alanine secretion. Nature *536*, 479–483.

Sullivan, M.R., Danai, L.V., Lewis, C.A., Chan, S.H., Gui, D.Y., Kunchok, T., Dennstedt, E.A., Vander Heiden, M.G., and Muir, A. (2019). Quantification of microenvironmental metabolites in murine cancers reveals determinants of tumor nutrient availability. ELife *8*, e44235.

Swenson, S.A., Moore, C.M., Marcero, J.R., Medlock, A.E., Reddi, A.R., and Khalimonchuk, O. (2020). From synthesis to utilization: the ins and outs of mitochondrial Heme. Cells *9*, 579.

Taguchi, R., and Ishikawa, M. (2010). Precise and global identification of phospholipid molecular species by an Orbitrap mass spectrometer and automated search engine Lipid Search. Journal of Chromatography A *1217*, 4229–4239.

Titov, D.V., Cracan, V., Goodman, R.P., Peng, J., Grabarek, Z., and Mootha, V.K. (2016). Complementation of mitochondrial electron transport chain by manipulation of the NAD+/NADH ratio. Science *352*, 231–235.

Tove, S.B. (1964). Toxicity of saturated fat. The Journal of Nutrition *84*, 237–243.

Tsherniak, A., Vazquez, F., Montgomery, P.G., Weir, B.A., Kryukov, G., Cowley, G.S., Gill, S., Harrington, W.F., Pantel, S., Krill-Burger, J.M., et al. (2017). Defining a cancer dependency map. Cell *170*, 564-576.e16.

Tyanova, S., Temu, T., Sinitcyn, P., Carlson, A., Hein, M.Y., Geiger, T., Mann, M., and Cox, J. (2016). The Perseus computational platform for comprehensive analysis of (prote)omics data. Nat Methods *13*, 731–740.

Van Horn, C.G., Caviglia, J.M., Li, L.O., Wang, S., Granger, D.A., and Coleman, R.A. (2005). Characterization of recombinant long-chain rat acyl-CoA synthetase isoforms 3 and 6: identification of a novel variant of isoform 6. Biochemistry *44*, 1635–1642.

Vande Voorde, J., Ackermann, T., Pfetzer, N., Sumpton, D., Mackay, G., Kalna, G., Nixon, C., Blyth, K., Gottlieb, E., and Tardito, S. (2019). Improving the metabolic fidelity of cancer models with a physiological cell culture medium. Sci. Adv. *5*, eaau7314.

Vergnes, L., Beigneux, A.P., Davis, R., Watkins, S.M., Young, S.G., and Reue, K. (2006). Agpat6 deficiency causes subdermal lipodystrophy and resistance to obesity. Journal of Lipid Research *47*, 745–754.

Wang, X., and Lin, Y. (2008). Tumor necrosis factor and cancer, buddies or foes? Acta Pharmacol Sin *29*, 1275–1288.

Wang, T., Yu, H., Hughes, N.W., Liu, B., Kendirli, A., Klein, K., Chen, W.W., Lander, E.S., and Sabatini, D.M. (2017). Gene essentiality profiling reveals gene networks and synthetic lethal interactions with oncogenic Ras. Cell *168*, 890-903.e15.

Wang, X., Wu, W.K.K., Gao, J., Li, Z., Dong, B., Lin, X., Li, Y., Li, Y., Gong, J., Qi, C., et al. (2019). Autophagy inhibition enhances PD-L1 expression in gastric cancer. J Exp Clin Cancer Res *38*, 140.

Weiss, L., Hoffmann, G.E., Schreiber, R., Andres, H., Fuchs, E., Körber, E., and Kolb, H.J. (1986). Fatty-acid biosynthesis in man, a pathway of minor importance. Purification, optimal assay conditions, and organ distribution of fatty-acid synthase. Biological Chemistry Hoppe-Seyler *367*, 905–912.

Wende, A.R., and Abel, E.D. (2010). Lipotoxicity in the heart. Biochimica et Biophysica Acta (BBA) - Molecular and Cell Biology of Lipids *1801*, 311–319.

Wendel, A.A., Lewin, T.M., and Coleman, R.A. (2009). Glycerol-3-phosphate acyltransferases: Rate limiting enzymes of triacylglycerol biosynthesis. Biochimica et Biophysica Acta (BBA) - Molecular and Cell Biology of Lipids *1791*, 501–506.

Wendel, A.A., Cooper, D.E., Ilkayeva, O.R., Muoio, D.M., and Coleman, R.A. (2013). Glycerol-3-phosphate acyltransferase (GPAT)-1, but not GPAT4, incorporates newly synthesized fatty acids into triacylglycerol and diminishes fatty acid oxidation. Journal of Biological Chemistry *288*, 27299–27306.

Wessel, D., and Flügge, U.I. (1984). A method for the quantitative recovery of protein in dilute solution in the presence of detergents and lipids. Analytical Biochemistry *138*, 141–143.

Wheaton, W.W., and Chandel, N.S. (2011). Hypoxia. 2. Hypoxia regulates cellular metabolism. American Journal of Physiology - Cell Physiology *300*, C385–C393.

Williams, K.J., Argus, J.P., Zhu, Y., Wilks, M.Q., Marbois, B.N., York, A.G., Kidani, Y., Pourzia, A.L., Akhavan, D., Lisiero, D.N., et al. (2013). An essential requirement for the SCAP/SREBP signaling axis to protect cancer cells from lipotoxicity. Cancer Res *73*, 2850–2862.

Wu, J., and Lanier, L.L. (2003). Natural killer cells and cancer. Advances in Cancer Research *90*, 127–156.

Xu, D., Zhao, H., Jin, M., Zhu, H., Shan, B., Geng, J., Dziedzic, S.A., Amin, P., Mifflin, L., Naito, M.G., et al. (2020). Modulating TRADD to restore cellular homeostasis and inhibit apoptosis. Nature *587*, 133–138.

Xu, R., Pelicano, H., Zhou, Y., Carew, J.S., Feng, L., Bhalla, K.N., Keating, M.J., and Huang, P. (2005). Inhibition of glycolysis in cancer cells: a novel strategy to overcome drug resistance associated with mitochondrial respiratory defect and hypoxia. Cancer Res 10.

Yamada, T., Uchikata, T., Sakamoto, S., Yokoi, Y., Fukusaki, E., and Bamba, T. (2013). Development of a lipid profiling system using reverse-phase liquid chromatography coupled to high-resolution mass spectrometry with rapid polarity switching and an automated lipid identification software. Journal of Chromatography A *1292*, 211–218.

Yamaguchi, N., Weinberg, E.M., Nguyen, A., Liberti, M.V., Goodarzi, H., Janjigian, Y.Y., Paty, P.B., Saltz, L.B., Kingham, T.P., Loo, J.M., et al. (2019). PCK1 and DHODH drive colorectal cancer liver metastatic colonization and hypoxic growth by promoting nucleotide synthesis. ELife *8*, e52135.

Yamamoto, K., Venida, A., Yano, J., Biancur, D.E., Kakiuchi, M., Gupta, S., Sohn, A.S.W., Mukhopadhyay, S., Lin, E.Y., Parker, S.J., et al. (2020). Autophagy promotes immune evasion of pancreatic cancer by degrading MHC-I. Nature *581*, 100–105.

Yang, A., Rajeshkumar, N.V., Wang, X., Yabuuchi, S., Alexander, B.M., Chu, G.C., Von Hoff, D.D., Maitra, A., and Kimmelman, A.C. (2014). Autophagy is critical for pancreatic tumor growth and progression in tumors with p53 alterations. Cancer Discovery *4*, 905–913.

Yang, A., Herter-Sprie, G., Zhang, H., Lin, E.Y., Biancur, D., Wang, X., Deng, J., Hai, J., Yang, S., Wong, K.-K., et al. (2018). Autophagy sustains pancreatic cancer growth through both cell-autonomous and nonautonomous mechanisms. Cancer Discov *8*, 276–287.

Yang, S., Wang, X., Contino, G., Liesa, M., Sahin, E., Ying, H., Bause, A., Li, Y., Stommel, J.M., Dell'Antonio, G., et al. (2011). Pancreatic cancers require autophagy for tumor growth. Genes & Development *25*, 717–729.

Yao, C.-H., Fowle-Grider, R., Mahieu, N.G., Liu, G.-Y., Chen, Y.-J., Wang, R., Singh, M., Potter, G.S., Gross, R.W., Schaefer, J., et al. (2016). Exogenous fatty acids are the preferred source of membrane lipids in proliferating fibroblasts. Cell Chemical Biology *23*, 483–493.

Ying, H., Kimmelman, A.C., Lyssiotis, C.A., Hua, S., Chu, G.C., Fletcher-Sananikone, E., Locasale, J.W., Son, J., Zhang, H., Coloff, J.L., et al. (2012). Oncogenic Kras maintains pancreatic tumors through regulation of anabolic glucose metabolism. Cell *149*, 656–670.

Young, T.M., Reyes, C., Pasnikowski, E., Castanaro, C., Wong, C., Decker, C.E., Chiu, J., Song, H., Wei, Y., Bai, Y., et al. (2020). Autophagy protects tumors from T cell–mediated cytotoxicity via inhibition of TNFα-induced apoptosis. Sci. Immunol. *5*, eabb9561.

Yu, J., Loh, K., Song, Z., Yang, H., Zhang, Y., and Lin, S. (2018). Update on glycerol-3-phosphate acyltransferases: the roles in the development of insulin resistance. Nutrition & Diabetes *8*.

Zhang, C., Cooper, D.E., Grevengoed, T.J., Li, L.O., Klett, E.L., Eaton, J.M., Harris, T.E., and Coleman, R.A. (2014). Glycerol-3-phosphate acyltransferase-4-deficient mice are protected from diet-induced insulin resistance by the enhanced association of mTOR and rictor. American Journal of Physiology-Endocrinology and Metabolism *307*, E305–E315.

Zhang, M., Di Martino, J.S., Bowman, R.L., Campbell, N.R., Baksh, S.C., Simon-Vermot, T., Kim, I.S., Haldeman, P., Mondal, C., Yong-Gonzales, V., et al. (2018). Adipocyte-derived lipids mediate melanoma progression via FATP proteins. Cancer Discov *8*, 1006–1025.

Zhu, X.G., Nicholson Puthenveedu, S., Shen, Y., La, K., Ozlu, C., Wang, T., Klompstra, D., Gultekin, Y., Chi, J., Fidelin, J., et al. (2019). CHP1 regulates compartmentalized glycerolipid synthesis by activating GPAT4. Molecular Cell *74*, 45-58.e7.

Zhu, X.G., Chudnovskiy, A., Baudrier, L., Prizer, B., Liu, Y., Ostendorf, B.N., Yamaguchi, N., Arab, A., Tavora, B., Timson, R., et al. (2021). Functional genomics in vivo reveal metabolic dependencies of pancreatic cancer cells. Cell Metabolism *33*, 211-221.e6.